Article:

Aad, G. orcid.org/0000-0002-6665-4934, Aakvaag, E. orcid.org/0000-0001-7616-1554, Abbott, B. orcid.org/0000-0002-5888-2734 et al. (2943 more authors) (2025) Measurements of the production cross-sections of a Higgs boson in association with a vector boson and decaying into WW* with the ATLAS detector at √s = 13 TeV. Journal of High Energy Physics, 2025 (8). 34. ISSN: 1126-6708

https://doi.org/10.1007/jhep08(2025)034

Published for SISSA by Springer

Received: *March 26, 2025*
Accepted: *June 22, 2025*
Published: *August 5, 2025*

Measurements of the production cross-sections of a Higgs boson in association with a vector boson and decaying into WW^* with the ATLAS detector at $\sqrt{s} = 13$ TeV

JHEP08(2025)034

The ATLAS collaboration

E-mail: atlas.publications@cern.ch

Abstract: Measurements of the total and differential Higgs boson production cross-sections, via WH and ZH associated production using $H \to WW^* \to \ell\nu\ell\nu$ and $H \to WW^* \to \ell\nu jj$ decays, are presented. The analysis uses proton-proton events delivered by the Large Hadron Collider at a centre-of-mass energy of 13 TeV and recorded by the ATLAS detector between 2015 and 2018. The data correspond to an integrated luminosity of 140 fb^{-1}. The sum of the WH and ZH cross-sections times the $H \to WW^*$ branching fraction is measured to be $0.44^{+0.10}_{-0.09}$ (stat.) $^{+0.06}_{-0.05}$ (syst.) pb, in agreement with the Standard Model prediction. Higgs boson production is further characterised through measurements of the differential cross-section as a function of the transverse momentum of the vector boson and in the framework of Simplified Template Cross-Sections.

Keywords: Hadron-Hadron Scattering

ArXiv ePrint: 2503.19420

https://doi.org/10.1007/JHEP08(2025)034

Contents

1 Introduction

Higgs boson production with a W or Z boson, respectively denoted by WH and ZH and collectively referred to as VH associated production, provides direct access to the Higgs boson couplings to weak bosons. In the case of VH associated production with a subsequent

JHEP08(2025)034

$H \to WW^*$ decay, the Higgs boson couples only to vector bosons at both the production and decay vertices, allowing these couplings to be precisely measured and providing a stringent test of the Standard Model (SM) of particle physics. Statistically significant deviations from their expected values could indicate beyond the SM effects; for example, the presence of additional Higgs bosons [1, 2] or new heavy vector bosons [3, 4].

Measurements are presented of the total and differential WH and ZH production cross-sections in the $H \to WW^*$ decay channel, using proton-proton (pp) collisions at a centre-of-mass energy of $\sqrt{s} = 13$ TeV. The data correspond to an integrated luminosity of $140\,\text{fb}^{-1}$ and were recorded by the ATLAS detector [5] at the Large Hadron Collider (LHC) [6] between 2015 and 2018. Previous measurements were performed by the ATLAS [7] and CMS [8] collaborations at $\sqrt{s} = 7$ and 8 TeV and more recently by the CMS collaboration [9] at $\sqrt{s} = 13$ TeV using $137\,\text{fb}^{-1}$ of data. The latest result from the ATLAS collaboration used data from 2015 and 2016 with an integrated luminosity of $36.1\,\text{fb}^{-1}$ [10]. In the $H \to WW^*$ decay channel, measurements of Higgs boson production via gluon-gluon fusion (ggF) and vector-boson fusion (VBF) at $\sqrt{s} = 13$ TeV have also been performed by the ATLAS [11] and CMS [9] collaborations, and VH production has been studied in other decay modes including $H \to ZZ^* \to 4\ell$ [12, 13], $H \to \gamma\gamma$ [14, 15], $H \to b\bar{b}$ [16, 17], and $H \to \tau\tau$ [18, 19].

The analysis is performed using events with two (2ℓ), three (3ℓ), or four (4ℓ) charged leptons (electrons or muons) in the final state, targeting the WH and ZH channels. In the 2ℓ channel, both opposite-sign (OS) and same-sign (SS) lepton pair configurations are considered. Leptonic decays of τ-leptons resulting from the decays of the associated W/Z bosons or the W bosons from the $H \to WW^*$ decay are considered as signal, while no specific selection is performed for events with hadronically decaying τ-leptons in the final state. Events from VH production with $H \to \tau\tau$ are considered as background. Additionally, events from ggF and VBF production are also considered as background.

In each channel, multivariate discriminants are used to maximise the sensitivity to the Higgs boson signal. The distributions of these discriminants are combined in a binned maximum-likelihood fit to extract the signal yield and the background normalisations. The maximum-likelihood fit provides results for the WH and the ZH channels separately and for their combination VH. The VH fit is performed assuming the SM prediction for the relative cross-sections of the WH and ZH production processes. Cross-section measurements are also performed in bins of the transverse momentum, p_{T}, of the associated vector boson, p_{T}^V, (defined as the "p_{T}^V scheme" in the following) and in kinematic fiducial regions defined according to the Simplified Template Cross-Section (STXS) framework [20–22] (defined as the "STXS scheme" in the following).

The outline of the paper is as follows: section 2 provides an overview of the signal characteristics and the analysis strategy and a description of the STXS framework, section 3 describes the ATLAS detector, section 4 describes the data and the simulated event samples, section 5 describes the event reconstruction, section 6 details the various selections used to define the signal regions in the analysis, section 7 discusses how the backgrounds are estimated and includes the definitions of the control regions, and section 8 provides commentary on the systematic uncertainties. Finally, section 9 defines the likelihood fit procedure and presents the results of the analysis, which are summarised in section 10.

JHEP08(2025)034

2 Analysis overview

Higgs boson production with a W or Z boson, followed by a $H \to WW^*$ decay, is sought using events with two, three, or four charged leptons in the final state. The analysis is designed to select events which are kinematically consistent with the WH and ZH, $H \to WW^*$ processes in order to enhance the signal-to-background ratio. The channels are defined as follows:

(1) **Opposite-sign 2ℓ channel**: the targeted signal contribution consists of a VH process in which the associated weak boson V decays hadronically and produces two energetic jets, while W bosons from the $H \to WW^*$ decay produce two oppositely charged leptons and two neutrinos. The leading-order Feynman diagram for this process is shown in figure 1(a). After requiring two leptons of different flavour, the leading backgrounds for this channel are $t\bar{t}$ and Wt processes. Other major components are $Z \to \tau\tau$ and WW production with two associated jets. Final states including W+jets and multijets may produce mis-identified leptons, contaminating the signal region. Other background sources include WZ production and other processes involving the Higgs boson, in particular its production through ggF;

(2) **Same-sign 2ℓ channel**: the targeted signal contribution consists of a WH process in which the associated W boson decays leptonically, while for the $H \to WW^*$ decay, the W boson with the same sign as the associated W boson decays leptonically and the other W boson decays hadronically. The final state therefore contains two leptons with the same charge, two neutrinos, and two energetic jets. The leading-order Feynman diagram for this process is shown in figure 1(b). Significant backgrounds in this channel include WZ, $W+\gamma$, and W+jets production; WW, $Z+\gamma$, Z+jets, and top-quark processes also contribute to this final state;

(3) **3ℓ channel**: the targeted signal contribution consists of a WH process where all weak bosons decay leptonically producing three charged leptons and three neutrinos in the final state. The leading-order Feynman diagram for this process is shown in figure 1(c). The most prominent background to this channel is WZ production. Non-resonant WWW production is another significant background with the same final state as the signal. Other important backgrounds are ZZ, $Z+\gamma$, Z+jets, $t\bar{t}$, and Wt production;

(4) **4ℓ channel**: the targeted signal contribution consists of a ZH process where all weak bosons decay leptonically producing four charged leptons and two neutrinos in the final state. The leading-order Feynman diagram for this process is shown in figure 1(d). The main backgrounds to this channel are non-resonant ZZ and WWZ production.

The selections defining the channels described above are mutually exclusive due to the requirements on the respective multiplicity and total charge of the leptons. To maximise the analysis sensitivity to the VH, $H \to WW^*$ process in each of these event topologies, the data samples for each channel — except for the opposite-sign 2ℓ channel — are further subdivided into several signal regions (SRs). Additional kinematic regions, with orthogonal selection criteria and designated as control regions (CRs), are used to determine normalisation factors that are applied to the major backgrounds in each SR.

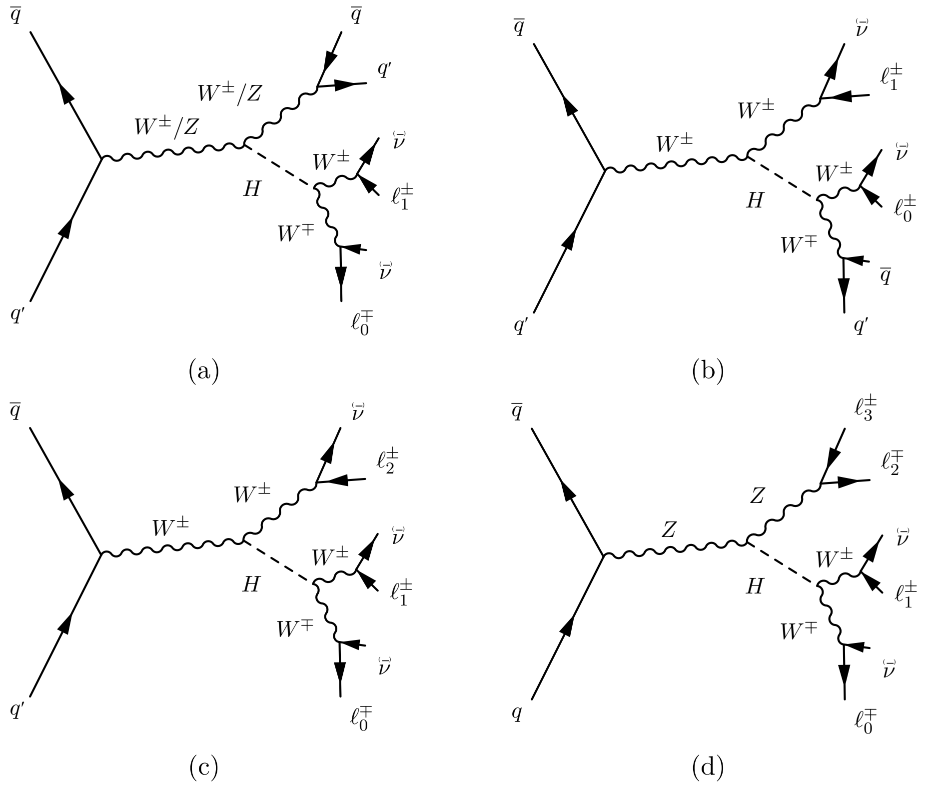

Figure 1. Leading-order Feynman diagrams for the signal topologies considered by the VH, $H \to WW^*$ measurement. The subscripts on the leptons are defined for the individual channels in section 6: (a) the opposite-sign 2ℓ channel, (b) the same-sign 2ℓ channel, (c) the 3ℓ channel, and (d) the 4ℓ channel.

A multivariate analysis is performed in all analysis channels to increase the sensitivity. The most suitable type of multivariate analysis, its configuration, and the set of input variables are chosen for each channel. Specifically, the setup providing the best separation of signal from background is selected and less complex setups are preferred if they provide the same performance. The 2ℓ and 3ℓ channels use neural networks based on Keras [23] with the TensorFlow [24] backend, and the 4ℓ channel uses boosted decision trees (BDTs) in TMVA [25].

The final results are extracted from a fit that simultaneously considers all SRs and CRs. The final results consist of a set of parameters of interest (POIs) which scale the SM expectations for the signal yields or cross-sections to match the observed data. The 3ℓ and 4ℓ are the most sensitive channels for the measurements of WH and ZH production, respectively, and for the overall measurement of VH production.

Cross-section measurements of VH are also conducted using the Stage 1.2 scheme of the STXS framework [20–22], which splits the production modes of the Higgs boson into kinematic fiducial regions or “categories” which are theoretically relevant, experimentally accessible, and straightforward to statistically combine. In this framework, the VH STXS category assumes a leptonic decay of the V and is further categorised according to its transverse momentum, p_{T}^{V}; in contrast, the $q\bar{q} \to V(\to q\bar{q})H$ (along with VBF) and $gg \to Z(\to q\bar{q})H$ (along with ggF) topologies are included in the electroweak (EW) qqH and ggH STXS categories, respectively.

JHEP08(2025)034

In the STXS measurement scheme, WH and ZH are measured independently in fiducial bins of p_{T}^{V} and $q\bar{q} \to V(\to q\bar{q})H$ is measured as part of EW qqH in a single fiducial bin of dijet invariant mass, m_{jj}. In addition, the limited interference between $q\bar{q} \to V(\to q\bar{q})H$ and VBF in the phase space relevant for this analysis motivates the use of the p_{T}^{V} measurement scheme, which is inclusive in the decay of the V. In the p_{T}^{V} scheme, the sensitivity to low values of p_{T}^{V} is primarily enabled by the $V(\to \text{leptons})H$ measurements, while the sensitivity to high values of p_{T}^{V} is primarily enabled by the $V(\to q\bar{q})H$ measurements. In both schemes, fiducial bins are merged to provide sensitivity for all measured parameters. This leads to measuring four bins of VH in the p_{T}^{V} scheme and three bins for each of WH and ZH as well as one bin for EW qqH in the STXS scheme.

3 ATLAS detector

The ATLAS detector [5] at the LHC covers nearly the entire solid angle around the collision point.[1] It consists of an inner tracking detector surrounded by a thin superconducting solenoid, electromagnetic and hadron calorimeters, and a muon spectrometer incorporating three large superconducting air-core toroidal magnets.

The inner-detector system (ID) is immersed in a 2 T axial magnetic field and provides charged-particle tracking in the range of $|\eta| < 2.5$. The high-granularity silicon pixel detector covers the vertex region and typically provides four measurements per track, the first hit normally being in the insertable B-layer (IBL) [26, 27]. It is followed by the silicon microstrip tracker (SCT), which usually provides eight measurements per track. These silicon detectors are complemented by the transition radiation tracker (TRT), which enables radially extended track reconstruction up to $|\eta| = 2.0$. The TRT also provides electron identification information based on the fraction of hits (typically 30 in total) above a higher energy-deposit threshold corresponding to transition radiation.

The calorimeter system covers the pseudorapidity range $|\eta| < 4.9$. In the region $|\eta| < 3.2$, electromagnetic calorimetry (EM) is provided by barrel and endcap high-granularity lead/liquid-argon (LAr) calorimeters, with an additional thin LAr presampler covering $|\eta| < 1.8$ to correct for energy loss in material upstream of the calorimeters. Hadron calorimetry is provided by the steel/scintillator-tile calorimeter, segmented into three barrel structures within $|\eta| = 1.7$, and two copper/LAr hadron endcap calorimeters. The solid angle coverage is completed with forward copper/LAr and tungsten/LAr calorimeter modules optimised for electromagnetic and hadronic energy measurements respectively.

The muon spectrometer (MS) comprises separate trigger and high-precision tracking chambers measuring the deflection of muons in a magnetic field generated by the superconducting air-core toroidal magnets. The field integral of the toroids ranges between 2.0 and 6.0 T m across most of the detector. Three layers of precision chambers, each consisting of layers of monitored drift tubes, cover the region $|\eta| < 2.7$, complemented by cathode-strip

[1] ATLAS uses a right-handed coordinate system with its origin at the nominal interaction point (IP) in the centre of the detector and the z-axis along the beam pipe. The x-axis points from the IP to the centre of the LHC ring, and the y-axis points upwards. Cylindrical coordinates (r, ϕ) are used in the transverse plane, ϕ being the azimuthal angle around the z-axis. The pseudorapidity is defined in terms of the polar angle θ as $\eta = -\ln\tan(\theta/2)$. Angular distance is measured in units of $\Delta R \equiv \sqrt{(\Delta\eta)^2 + (\Delta\phi)^2}$.

chambers in the forward region, where the background is highest. The muon trigger system covers the range $|\eta| < 2.4$ with resistive-plate chambers in the barrel, and thin-gap chambers in the endcap regions.

Events of interest are selected by the first-level trigger system implemented in custom hardware, followed by selections made by algorithms implemented in software in the high-level trigger [28]. The first-level trigger accepts events from the 40 MHz bunch crossings at a rate below 100 kHz, which the high-level trigger reduces further to record events to disk at about 1 kHz. The full ATLAS Run 2 data sample is used for the analysis, consisting of *pp* collision data produced at $\sqrt{s} = 13$ TeV and recorded between 2015 and 2018. The data are subjected to quality requirements [29], including the removal of events recorded when relevant detector components were not operating correctly. The total integrated luminosity after this cleaning of the data corresponds to 140 fb^{-1} [30].

An extensive software suite [31] is used in the reconstruction and analysis of real and simulated data, in detector operations, and in the trigger and data acquisition systems of the experiment.

4 Monte Carlo samples

Monte Carlo (MC) generators are used to model the hard *pp* scattering matrix element (ME), parton shower (PS) and hadronisation, and underlying event (UE). The generators that are used for modelling signal and background processes are listed in table 1.

The Higgs boson samples are simulated with the $H \to WW^*$ decay in the four main production channels: ggF, VBF, VH, and associated production with a top quark pair ($t\bar{t}H$). These samples are simulated using a Higgs boson mass of 125 GeV and then normalised to the cross-sections [21] computed for a mass of 125.09 GeV [32]. The normalisation of all Higgs boson samples accounts for the decay branching ratio calculated with HDECAY [33–35] and Prophecy4f [36–38]. All samples use the PDF4LHC15 [39] parton distribution function (PDF) set and are interfaced to Pythia 8.2 [40] for parton showering and hadronisation, with parameters set according to the AZNLO [41] (for VH, ggF, and VBF) or A14 [42] (for $t\bar{t}H$) set of tuned parameters (tunes). The decays of bottom and charm hadrons are performed using EvtGen [43].

The WH and ZH events are simulated at next-to-leading order (NLO) in perturbative quantum chromodynamics (QCD) for up to one additional jet using Powheg Box v2 MiNLO [44–48]. Each sample is normalised to a cross-section calculated at next-to-next-to-leading-order (NNLO) in QCD and at NLO in EW [49–53]. The subdominant $gg \to ZH$ process is simulated at leading-order (LO) in QCD with Powheg Box v2 and normalised to a cross-section calculated at NLO in QCD with next-to-leading logarithmic (NLL) corrections [54, 55].

The ggF events are simulated using Powheg Box v2 NNLOPS [56]. The simulation achieves NNLO accuracy for arbitrary inclusive $gg \to H$ observables by reweighting the Higgs boson rapidity spectrum in Hj-MiNLO [57–59] to that of HNNLO [60]. The sample is normalised to a cross-section computed at next-to-next-to-next-to-leading-order (N^{3}LO) in QCD with NLO EW corrections [21, 61–70]. The VBF events are simulated using Powheg Box v2 and normalised to a cross-section calculated at NLO in QCD and EW [71, 72], with approximate NNLO in QCD corrections applied [73]. The $t\bar{t}H$ events are simulated using POWHEG BOX v2 [74, 75] at NLO accuracy in QCD. The sample is normalised to a cross-section computed at NLO accuracy in QCD with NLO EW corrections [21].

The main background processes include single boson, diboson, triboson, single top quark, and top quark pair production.

The Z/γ^* ("Z+jets") processes are simulated using SHERPA 2.2.1 [76] at NLO in QCD for up to two jets and at LO for up to four jets, calculated using the COMIX [77] and OPENLOOPS [78–80] libraries. The single boson samples are normalised to cross-sections computed at NNLO in QCD [81]. The VV and $V{+}\gamma$ processes are simulated using SHERPA 2.2.2 and SHERPA 2.2.8, respectively, at NLO in QCD for up to one jet and at LO for up to three jets. Throughout the paper, WZ and ZZ are assumed to correspond to $WZ/W\gamma^*$ and $ZZ/Z\gamma^*$, respectively (i.e., including the virtual photon contribution). The on-shell VVV processes are modelled by SHERPA 2.2.2 at NLO in QCD inclusively and at LO for up two jets. Virtual QCD corrections to the VV, $V{+}\gamma$, and VVV processes were provided by the OPENLOOPS library [78–80, 82]. The gg-initiated diboson processes are modelled by SHERPA 2.2.2 at LO in QCD for up to one jet and normalised to cross-sections computed at NLO in QCD [83, 84]. For all SHERPA samples, the events are simulated using the NNPDF3.0NNLO [85] PDF set, and the matrix elements are matched with the SHERPA parton shower [77, 86] using the MEPS@NLO prescription [87–90] and the set of tuned parameters developed by the SHERPA authors. EW WW production in association with two jets ($WWqq$) is simulated using MADGRAPH5_AMC@NLO [91] with LO-accurate matrix elements [83] and using the NNPDF3.0NLO [85] PDF set. The events are interfaced to PYTHIA 8 for parton showering and hadronisation, with parameters set according to the A14 tune.

The top quark pair production is modelled by POWHEG BOX v2 at NLO in QCD with the h_{damp} parameter[2] set to $1.5\times m_{\mathrm{top}}$ [92]. The events are normalised to a cross-section computed at NNLO in QCD with next-to-next-to-leading logarithmic (NNLL) corrections [93–99]. The Wt process is simulated using POWHEG BOX v2 [100] at NLO in QCD using the five-flavour scheme. The diagram removal scheme [101] is used to remove interference and overlap with $t\bar{t}$ production. The $t\bar{t}V$, tZ, and tWZ processes are simulated using MADGRAPH5_AMC@NLO at NLO in QCD. For all top processes, events are simulated using the NNPDF3.0NLO PDF set. EVTGEN is used to model decays of hadrons containing b- or c-quarks, and the events are interfaced to PYTHIA 8 for parton showering and hadronisation, with parameters set according to the A14 tune.

All samples are processed through the GEANT4-based [102] ATLAS detector simulation [103] and the standard ATLAS reconstruction software [104]. The effect of pile-up is modelled by overlaying the hard-scattering event with simulated inelastic pp events simulated with PYTHIA 8.1 [105] using the NNPDF2.3LO [106] PDF set and the A3 [107] tune.

[2]The h_{damp} parameter is a resummation damping factor and one of the parameters that controls the matching of POWHEG matrix elements to the parton shower and thus effectively regulates the high-p_{T} radiation against which the $t\bar{t}$ system recoils.

Process	ME (alternative)	PS/UE (alternative)	Prediction order for total cross-section
$q\bar{q} \to WH$	POWHEG BOX v2 MINLO	PYTHIA 8 (HERWIG 7 [108, 109])	NNLO QCD + NLO EW [49–53]
$q\bar{q} \to ZH$	POWHEG BOX v2 MINLO	PYTHIA 8 (HERWIG 7)	NNLO QCD + NLO EW [49–53]
$gg \to ZH$	POWHEG BOX v2	PYTHIA 8 (HERWIG 7)	NLO + NLL [54, 55]
ggF H	POWHEG BOX v2 NNLOPS	PYTHIA 8	N^{3}LO QCD + NLO EW [21, 61–70]
VBF H	POWHEG BOX v2	PYTHIA 8	NNLO QCD + NLO EW [71–73]
$t\bar{t}H$	POWHEG BOX v2	PYTHIA 8	NLO QCD + NLO EW [21]
Z/γ^*	SHERPA 2.2.1 (MADGRAPH5_AMC@NLO)	SHERPA 2.2.1 (PYTHIA 8)	NNLO [81]
$q\bar{q}/g \to WW$	SHERPA 2.2.2	SHERPA 2.2.2	NLO [78–80]
$WZ/ZZ/V\gamma^*$	SHERPA 2.2.2	SHERPA 2.2.2	NLO [110]
$V{+}\gamma$	SHERPA 2.2.8	SHERPA 2.2.8	NLO [110]
$gg \to WW/ZZ$	SHERPA 2.2.2	SHERPA 2.2.2	NLO [83, 84]
VVV	SHERPA 2.2.2 (MADGRAPH5_AMC@NLO)	SHERPA 2.2.2 (PYTHIA 8)	NLO [111]
$qq \to WWqq$	MADGRAPH5_AMC@NLO	PYTHIA 8	LO
$t\bar{t}$	POWHEG BOX v2 (MADGRAPH5_AMC@NLO)	PYTHIA 8 (HERWIG 7)	NNLO + NNLL [93–99]
Wt	POWHEG BOX v2	PYTHIA 8	NLO [112, 113]
$t\bar{t}V$	MADGRAPH5_AMC@NLO	PYTHIA 8	NLO [114]
tZ	MADGRAPH5_AMC@NLO	PYTHIA 8	NLO [115]
tWZ	MADGRAPH5_AMC@NLO	PYTHIA 8	NLO [116]

Table 1. MC generators used to model the signal and background processes. Alternative generators or parton shower models — used to estimate systematic uncertainties — are shown in parenthesis. In the last column, the prediction order (in QCD, unless specified otherwise) for the total cross-section is shown.

5 Event reconstruction

Candidate signal events are selected using triggers that require a single isolated lepton with minimum p_{T} thresholds ranging from 24 to 26 GeV for electrons and from 20 to 26 GeV for muons [117, 118], depending on the data-taking period. At least one of the leptons reconstructed offline is required to have triggered the event. Additionally, the lepton is required to have a reconstructed p_{T} higher than the nominal trigger threshold by at least 1 GeV, which ensures that the p_{T} is squarely on the plateau of the trigger's efficiency.

Selected events are required to have at least one primary vertex reconstructed from at least two matched tracks, each with transverse momentum $p_{\mathrm{T}} > 500$ MeV, as described in ref. [119]. If an event has more than one reconstructed primary vertex, the vertex with the largest track $\sum p_{\mathrm{T}}^2$ is selected for the analysis.

Electrons are reconstructed by matching energy clusters in the electromagnetic calorimeter to well-reconstructed tracks that are extrapolated to the calorimeter [120]. Electron candidates are required to satisfy $|\eta| < 2.47$, excluding the transition region $1.37 < |\eta| < 1.52$ between the barrel and end caps of the LAr calorimeter.

Muons are reconstructed from a global fit to matching tracks from the ID and the MS [121]. They are required to satisfy $|\eta| < 2.5$.

For the purpose of lepton counting, all leptons with $p_{\mathrm{T}} > 10\,\mathrm{GeV}$ and passing a set of identification requirements common to all channels are included. This ensures orthogonality between the channels when divided according to an exact lepton multiplicity and total charge.

To suppress particles mis-identified as leptons, several identification, impact parameter, and isolation criteria are applied to electron and muon candidates, shown in table 2. For electrons, a likelihood-based identification method [122] is employed. Electron candidates in the 2ℓ and 3ℓ channels must satisfy the "Tight" likelihood working point, while electron candidates in the 4ℓ channel must satisfy the "Medium" likelihood working point. The "Tight" and "Medium" working points have identification efficiencies of ∼78% and ∼88%, respectively, for electrons with $p_{\mathrm{T}} \sim 40\,\mathrm{GeV}$. For muons, a cut-based identification method [121] is employed. Muon candidates must satisfy the "Medium" working point, which has an identification efficiency of ∼96% for muons with $p_{\mathrm{T}} \sim 40\,\mathrm{GeV}$. The impact parameter requirements are $|z_0 \sin\theta| < 0.5\,\mathrm{mm}$ and $|d_0|/\sigma_{d_0} < 5$ (3) for electrons (muons).[3] Electron candidates in the 2ℓ and 3ℓ channels must also be unambiguously reconstructed as electrons; they cannot be simultaneously reconstructed as photons.

For 2ℓ and 3ℓ channels, a newly developed multivariate method based on a BDT, the prompt lepton improved veto (PLIV), is employed. PLIV exploits isolation and lifetime information — including the presence of secondary vertices — associated with a track jet matched to the selected lepton candidate. It leads to a substantial improvement in the rejection of mis-identified leptons compared to previously available methods within ATLAS while maintaining high efficiency for selecting prompt leptons. Lepton candidates in the 2ℓ and 3ℓ channels must satisfy the "PLImprovedTight" working point. For electrons, this working point has prompt and non-prompt electron efficiencies of ∼95% and ∼4%, respectively, for electrons with $p_{\mathrm{T}} \sim 40\,\mathrm{GeV}$ and $|\eta| < 1.37$; for muons, this working point has prompt and non-prompt muon efficiencies of ∼95% and ∼3%, respectively, for muons with $p_{\mathrm{T}} \sim 40\,\mathrm{GeV}$. Electron and muon candidates in the 4ℓ channel must satisfy the cut-based "FCLoose" and "Loose_VarRad" working points, respectively, which rely on tracking and calorimeter isolation variables [121, 122]. The "FCLoose" working point has an isolation efficiency of ∼99% for electrons with $p_{\mathrm{T}} \sim 40\,\mathrm{GeV}$ and passing the "Medium" identification working point, and the "Loose_VarRad" working point has a prompt muon efficiency of 97% and an efficiency for muons from heavy-flavour decays of 6.1% for muons with $20 < p_{\mathrm{T}} < 100\,\mathrm{GeV}$ and passing the "Medium" identification working point. To suppress electron charge mis-identification in the same-sign 2ℓ channel and the 3ℓ channel with zero same-flavour, opposite-sign lepton pairs in the final state, another BDT discriminant, the electron charge identification selector (ECIDS) [122], is used.

[3]The transverse impact parameter, d_0, is defined by the point of closest approach of the track to the beamline in the r–ϕ plane, its uncertainty being σ_{d_0}, while the longitudinal impact parameter, z_0, is given by the longitudinal distance to the hard-scatter vertex from this same point.

JHEP08(2025)034

	Flavour	
Criteria	Electrons	Muons
p_{T} [GeV]	> 10	
$\|\eta\|$	< 1.37 or $\in [1.52, 2.47]$	< 2.5
Identification	Tight (Medium)	Medium
$\|z_0 \sin\theta\|$ [mm]	< 0.5	
$\|d_0/\sigma_{d_0}\|$	< 5	< 3
Unambiguous e/γ	Yes (No)	—
Isolation	PLImprovedTight (FCLoose)	PLImprovedTight (Loose_VarRad)
ECIDS	Yes* (No)	—

Table 2. The electron and muon definitions used by the analysis. Any selection in brackets, (...), is specific to the 4ℓ channel and is used instead of the preceding selection on that same line of the table; otherwise, the selections are applicable to all channels. *ECIDS is only applied to the same-sign 2ℓ channel and the 3ℓ channel with zero same-flavour, opposite-sign lepton pairs in the final state.

Jets are reconstructed using the anti-k_t algorithm with a radius parameter of $R = 0.4$ and particle-flow objects as input [123–125]. The four-momentum of the jets is corrected for the response of the non-compensating calorimeter, signal losses due to noise threshold effects, energy loss in inactive material, and contamination from pile-up (defined as additional pp interactions in the same and neighbouring bunch crossings) [126]. For jets entering the analysis, a kinematic selection of $p_{\mathrm{T}} > 20$ GeV and $|\eta| < 4.5$ is applied. For the purpose of jet counting, only jets with $p_{\mathrm{T}} > 30$ GeV are considered. A jet-vertex-tagger multivariate discriminant selection that reduces contamination from pile-up [127] is applied to jets with $20 < p_{\mathrm{T}} < 60$ GeV and $|\eta| < 2.4$, utilising calorimeter and tracking information to separate hard-scatter jets from pile-up jets. Furthermore, to suppress pile-up jets in the forward region, $|\eta| > 2.5$, jet shapes and topological correlations in pile-up interactions are exploited [128, 129].

Jets with $p_{\mathrm{T}} > 20$ GeV and $|\eta| < 2.5$ containing b-hadrons (b-jets) are identified using a neural-network discriminant, DL1r, based on a number of lower-level taggers which utilise relevant quantities such as the associated track impact parameters and information from secondary vertices. The working point that is adopted has an average 85% b-jet tagging efficiency, as estimated from simulated $t\bar{t}$ events [130, 131].

The missing transverse momentum $\vec{p}_{\mathrm{T}}^{\mathrm{miss}}$, with magnitude $E_{\mathrm{T}}^{\mathrm{miss}}$, is calculated as the negative vector sum of the p_{T} of all the selected leptons and jets, together with reconstructed tracks that are not associated with these objects but are consistent with originating from the primary vertex [132]. It serves as experimental proxy for the momentum carried by undetected particles. An object-based $E_{\mathrm{T}}^{\mathrm{miss}}$ significance [132], $\mathcal{S}_{\mathrm{miss}}$, is used to reject events where the $E_{\mathrm{T}}^{\mathrm{miss}}$ arises due to the mis-reconstruction of the physics objects entering the calculation.

Channel	2ℓ		3ℓ		4ℓ	
	OS	SS	Z-dominated	Z-depleted	1-SFOS	2-SFOS
Minimum lepton p_{T} [GeV]	15	15	15	15	10	10
Number of leptons	2	2	3	3	4	4
Total lepton charge	0	± 2	± 1	± 1	0	0
Number of SFOS pairs	0	—	1 or 2	0	1	2
Number of DFOS pairs	1	—	—	—	—	—
Minimum $\Delta R_{\ell\ell}$	0.1	0.4	0.1	0.1	0.2 ($\ell_0\ell_1$)	
Minimum $m_{\ell\ell}$ [GeV]	10	—	12 (all SFOS)	—	12 (all SFOS) or 10 (all DFOS)	
Number of jets	≥ 2	≥ 1	—	—	—	—
Number of b-tagged jets	0	0	0	0	0	0
$\lvert m_{\ell\ell} - m_Z\rvert$ [GeV]	—	> 20 ($e^{\pm}e^{\pm}$)	> 25 (all SFOS)	—	—	—
$m_{\ell\ell}$ [GeV]	—	—	—	—	—	< 50 ($\ell_0\ell_1$)
$E_{\mathrm{T}}^{\mathrm{miss}}$ [GeV]	—	—	> 30	—	—	—
$\lvert m_{jj} - 85\,\mathrm{GeV}\rvert$ [GeV]	< 15	—	—	—	—	—
m_{jj} [GeV]	—	< 500	—	—	—	—
$\lvert\Delta y_{jj}\rvert$	< 1.2	—	—	—	—	—
$\lvert m_{4\ell} - 122.5\,\mathrm{GeV}\rvert$ [GeV]	—	—	—	—	—	> 7.5
$\mathrm{ANN}^{VH}_{\mathrm{DFOS}}$	> 0.2	—	—	—	—	—
$\mathrm{ANN}^{t\bar{t}}_{\mathrm{Zdep}}$	—	—	—	< 0.25	—	—

Table 3. Definition of the event selection for each SR in the analysis before applying multivariate techniques. The selections are defined and motivated for all channels in their respective subsections of section 6. "SFOS" and "DFOS" refer to same- and different-flavour, opposite-sign lepton pairs, respectively. In the context of the 4ℓ channel, leptons 0 and 1, ℓ_0 and ℓ_1, comprise the Higgs boson candidate — this is described in greater detail in section 6.4.

6 Event selection

In this section, the criteria used to define the SR in each channel are described. Table 3 summarises the selections for each channel before applying multivariate techniques. In table 3 and throughout this section, the minimum lepton p_{T} selections are smaller than the p_{T} thresholds of the single lepton triggers. While at least one lepton must have triggered the event and therefore satisfy one of these higher thresholds, all leptons must satisfy minimum p_{T} selections.

The multivariate techniques applied in each channel are also described in greater detail in this section. The variables used as input by each technique have been confirmed to exhibit good consistency with data in the phase space regions where the technique is trained and deployed.

6.1 Opposite-sign 2ℓ channel

The opposite-sign 2ℓ channel requires two different-flavour, opposite-sign (DFOS) leptons from the decay of the Higgs boson, labelled ℓ_0 and ℓ_1 in decreasing order of p_{T}, and two or more jets from the decay of the associated vector boson, which can be either a W or a Z. The leading and subleading leptons must exceed p_{T} thresholds of 22 GeV and 15 GeV, respectively, and are required to satisfy the common lepton selections. The invariant mass of the leptons must satisfy $m_{\ell\ell} > 10\,\mathrm{GeV}$ to remove low-mass resonances, and the angular separation

JHEP08(2025)034

between the leptons must satisfy $\Delta R_{\ell\ell} > 0.1$ to remove overlapping leptons. To reject top quark production, events with at least one b-jet are vetoed. To ensure orthogonality with the ATLAS ggF and VBF production measurements [11], the leading dijet system is required to have an invariant mass of $|m_{jj} - 85\,\text{GeV}| < 15\,\text{GeV}$ and a rapidity separation of $|\Delta y_{jj}| < 1.2$.

An artificial neural network (ANN) is trained to simultaneously classify VH, ggF, VBF, top, Z+jets, and WW processes; ggF and VBF correspond to the dominant Higgs boson backgrounds, and top, Z+jets, and WW correspond to the dominant non-Higgs boson backgrounds. The output consists of six distinct output nodes, $\text{ANN}^{i}_{\text{DFOS}}$, each describing the likeliness of the input event to stem from process i ($i = VH$, ggF, VBF, top, Z+jets, and WW) with the condition that $\sum_i \text{ANN}^{i}_{\text{DFOS}} = 1$. Different nodes are needed to build dedicated control regions to normalise the relevant background processes, as explained in section 7. In total, 19 variables are used as input — these are summarised in table 15 of appendix A. Variables including the dilepton invariant mass, $m_{\ell\ell}$, and azimuthal separation, $\Delta\phi_{\ell\ell}$, are useful for separating Higgs boson production from background processes, and variables including the dijet invariant mass, m_{jj}, and rapidity separation, $|\Delta y_{jj}|$, are useful for independently separating VH and VBF production from all other processes. The Z+jets background is separated from other processes by means of the invariant mass of the τ-lepton pair using the collinear approximation [133], $m_{\tau\tau}$, and the top and WW backgrounds are separated from other processes by means of the transverse mass of the $H \to WW^*$ system, m_{T}:

$$m_{\text{T}} = \sqrt{2 p_{\text{T}}^{\ell\ell} E_{\text{T}}^{\text{miss}} \left(1 - \cos \Delta\phi_{\ell\ell,\text{miss}}\right)}\,, \tag{6.1}$$

where $p_{\text{T}}^{\ell\ell}$ is the transverse momentum of the dilepton system and $\Delta\phi_{\ell\ell,\text{miss}}$ is the azimuthal separation between the dilepton system and the $E_{\text{T}}^{\text{miss}}$. To construct the SR, the VH output node of the ANN is required to be greater than 0.2, corresponding to a signal efficiency of 80% and a background rejection of 77%.

Figure 2 shows distributions of $\text{ANN}^{VH}_{\text{DFOS}}$ and a signal-sensitive kinematic variable in the opposite-sign 2ℓ SR, as obtained from the fit procedure described in section 9.1 (hereafter called a “post-fit” distribution).

6.2 Same-sign 2ℓ channel

The same-sign 2ℓ channel selects exactly two same-sign isolated leptons with the leading lepton p_{T} above 22 GeV and subleading lepton p_{T} above 15 GeV. The leading and subleading leptons are labelled as ℓ_0 and ℓ_1, respectively. Events with at least one reconstructed jet are selected to maintain a high signal efficiency; the choice to require at least one jet instead of at least two jets is made because a significant fraction of simulated signal events, 57%, have only one reconstructed jet. The invariant mass of the leading dijet system, m_{jj}, is required to be below 500 GeV for events with two or more jets to suppress contributions from the same-sign WW process [134]. Events containing any b-tagged jets are vetoed to reject the top backgrounds. The angular separation between the leptons is required to be $\Delta R_{\ell\ell} > 0.4$ to suppress the W+γ events. The events are further split into SS2μ, SS2e, and SSDF channels according to the lepton flavour. The SS2e channel requires two electrons and vetoes events where the invariant mass of the electron pair is within ± 20 GeV of the Z pole — this suppresses Z+jets events, where the charge of an electron is reconstructed incorrectly.

JHEP08(2025)034

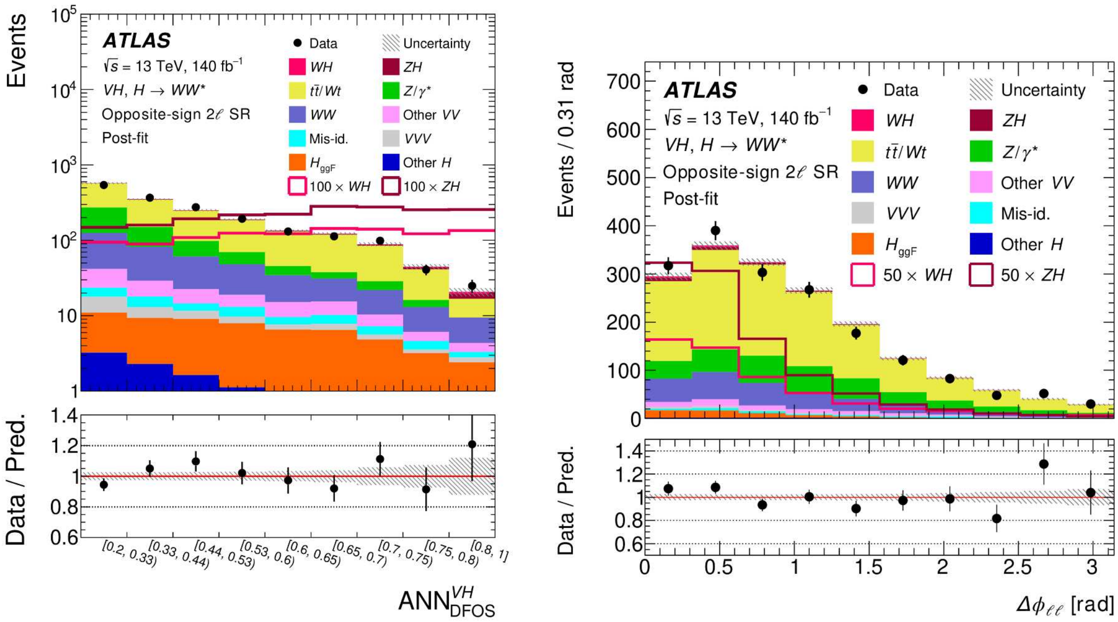

(a) (b)

Figure 2. Post-fit distribution of (a) $\mathrm{ANN}^{VH}_{\mathrm{DFOS}}$ and (b) the dilepton azimuthal separation, $\Delta\phi_{\ell\ell}$, in the opposite-sign 2ℓ SR. The post-fit WH and ZH signal yields are additionally overlaid and upscaled in both distributions. The lower panel shows the ratio of the data to the sum of the fitted signal and background. The hatched band shows the total uncertainty. The post-fit results are obtained from the combined 2-POI fit described in section 9.1. In all subsequent post-fit distributions, "Mis-id." is the mis-identified lepton background, as described in section 7.1.

The SS2μ channel requires two muons, and the SSDF channel requires one electron and one muon. The selections described above constitute the SS2μ, SS$2e$, and SSDF SRs.

The WZ process is the dominant background in the same-sign 2ℓ channel. A recurrent neural network (RNN) [135] is trained to distinguish WH from WZ, and the same RNN is used in each of the SS2μ, SS$2e$, and SSDF SRs. The RNN has the advantage of being able to learn sequential dependencies for arbitrary-length sequences of objects as input. This feature is used in the analysis where the number of jet variables depend on the jet multiplicity of the events.

The sequences provided to the RNN consist of reconstructed objects placed in order of leptons, $E_{\mathrm{T}}^{\mathrm{miss}}$, and jets (up to a maximum of five jets) with leptons and jets further ordered by p_{T}. The RNN uses the p_{T}, η, and ϕ of leptons and jets and the magnitude, $E_{\mathrm{T}}^{\mathrm{miss}}$, and the azimuthal angle, ϕ_{miss}, of the missing transverse momentum. A variable containing the information to distinguish between different particle types (leptons, missing transverse momentum, and jets) is also given as input to the RNN. The geometry of the ATLAS detector — and the physics — has a rotational symmetry in the ϕ direction and a mirror symmetry in the η direction. These symmetries are used to pre-process the input variables: the coordinate system of the sequence is rotated to keep the leading lepton with a ϕ coordinate of 0 and reflected to keep the leading lepton with a positive η coordinate. By doing so, the training data is used in a more efficient way as the RNN does not need to learn these symmetries in the training process.

JHEP08(2025)034

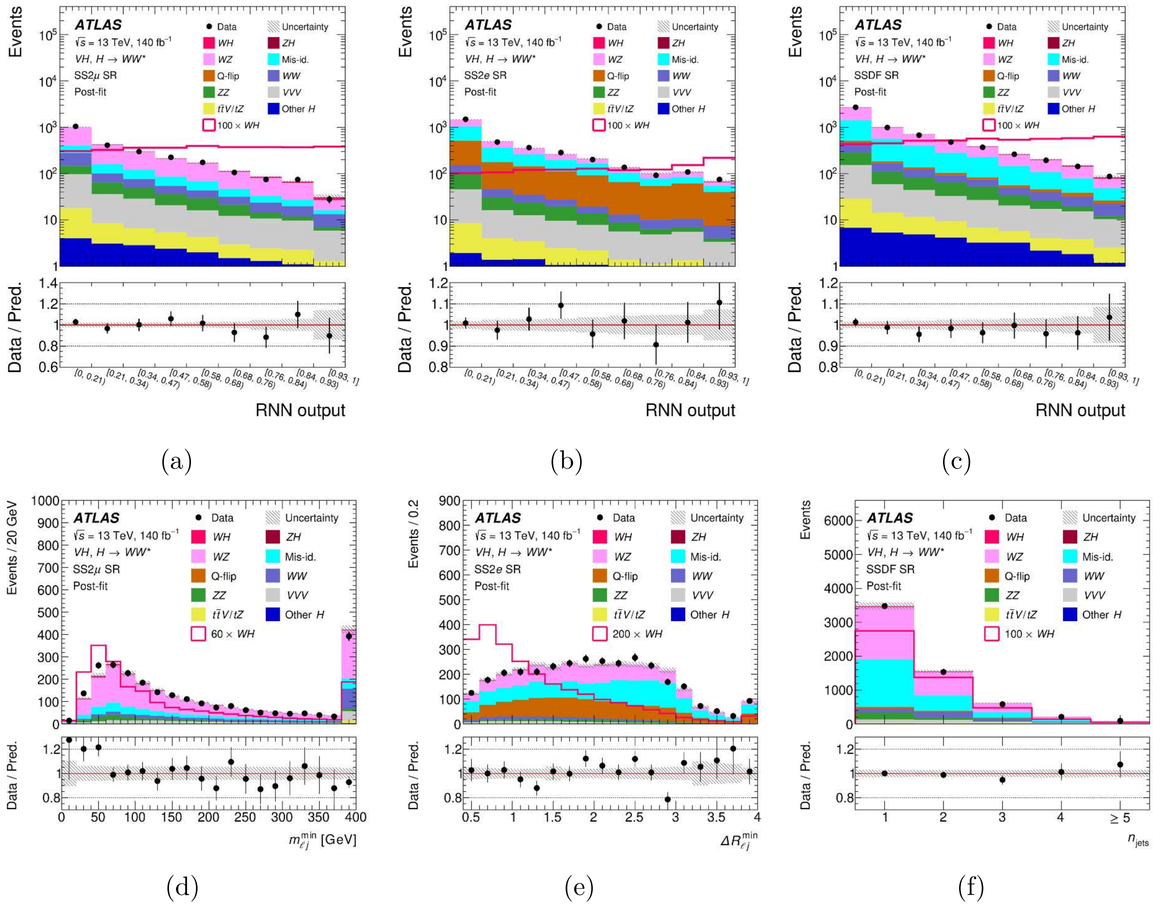

Figure 3. Post-fit distributions of the RNN discriminant in the (a) SS2μ, (b) SS2e, and (c) SSDF SRs and (d) the minimum value of the invariant mass of a lepton and jet in the SS2μ SR, (e) the minimum value of the ΔR between a lepton and a jet in the SS2e SR, and (f) the number of jets in the SSDF SR. The post-fit WH signal yields are additionally overlaid and upscaled in all distributions. The lower panel shows the ratio of the data to the sum of the fitted signal and background. The hatched band shows the total uncertainty. The last bin includes overflow, where applicable. The post-fit results are obtained from the combined 2-POI fit described in section 9.1. "Q-flip" is the electron background with mis-identified charge, as described in section 7.

Figure 3 shows the post-fit distributions of the RNN discriminants and signal-sensitive kinematic variables in the three same-sign 2ℓ SRs. In the SS2μ signal region, an RNN shape mis-modelling in WZ events, the largest background in that signal region, was observed. A correction to the RNN shape was evaluated using a validation region enriched in the WZ background and applied to each of the SS2μ, SS2e, and SSDF signal regions. A detailed description of this correction is given in section 7. A residual discrepancy between data and simulation is observed in the minimum value of the invariant mass of a lepton and jet, shown in figure 3(d). As described in section 7, this variable is sensitive to the mis-modelling in WZ events; however, unlike the RNN shape, this variable is not explicitly corrected as it does not directly enter the fit model.

JHEP08(2025)034

6.3 3ℓ channel

In the 3ℓ channel, exactly three isolated leptons with $p_T > 15\,\text{GeV}$ are required with a total charge of ± 1. The lepton with unique charge is labelled ℓ_0, the lepton closest to ℓ_0 in angular distance ΔR is labelled ℓ_1, and the remaining lepton is labelled ℓ_2. This labelling scheme is demonstrated pictorially in the leading-order Feynman diagram, figure 1(c). In signal events, leptons ℓ_0 and ℓ_1 are most likely to originate from the $H \to WW^*$ decay with probabilities of 99% and 85%, respectively.

The most prominent background processes in the 3ℓ channel are WZ production and top quark processes with either three prompt leptons (e.g., $t\bar{t}V$) or two prompt leptons and one non-prompt lepton from a b-hadron decay (e.g., $t\bar{t}$).

The analysis of the 3ℓ channel separates events with at least one same-flavour, opposite-sign charge (SFOS) lepton pair from events with zero SFOS lepton pairs, which have different signal-to-background ratios. Due to the presence of background processes with $Z \to \ell\ell$ decays as a dominant background, the former set of events is hereafter referred to as the Z-dominated channel, while the latter is referred to as the Z-depleted channel.

In the Z-dominated channel, the major background processes are those involving Z bosons. Therefore, the invariant mass, $m_{\ell\ell}$, for each SFOS pair is required to satisfy a Z-veto selection: $|m_{\ell\ell} - m_Z| > 25\,\text{GeV}$. To suppress background events from heavy-flavour quarkonia, the minimum invariant mass of all SFOS pairs is required to be greater than 12 GeV. Furthermore, the E_T^{miss} is required to be larger than 30 GeV to select final states with neutrinos. To suppress processes containing top quarks, events with at least one b-tagged jets are vetoed. To remove overlapping leptons, the angular separation between all lepton pairs must satisfy $\Delta R_{\ell\ell} > 0.1$. These selections constitute the Z-dominated SR.

For both the channels, dedicated ANNs are used to separate signal from background. In the Z-dominated channel, fifteen variables are used as input — these are summarised in table 16 of appendix A. The purpose of the single output classifier, ANN_{Zdom}, is to distinguish between the signal and the dominant WZ background. Accordingly, it is trained against this background process. The output is used as final discriminant in this channel. Particularly useful variables for separating WH and WZ production include the invariant mass of leptons 0 and 1, $m_{\ell_0\ell_1}$, as well as the angular distance between leptons 0 and 1, $\Delta R_{\ell_0\ell_1}$; also useful are the E_T^{miss} and E_T^{miss}-related variables such as the azimuthal separation between lepton 0 and the E_T^{miss}, $\Delta\phi_{\ell_0,\text{miss}}$.

In the Z-depleted channel, the three dominant background processes are $t\bar{t}$, WZ, and WWW. To simultaneously separate the WH signal from these backgrounds, a multi-classifier is used providing four distinct output nodes, $\text{ANN}^i_{\text{Zdep}}$, each describing the likeliness of the input event to stem from process i ($i = WH$, $t\bar{t}$, WZ, WWW) with the condition that $\sum_i \text{ANN}^i_{\text{Zdep}} = 1$. Table 17 of appendix A summarises the input variables used in the Z-depleted channel. The angular distance between leptons 0 and 1, $\Delta R_{\ell_0\ell_1}$, is particularly useful for separating WH production from background processes, and the E_T^{miss} and E_T^{miss}-related variables are useful for separating WH, $t\bar{t}$, and WZ production, which all have varying numbers of neutrinos in the final state. The transverse momentum of the leading jet, $p_T^{j_0}$, is useful for separating $t\bar{t}$ production from other processes, and the compatibility of the event with the $WZ(\to \tau\tau)$ hypothesis, F_α, is useful for separating WZ production from other processes. The latter variable is described in greater detail in the appendix.

To suppress processes containing top quarks, events with a high $\mathrm{ANN}^{t\bar{t}}_{\mathrm{Zdep}}$ score — greater than 0.25 — or at least one b-tagged jets are vetoed. Additionally, all lepton pairs must satisfy $\Delta R_{\ell\ell} > 0.1$ to remove overlapping leptons. These selections constitute the Z-depleted SR, whose final discriminant, $\mathrm{ANN}^{\Delta}_{\mathrm{Zdep}}$, is defined as:

$$\mathrm{ANN}^{\Delta}_{\mathrm{Zdep}} = \mathrm{ANN}^{WH}_{\mathrm{Zdep}} - \mathrm{ANN}^{WZ}_{\mathrm{Zdep}} - \mathrm{ANN}^{WWW}_{\mathrm{Zdep}}\,. \tag{6.2}$$

Figure 4 shows the post-fit distributions of the ANN discriminants and signal-sensitive kinematic variables in both the Z-dominated and Z-depleted SRs.

6.4 4ℓ channel

The ZH channel includes events with four isolated leptons with $p_{\mathrm{T}} > 10\,\mathrm{GeV}$ and total electric charge of zero. Events containing an SFOS lepton pair with $m_{\ell\ell} < 12\,\mathrm{GeV}$ or a DFOS lepton pair with $m_{\ell\ell} < 10\,\mathrm{GeV}$ are rejected to suppress the contamination from heavy-flavour quarkonia. Selected events are classified into channels according to the number of SFOS lepton pairs: 1-SFOS and 2-SFOS. Events with no SFOS lepton pairs are excluded.

The most prominent background process in the 4ℓ channel is ZZ production, with smaller contributions from top quark processes (e.g., $t\bar{t}Z$), processes with mis-identified leptons (e.g., $t\bar{t}W$), and WWZ production.

The reconstruction of the ZH process proceeds through the identification of the leptons from the Z boson, called ℓ_2 and ℓ_3, as the SFOS lepton pair with invariant mass closest to the mass of the Z boson. The remaining two leptons, labelled ℓ_0 and ℓ_1, are candidates for originating from the Higgs boson decay. This labelling scheme is demonstrated pictorially in the leading-order Feynman diagram, figure 1(d). To suppress the $t\bar{t}Z$ process, events containing b-tagged jets are rejected. To reduce the ZZ background process in 2-SFOS events, the invariant mass of ℓ_0 and ℓ_1, $m_{\ell_0\ell_1}$, is required to be below 50 GeV; to ensure orthogonality with the ATLAS $H \to ZZ^* \to 4\ell$ measurement [12], the 4-lepton invariant mass, $m_{4\ell}$, is required to be below 115 GeV or above 130 GeV. Finally, the angular separation between ℓ_0 and ℓ_1, $\Delta R_{\ell_0\ell_1}$, is required to be larger than 0.2 to remove overlapping leptons.

The selections described above constitute the 1-SFOS and 2-SFOS SRs. For each SR, a discriminant based on a BDT is used to achieve a further separation between the ZH and ZZ processes. Independent BDTs are trained for each SR but sharing a common set of input variables, which are summarised in table 18 of appendix A. In the 1-SFOS SR, the most important variables for discriminating between ZH and ZZ include $m_{\ell_0\ell_1}$, the number of jets, and the azimuthal separation between the leptons from the Higgs boson candidate in the rest frame of the Higgs boson, $\Delta\phi^{\mathrm{boost}}_{\ell_0\ell_1}$; in the 2-SFOS SR, the most important variables include $m_{\ell_0\ell_1}$, $E_{\mathrm{T}}^{\mathrm{miss}}$, and $\Delta\phi^{\mathrm{boost}}_{\ell_0\ell_1}$. Figure 5 shows the post-fit distributions of the BDT discriminants and signal-sensitive kinematic variables in the two 4ℓ SRs.

6.5 STXS categorisation

The Stage 1.2 STXS categorisation scheme for VH production is split by the production mode ($q\bar{q} \to WH$, $q\bar{q} \to ZH$, and $gg \to ZH$), the p_{T} of the associated vector boson, and the number of jets, as shown in figure 17 of appendix B. Based on the expected sensitivity of the measurement, kinematic fiducial regions are merged to ensure each cross-section is

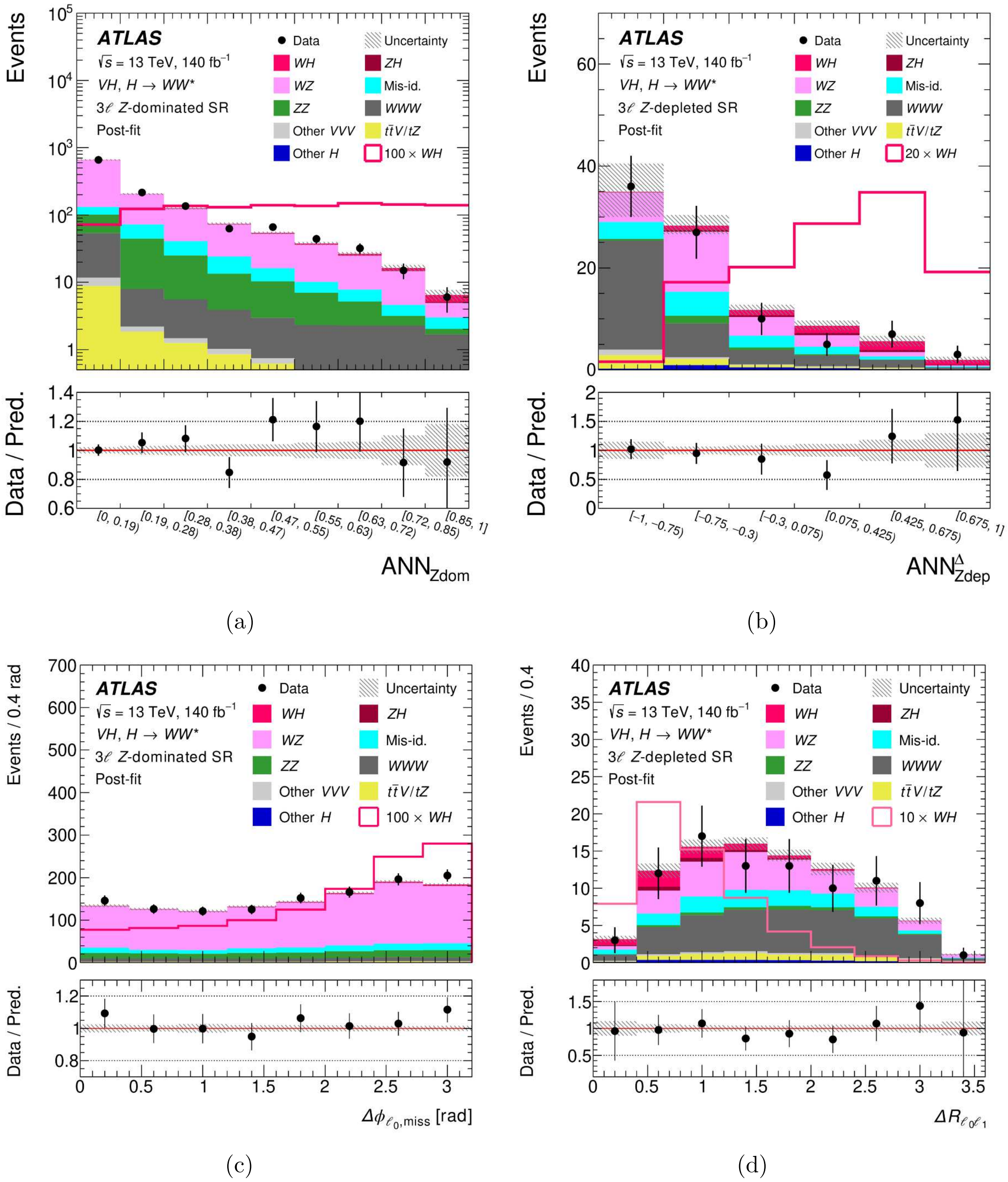

Figure 4. Post-fit distributions of (a) $\mathrm{ANN_{Zdom}}$ and (c) the azimuthal separation between lepton 0 and the $E_{\mathrm{T}}^{\mathrm{miss}}$, $\Delta\phi_{\ell_0,\mathrm{miss}}$, in the Z-dominated SR as well as (b) $\mathrm{ANN}^{\Delta}_{\mathrm{Zdep}}$ and (d) the angular distance between leptons 0 and 1, $\Delta R_{\ell_0\ell_1}$, in the Z-depleted SR. The post-fit WH signal yields are additionally overlaid and upscaled in all distributions. The lower panel shows the ratio of the data to the sum of the fitted signal and background. The last bin includes overflow, where applicable. The post-fit results are obtained from the combined 2-POI fit described in section 9.1.

JHEP08(2025)034

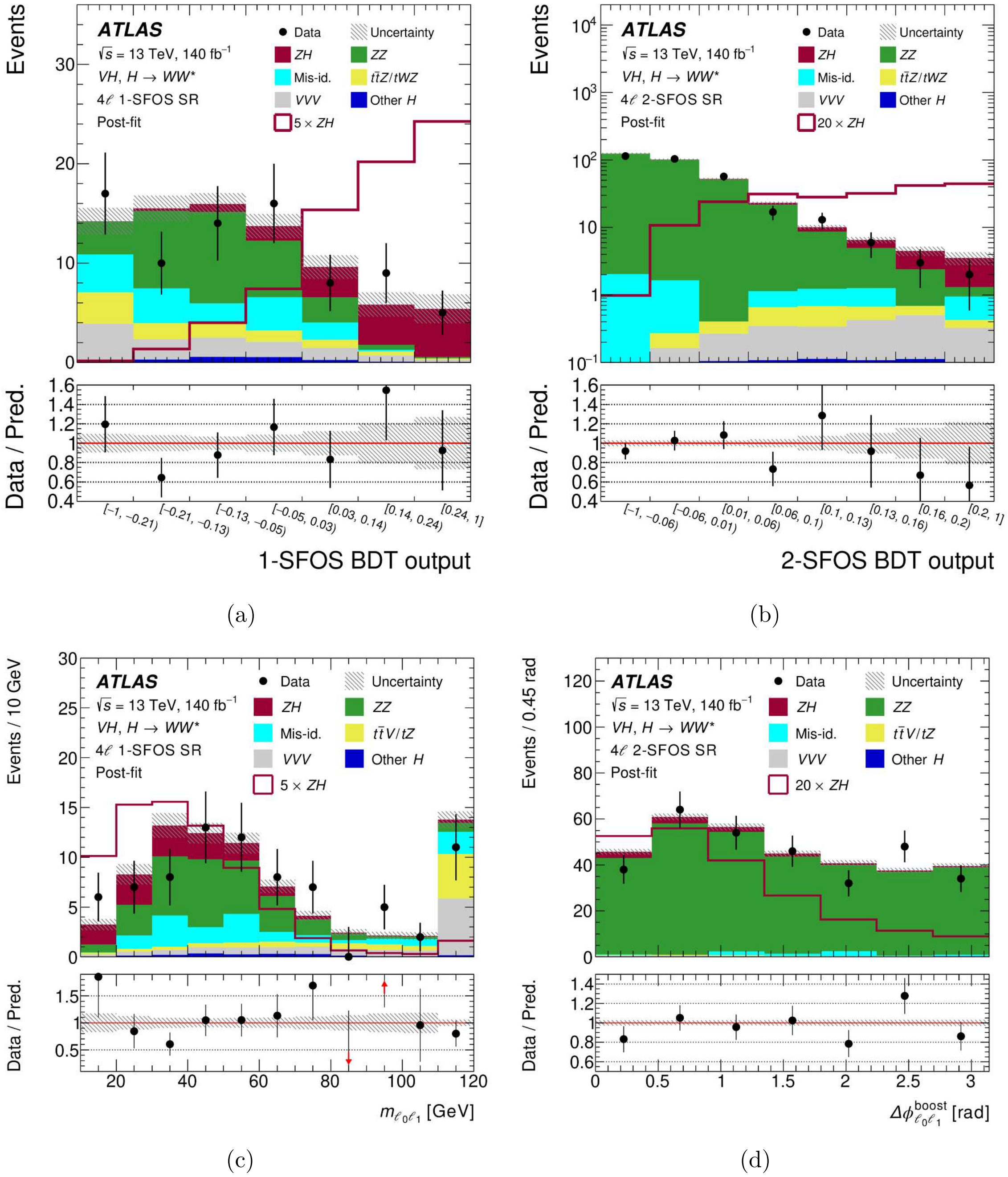

Figure 5. Post-fit distributions of (a) the BDT output and (c) the invariant mass of the Higgs boson candidate, $m_{\ell_0\ell_1}$, in the 1-SFOS SR and (b) the BDT output and (d) the azimuthal separation between the leptons from the Higgs boson candidate in the rest frame of the Higgs boson, $\Delta\phi^{\text{boost}}_{\ell_0\ell_1}$, in the 2-SFOS SR. The post-fit ZH signal yields are additionally overlaid and upscaled in all distributions. The lower panel shows the ratio of the data to the sum of the fitted signal and background, and the arrow in (c) indicates the position of a point outside the vertical axis range. The hatched band shows the total uncertainty. The last bin includes overflow, where applicable. The post-fit results are obtained from the combined 2-POI fit described in section 9.1.

JHEP08(2025)034

p_T^V scheme	STXS scheme
VH, $0 \leq p_T^V < 75\,\text{GeV}$	$\ell\nu H$ and $\ell\ell H$, $0 \leq p_T^V < 75\,\text{GeV}$
VH, $75 \leq p_T^V < 150\,\text{GeV}$	$\ell\nu H$ and $\ell\ell H$, $75 \leq p_T^V < 150\,\text{GeV}$
VH, $150 \leq p_T^V < 250\,\text{GeV}$	$\ell\nu H$ and $\ell\ell H$, $p_T^V \geq 150\,\text{GeV}$
VH, $p_T^V \geq 250\,\text{GeV}$	EW qqH, $60 \leq m_{jj} < 120\,\text{GeV}$

Table 4. Summary the differential cross-sections measured in the p_T^V and STXS schemes.

measured with adequate precision, yielding a reduced categorisation schemes, p_T^V and STXS. In both the schemes, there is no splitting of events by jet multiplicity. The fiducial regions for each are shown in table 4.

For the p_T^V scheme, the $q\bar{q} \to WH$, $q\bar{q} \to ZH$, and $gg \to ZH$ categories are merged into a single VH category which is inclusive in the decay of the vector boson and which is defined in the fiducial region $|y_H| < 2.5$ where y_H is the rapidity of the Higgs boson. The $250 \leq p_T^V < 400\,\text{GeV}$ and $p_T^V \geq 400\,\text{GeV}$ categories are merged into a single $p_T^V \geq 250\,\text{GeV}$ category. This yields four measured fiducial cross-sections.

In the STXS scheme, the $q\bar{q} \to W(\to \ell\nu)H$ category, written as $\ell\nu H$ for brevity, is measured independently of the $q\bar{q} \to Z(\to \ell\ell/\nu\nu)H$ and $gg \to Z(\to \ell\ell/\nu\nu)H$ categories, which are merged and written as $\ell\ell H$ for brevity. The $150 \leq p_T^V < 250\,\text{GeV}$, $250 \leq p_T^V < 400\,\text{GeV}$, and $p_T^V \geq 400\,\text{GeV}$ categories are merged into a single $p_T^V \geq 150\,\text{GeV}$ category. The EW qqH category with $60 \leq m_{jj} < 120\,\text{GeV}$ is measured using the opposite-sign 2ℓ channel. This yields seven measured fiducial cross-sections.

For each of the channels considered by the analysis, subregions of the corresponding SRs are defined which target the individual or pairs of the fiducial cross-sections above. The subregions are split using selections on reconstructed proxies of p_T^V; the boundaries of these selections were scanned and chosen to ensure adequate expected sensitivity for all POIs measured by the corresponding channel. Table 5 summarises the p_T^V proxies and selections for each channel and the relevant p_T^V range for each subregion.

For the opposite-sign 2ℓ channel, the chosen proxy is the dijet transverse momentum, p_T^{jj}. For the same-sign 2ℓ channel, the chosen proxy is the scalar sum of the lepton, jet, and missing transverse momenta, $\sum |p_T|$. The same splitting is shared between the SS2μ, SS$2e$, and SSDF SRs.

For the 3ℓ channel, a regression ANN is used to reconstruct the transverse momentum of the W boson. The regression ANN receives a subset of the input variables used by the multi-classifier of the Z-depleted SR — these input variables are summarised in table 19 of appendix A. Its output node, p_T^R, is chosen as a proxy for p_T^V and is utilised in both the Z-dominated and Z-depleted SRs.

For the 4ℓ channel, the chosen proxy is the transverse momentum of the Z boson candidate, $p_T^Z \coloneqq p_T^{\ell_2\ell_3}$. The same splitting is applied to both the 1-SFOS and 2-SFOS SRs.

The performance of the proxies for several channels is shown in figure 18 of appendix B. Each channel uses the trained multivariate discriminant from the inclusive SR in each of its subregions; retraining of the discriminant was tested for the 3ℓ channel without producing

Channel	p_{T}^{V} proxy	Reconstructed SR	Relevant p_{T}^{V} range
Opposite-sign 2ℓ	Dijet transverse momentum, p_{T}^{jj}	$0 \leq p_{\mathrm{T}}^{jj} < 160\,\mathrm{GeV}$	$0 \leq p_{\mathrm{T}}^{V} < 150\,\mathrm{GeV}$
		$160 \leq p_{\mathrm{T}}^{jj} < 260\,\mathrm{GeV}$	$150 \leq p_{\mathrm{T}}^{V} < 250\,\mathrm{GeV}$
		$p_{\mathrm{T}}^{jj} \geq 260\,\mathrm{GeV}$	$p_{\mathrm{T}}^{V} \geq 250\,\mathrm{GeV}$
Same-sign 2ℓ	Scalar sum of lepton, jet, and missing transverse momenta, $\sum \lvert p_{\mathrm{T}} \rvert$	$0 \leq \sum \lvert p_{\mathrm{T}} \rvert < 200\,\mathrm{GeV}$	$0 \leq p_{\mathrm{T}}^{V} < 75\,\mathrm{GeV}$
		$200 \leq \sum \lvert p_{\mathrm{T}} \rvert < 320\,\mathrm{GeV}$	$75 \leq p_{\mathrm{T}}^{V} < 150\,\mathrm{GeV}$
		$320 \leq \sum \lvert p_{\mathrm{T}} \rvert < 460\,\mathrm{GeV}$	$150 \leq p_{\mathrm{T}}^{V} < 250\,\mathrm{GeV}$
		$\sum \lvert p_{\mathrm{T}} \rvert \geq 460\,\mathrm{GeV}$	$p_{\mathrm{T}}^{V} \geq 250\,\mathrm{GeV}$
3ℓ Z-dominated	Regression ANN for W transverse momentum, p_{T}^{R}	$0 \leq p_{\mathrm{T}}^{R} < 90\,\mathrm{GeV}$	$0 \leq p_{\mathrm{T}}^{V} < 75\,\mathrm{GeV}$
		$90 \leq p_{\mathrm{T}}^{R} < 180\,\mathrm{GeV}$	$75 \leq p_{\mathrm{T}}^{V} < 150\,\mathrm{GeV}$
		$p_{\mathrm{T}}^{R} \geq 180\,\mathrm{GeV}$	$p_{\mathrm{T}}^{V} \geq 150\,\mathrm{GeV}$
3ℓ Z-depleted	Regression ANN for W transverse momentum, p_{T}^{R}	$0 \leq p_{\mathrm{T}}^{R} < 90\,\mathrm{GeV}$	$0 \leq p_{\mathrm{T}}^{V} < 75\,\mathrm{GeV}$
		$90 \leq p_{\mathrm{T}}^{R} < 180\,\mathrm{GeV}$	$75 \leq p_{\mathrm{T}}^{V} < 150\,\mathrm{GeV}$
		$180 \leq p_{\mathrm{T}}^{R} < 270\,\mathrm{GeV}$	$150 \leq p_{\mathrm{T}}^{V} < 250\,\mathrm{GeV}$
		$p_{\mathrm{T}}^{R} \geq 270\,\mathrm{GeV}$	$p_{\mathrm{T}}^{V} \geq 250\,\mathrm{GeV}$
4ℓ	Z boson transverse momentum, p_{T}^{Z}	$0 \leq p_{\mathrm{T}}^{Z} < 75\,\mathrm{GeV}$	$0 \leq p_{\mathrm{T}}^{V} < 75\,\mathrm{GeV}$
		$75 \leq p_{\mathrm{T}}^{Z} < 150\,\mathrm{GeV}$	$75 \leq p_{\mathrm{T}}^{V} < 150\,\mathrm{GeV}$
		$150 \leq p_{\mathrm{T}}^{Z} < 250\,\mathrm{GeV}$	$150 \leq p_{\mathrm{T}}^{V} < 250\,\mathrm{GeV}$
		$p_{\mathrm{T}}^{Z} \geq 250\,\mathrm{GeV}$	$p_{\mathrm{T}}^{V} \geq 250\,\mathrm{GeV}$

Table 5. Selections used to define the SRs entering the differential cross-section measurement. For each channel, the p_{T}^{V} proxy and the selections applied to it are shown. In the context of the Stage 1.2 STXS framework, the p_{T}^{V} range relevant to each SR is also shown. In the case of the same-sign 2ℓ channel, the selections are the same for each of the SS2μ, SS$2e$, and SSDF SRs; in the case of the 4ℓ channel, the selections are the same for each of the 1-SFOS and 2-SFOS SRs.

appreciable improvements in sensitivity. The binning of the discriminant in each subregion is necessarily different from that of the inclusive SR, owing to smaller sample sizes. These distributions are provided as input to the combined fit. In the case of the STXS scheme, the opposite-sign 2ℓ SR is still split according to p_{T}^{V}; however, only a single fiducial cross-section of EW qqH is measured.

Figure 6 shows the relative contributions of the reduced categories in all reconstructed SRs. In each case, the reduced categories provide the largest contributions in the corresponding SRs which aim to select them. Post-fit distributions for a subset of the SRs are shown in figures 7 and 8 for the $2\ell/3\ell$ and 4ℓ channels, respectively.

7 Background modelling

The background contamination in the SRs results from various physics processes, each modelled by pure data-driven prediction, pure MC prediction, or MC prediction normalised to data either using dedicated CRs or using only the SRs. The first method — pure data-driven

JHEP08(2025)034

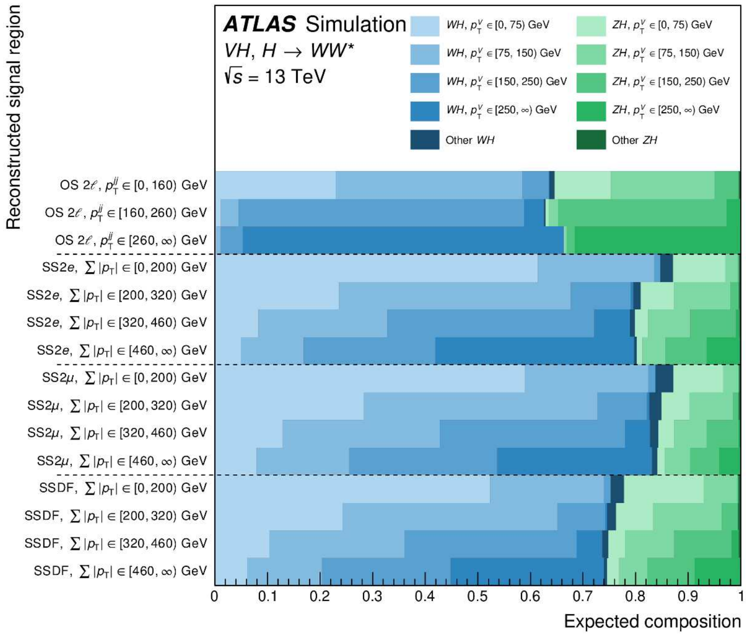

(a)

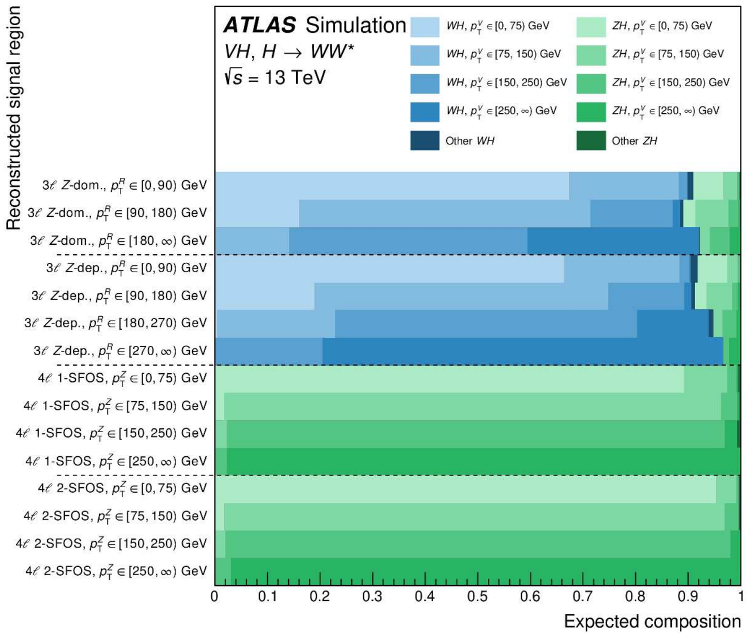

(b)

Figure 6. Relative SM signal composition in terms of the reduced categories for each reconstructed SR of the (a) 2ℓ and (b) $3\ell/4\ell$ channels. The categorisation follows the p_T^V scheme; however, the WH and ZH templates are resolved to show their relative fraction in each SR. "Other WH/ZH" includes forward Higgs bosons (i.e., Higgs bosons produced with rapidity $|y| > 2.5$) and — for the 3ℓ channels only — Higgs boson processes not included in the categorisation.

JHEP08(2025)034

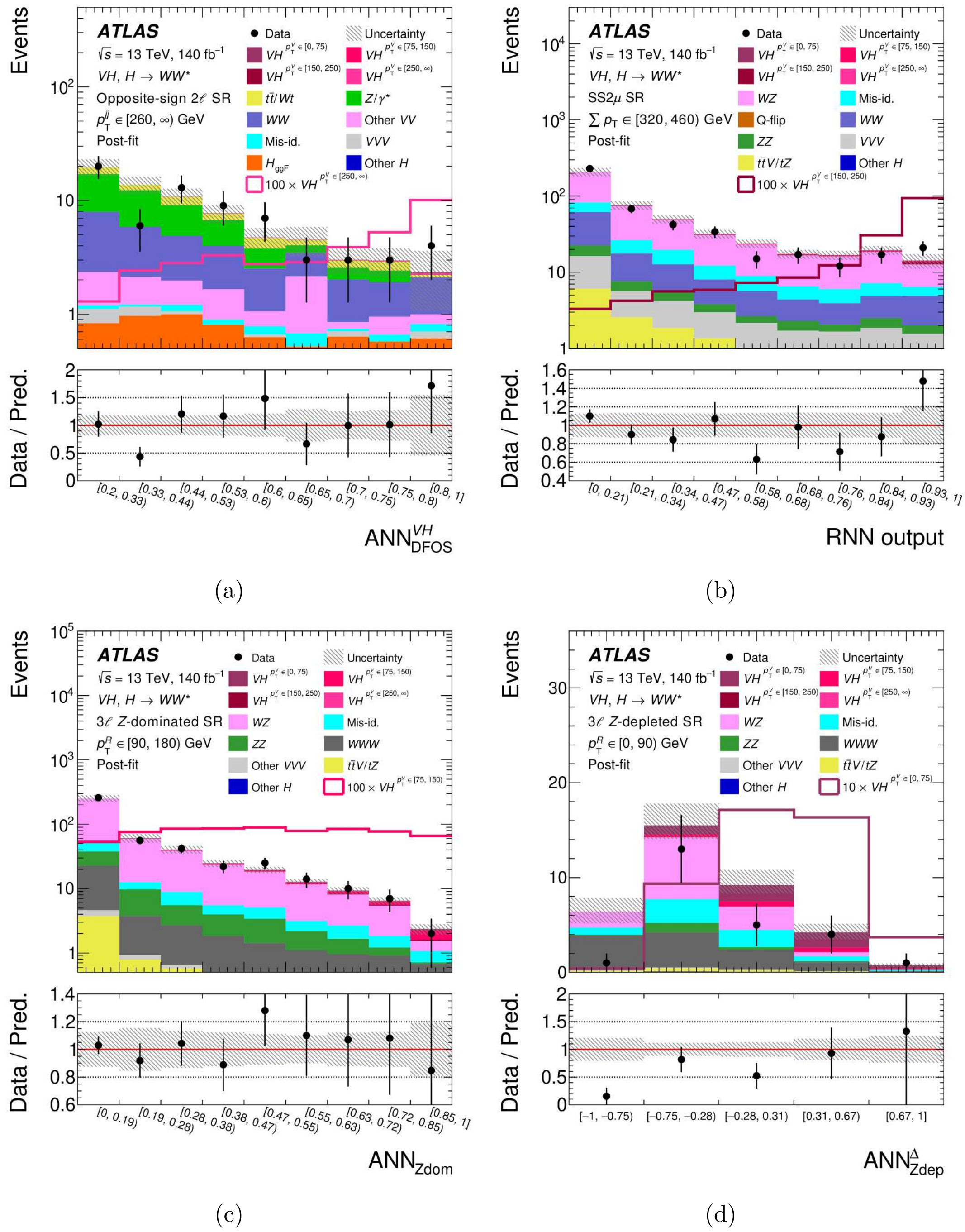

Figure 7. Post-fit ANN/RNN discriminants in a subset of the SRs considered by the analysis: (a) opposite-sign 2ℓ SR in the $p_{\mathrm{T}}^{jj} \geq 260\,\mathrm{GeV}$ subregion, (b) SS2μ SR in the $230 \leq \sum |p_{\mathrm{T}}| < 460\,\mathrm{GeV}$ subregion, (c) 3ℓ Z-dominated SR in the $90 \leq p_{\mathrm{T}}^{R} < 180\,\mathrm{GeV}$ subregion, and (d) 3ℓ Z-depleted SR in the $0 \leq p_{\mathrm{T}}^{R} < 90\,\mathrm{GeV}$ subregion. The lower panel shows the ratio of the data to the sum of the fitted signal and background. In each distribution, the post-fit VH signal template targeted by that SR is overlaid and upscaled. The hatched band shows the total uncertainty. The post-fit results are obtained from the combined fit for the p_{T}^{V} scheme, described in section 9.1.

JHEP08(2025)034

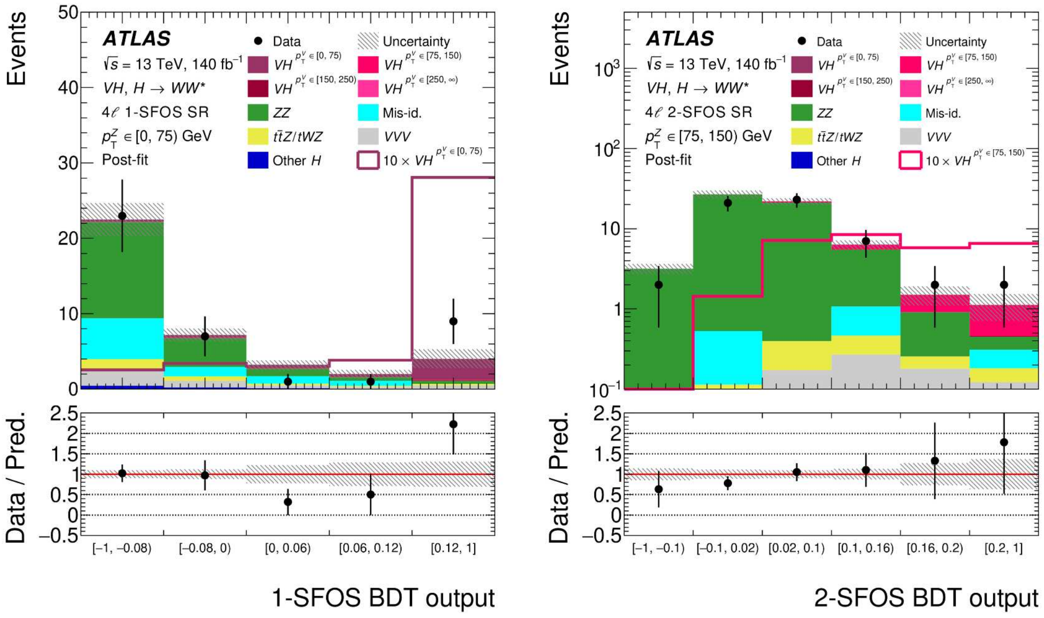

(a) (b)

Figure 8. Post-fit BDT discriminants in a subset of the SRs considered by the analysis: (a) 4ℓ 1-SFOS SR in the $0 \leq p_T^Z < 75\,\text{GeV}$ subregion and (b) 4ℓ 2-SFOS SR in the $75 \leq p_T^Z < 150\,\text{GeV}$ subregion. In each distribution, the post-fit VH signal template targeted by that SR is overlaid and upscaled. The lower panel shows the ratio of the data to the sum of the fitted signal and background. The hatched band shows the total uncertainty. The post-fit results are obtained from the combined fit for the p_T^V scheme, described in section 9.1.

Channel	Pure MC	Normalised in the fit	Control region	Data-driven
Opposite-sign 2ℓ	WZ, ZZ, VVV, H (non-VH)	—	$t\bar{t}/Wt$, Z+jets, WW	$W+\gamma$, W+jets
Same-sign 2ℓ	WW, ZZ, VVV, $t\bar{t}V/tZ$	WZ	—	$V+\gamma$, V+jets
3ℓ	ZZ, VVV (non-WWW), $t\bar{t}V/tZ$, H (non-VH)	WWW	WZ	$Z+\gamma$, Z+jets, $t\bar{t}/Wt$, WW
4ℓ	VVV, $t\bar{t}V/tWZ$, H (non-VH)	—	ZZ	WZ, $t\bar{t}W/tZ$, Z+jets, $t\bar{t}/Wt$

Table 6. Summary of background modelling for each channel. "Normalised in the fit" are the background processes which are normalised in the fit but which do not have dedicated control regions; instead, their normalisation is determined by the signal discriminant. Data-driven background processes have at least one reconstructed mis-identified lepton.

prediction — is used to estimate the backgrounds with mis-identified leptons and electrons with mis-identified charge. In this estimate, rates and differential distributions ("shapes") are extracted from data exploiting the method described in section 7.1. In the second method, the rates and shapes are extracted from simulation and normalised to the predicted cross-sections. In the third method, the rates are fit to data using the CRs — which are orthogonal to the SRs — in addition to the SRs themselves, while the shapes are extracted from simulation. Table 6 summarises the method adopted for each background process in each signal region. The same methods are adopted for the STXS measurement with no change of the CR definitions.

JHEP08(2025)034

In the opposite-sign 2ℓ channel, different CRs are defined to normalise the top, Z+jets, and WW background processes. The VH output node of the ANN is required to be less than 0.2 to define a region orthogonal to the SR, while dedicated selections on each of the ANN background nodes — $\mathrm{ANN}^{\mathrm{top}}_{\mathrm{DFOS}}$, $\mathrm{ANN}^{Z+\mathrm{jets}}_{\mathrm{DFOS}}$, and $\mathrm{ANN}^{WW}_{\mathrm{DFOS}}$ — are used to define three CRs. The top CR is used to normalise both the $t\bar{t}$ and Wt background processes. The purities for the top, Z+jets, and WW CRs are 72%, 77%, and 58%, respectively. In this section, a CR purity is defined as the number of events targeted by that CR relative to the total number of events, each calculated within that CR.

In the same-sign 2ℓ channel, the WZ background in the SR is normalised using a free fit parameter. The $t\bar{t}$ and Z+jets background processes contribute when the charge of one lepton is wrongly assigned. An electron with a hard bremsstrahlung or a mis-measured track curvature has a large charge mis-identification probability, which is measured in data using a control sample of electrons from Z boson decays. In this sample, the WZ background is obtained from MC and the mis-identified lepton background is obtained from the data-driven procedure described in section 7.1. The charge mis-identification probability is parametrised as a function of electron p_{T} with six bins and $|\eta|$ with six bins. The bins were chosen in accordance with the size of the event sample and the geometry of the detector. The charge mis-identification probability varies from $\mathcal{O}(10^{-5})$ for the electrons with $15 < p_{\mathrm{T}} < 60\,\mathrm{GeV}$ and $|\eta| < 0.6$ to $\mathcal{O}(10^{-1})$ for electrons with $p_{\mathrm{T}} > 300\,\mathrm{GeV}$ and $|\eta| > 2.3$. The measured charge mis-identification probabilities are applied to a sample of opposite-sign leptons that satisfies the requirements of same-sign 2ℓ SRs, resulting in an estimate of the charge mis-identification background in each SR. The fraction of the charge mis-identification background is 26% in the SS2e SR and 1.6% in the SSDF SR. The muon charge mis-identification probability is negligible in the p_{T} range relevant to this analysis.

The quality of the WZ modelling of the RNN for the same-sign 2ℓ channel was evaluated in a WZ-enriched validation region, defined using the selections common to each of the SS2μ, SS2e, and SSDF SRs but inclusive in the flavours of the leading isolated leptons. This validation region also requires an additional reconstructed lepton with $p_{\mathrm{T}} > 15\,\mathrm{GeV}$ and meeting looser quality criteria than those applied to the two leading isolated leptons. These looser leptons are reconstructed imperfectly and are similar to those missed in WZ events in which only two leptons are reconstructed. As a consequence, the RNN distribution in this region is sensitive to the quality of simulating events with real leptons from WZ. This validation region is also depleted in signal, with relative signal fractions of $< 1\%$ inclusively and $< 2\%$ in the signal-sensitive bin. A shape mis-modelling of the RNN shape for WZ events is observed, amounting to 30% less data than predicted in the bins of higher value of the RNN output. The source of this mis-modelling was found to be particularly enhanced at small values of the ΔR distribution between a lepton and its nearest jet as well as at small values of the distribution of the minimum lepton-jet invariant mass considering all leptons and jets. As the signal events tend to be at low values of this variable, the high-score regions of the RNN also exhibit this mis-modelling. A dedicated correction to the RNN shape in the WZ background is derived by fitting an exponential function to the ratio of data — with the non-WZ background subtracted — to the WZ background. The correction is then applied to the WZ background in each of the SS2μ, SS2e, and SSDF signal regions,

JHEP08(2025)034

with a conservative 100% systematic uncertainty assigned to the correction and decorrelated among the signal regions. This uncertainty reduces the expected sensitivity of the same-sign 2ℓ channel by $\sim$20% with respect to what is obtained neglecting it. Good modelling is observed for events with three reconstructed leptons that are required to meet stringent quality criteria — as shown in figure 10. Consequently, no additional correction or uncertainty is needed for the 3ℓ channels.

In the 3ℓ channel, WZ CRs are defined by requiring at least one SFOS lepton pair and by inverting the Z-veto selection with respect to the Z-dominated SR. The WZ background normalisation depends on the jet multiplicity of the events, so the CR is split into two regions containing events with no reconstructed jets and events with at least one reconstructed jet, respectively. The purity of the regions without jets is 93% and the purity of the region with one or more jets is 88%.

Motivated by an excess in the measurement of the $WWW+WH$ rate reported in ref. [136], the WWW background is normalised in the fit procedure through a floating parameter and without a dedicated CR. The WWW process is the largest background in the 3ℓ Z-depleted channel followed by WZ production, and thus the value of the WWW normalisation factor is entirely determined by this channel. The measured normalisation factor, $2.2^{+0.7}_{-0.6}$, is consistent with the measured signal strength, 1.61 ± 0.25, from the ATLAS WWW analysis [136].

In the 4ℓ channel, a dedicated CR is used to estimate the normalisation factor of the ZZ process. It is defined in the 2-SFOS channel after the b-jet veto by adding a set of requirements on the invariant mass of each of the lepton pairs. To select on-shell Z boson leptonic decays, $m_{\ell_2\ell_3}$ is required to be within ± 10 GeV of the Z boson mass. The invariant mass $m_{\ell_0\ell_1}$ must be above 50 GeV. The purity of this region is about 97%.

Figures 9, 10, and 11 show distributions of the multivariate discriminants, described in section 6, in the relevant CRs. Good modelling is observed in the CRs for all of the distributions shown.

The background processes which are not normalised in the fit procedure or not measured via data-driven methods are estimated via pure MC prediction and normalised to their theoretical cross-sections.

7.1 Backgrounds with non-prompt leptons

Non-prompt electrons can originate from the decays of heavy-flavour hadrons, mis-identification of hadronic jets, and photon conversions in the detector material, with an admixture depending on the lepton quality requirements and event categories. Non-prompt muons only originate from decays of heavy-flavour hadrons. The physical processes which contribute non-prompt leptons in each channel are summarised in table 6.

All backgrounds with non-prompt leptons are estimated by weighting events from dedicated control samples with extrapolation factors. Except for requiring one of the lepton candidates to be an anti-identified ("anti-ID") lepton, these control samples satisfy all of the nominal selections given in table 2. An anti-ID lepton fails to meet the full identification criteria used to select identified ("ID") leptons but satisfies a looser set of criteria. The extrapolation factors are defined as the ratios between the numbers of events with non-prompt lepton candidates being ID and anti-ID. Using the control samples, a maximum-likelihood fit

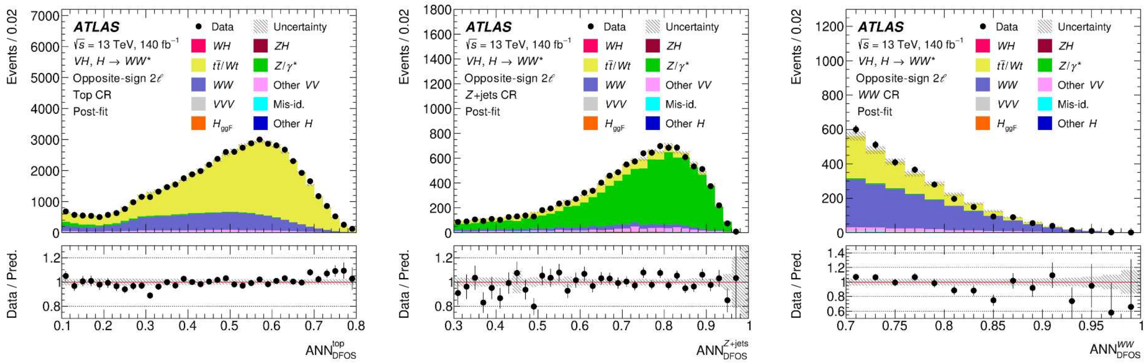

(a) (b) (c)

Figure 9. Post-fit distributions of (a) $\text{ANN}^{\text{top}}_{\text{DFOS}}$ in the top CR, (b) $\text{ANN}^{Z\text{+jets}}_{\text{DFOS}}$ in the Z+jets CR, and (c) $\text{ANN}^{WW}_{\text{DFOS}}$ in the WW CR of the opposite-sign 2ℓ channel. The lower panel shows the ratio of the data to the sum of the fitted signal and background. The hatched band shows the total uncertainty. The last bin includes overflow, where applicable. The post-fit results are obtained from the combined 2-POI fit described in section 9.1.

measures the extrapolation factors such that the total number of weighted events matches the number of observed data events with only ID leptons after subtracting the expected contribution from processes with only prompt leptons.

The non-prompt electron background in 2ℓ and 3ℓ channels is estimated from simulation with data-driven corrections. The corresponding extrapolation factors are measured separately for three sources — heavy-flavour jets, light-flavour jets, and γ conversions — using three sets of samples enriched in $t\bar{t}$, Z+jets, and $Z+\gamma$ events, respectively. The simulated events with a non-prompt anti-ID electron are counted according to the source of the non-prompt electron and weighted by extrapolation factors. This yields three sets of extrapolation factors which are simultaneously measured using a maximum-likelihood fit. In contrast, the non-prompt muon background in 2ℓ and 3ℓ channels is estimated by using a fully data-driven technique. From a sample enriched in $t\bar{t}$, the number of events with a non-prompt muon is calculated from the observed data after subtracting the expected contribution from processes with only prompt muons. The corresponding extrapolation factors are then obtained from a maximum-likelihood fit. The non-prompt electron and muon extrapolation factors are both measured in bins of lepton p_{T}.

The measurement of the non-prompt electron and muon extrapolation factors for the 4ℓ channel follows a similar procedure to the measurement of the non-prompt muon extrapolation factors for the 2ℓ and 3ℓ channels. The differences between the 2ℓ and 3ℓ channels are due to the looser lepton selection and the lower sample size available in the control samples. The extrapolation factors are measured in a sample enriched in Z+jets events and are inclusive in lepton p_{T}. Processes with two non-prompt leptons are accounted for in the extrapolation by applying a correction term evaluated in a sample where two of the lepton candidates are anti-ID.

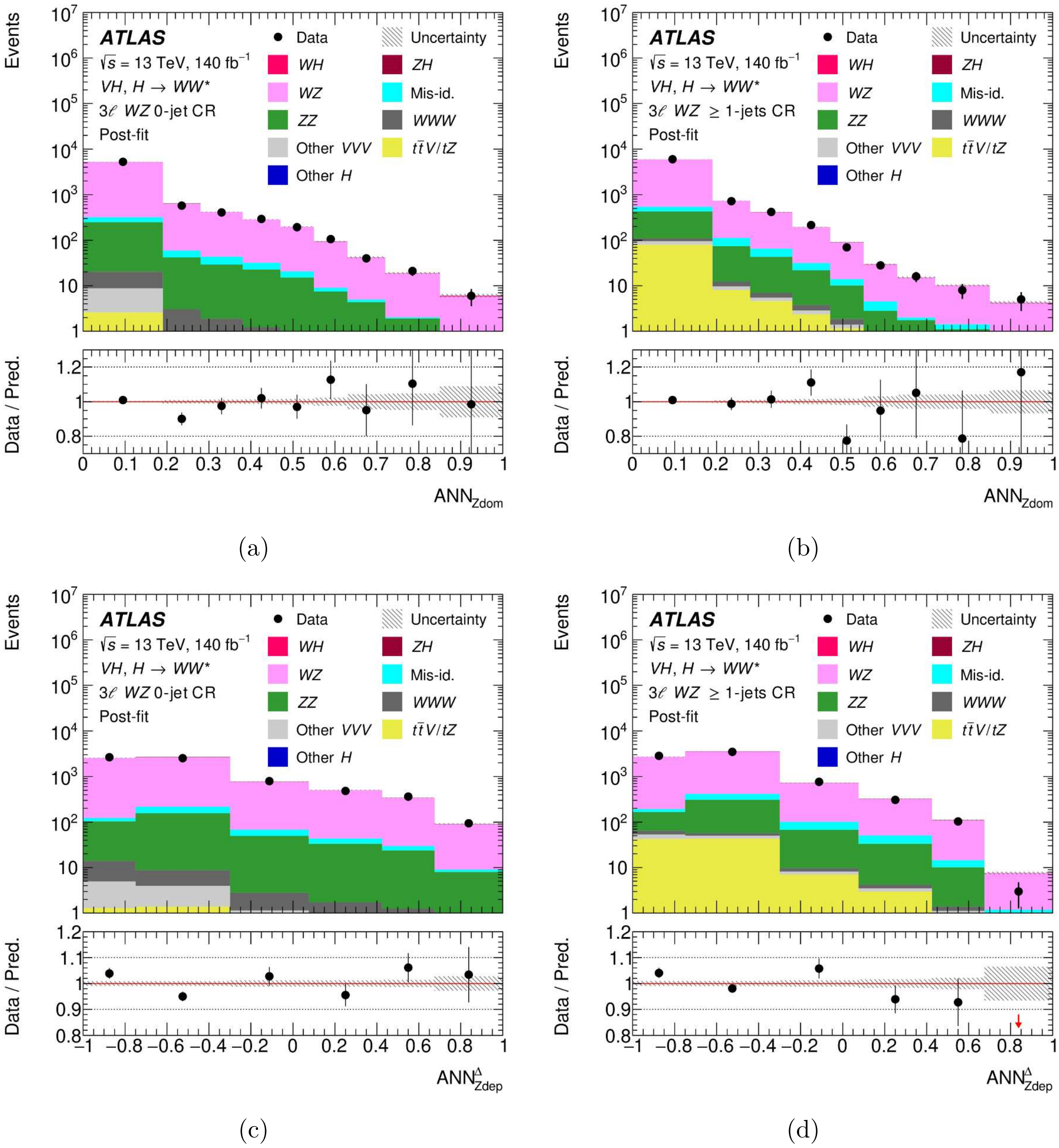

Figure 10. Post-fit distributions of $\mathrm{ANN}_{\mathrm{Zdom}}$ in the (a) WZ CR with no jets and (b) WZ CR with at least one jet and of $\mathrm{ANN}^{\Delta}_{\mathrm{Zdep}}$ in the (c) WZ CR with no jets and (d) WZ CR with at least one jet. The binning of each distribution matches that used in the corresponding SR where that distribution is relevant. The lower panel shows the ratio of the data to the sum of the fitted signal and background, and the arrow in (d) indicates the position of a point outside the vertical axis range. The hatched band shows the total uncertainty. The post-fit results are obtained from the combined 2-POI fit described in section 9.1.

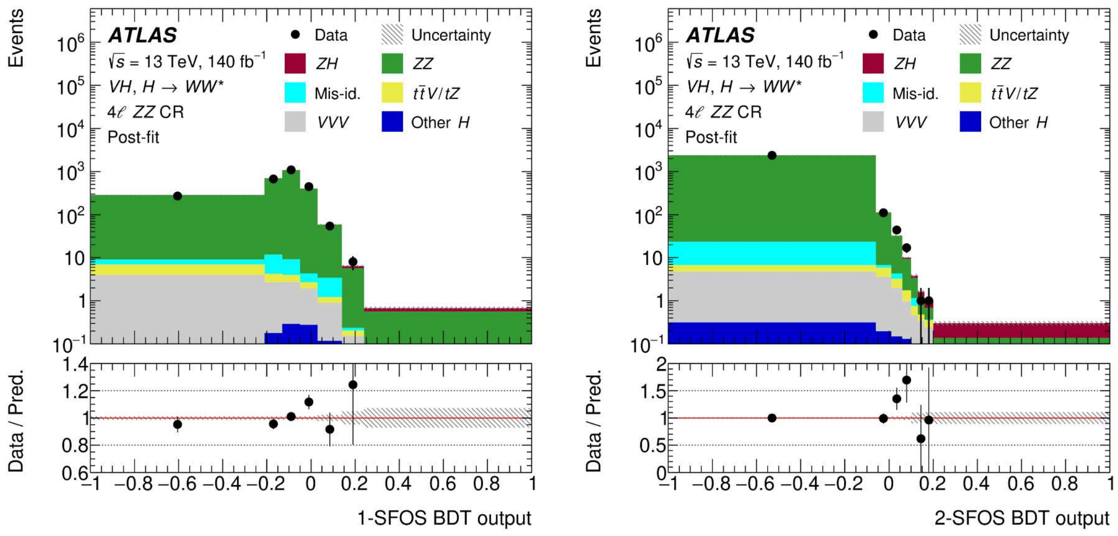

(a) (b)

Figure 11. Post-fit distributions of the (a) 1-SFOS BDT output and (b) 2-SFOS BDT output in the ZZ CR. The binning of each distribution matches that used in the corresponding SR where that distribution is relevant. The lower panel shows the ratio of the data to the sum of the fitted signal and background. The hatched band shows the total uncertainty. The post-fit results are obtained from the combined 2-POI fit described in section 9.1.

8 Systematic uncertainties

The experimental and theoretical sources of systematic uncertainties are evaluated using MC samples and their effects are included in the statistical analysis. The impact of each uncertainty is estimated per analysis region and per bin. A list of the systematic uncertainty sources with corresponding impact on the measurement is shown in section 9.2.

The theoretical and experimental uncertainties are varied in a correlated way for all MC processes across all signal and control region bins, which considers the normalisation extrapolation from control to signal regions.

8.1 Experimental uncertainties

Experimental uncertainties associated with leptons originate from the reconstruction, identification, and isolation efficiencies [120, 121] and from the scale and resolution of the energy or momentum [137, 138]. For jets, uncertainties arise from the jet energy scale and resolution [126], the performance of the pile-up jet tagger [127, 129], and the b-jet identification [131]. Furthermore, uncertainties due to the trigger selection [117, 118] and the soft term in the reconstruction of the $E_{\mathrm{T}}^{\mathrm{miss}}$ [132] are estimated. The uncertainty in the modelling of pile-up for simulated samples is estimated by varying the reweighting to the profile in data within its uncertainties. The uncertainty in the integrated luminosity is 0.83% [30], which is measured using the LUCID-2 detector [139]. The luminosity uncertainty is applied to the signal and background processes which are normalised to theoretical predictions.

JHEP08(2025)034

For the data-driven estimate of the backgrounds attributed to mis-identified leptons and electrons with mis-identified charge, uncertainties are considered for the availability of data and MC statistics, variations on the theoretical predictions of the prompt lepton backgrounds, variations in the analysis selections, and the self-consistency of the method. The latter source of uncertainty is estimated purely using MC by comparing the mis-identified lepton estimate obtained from MC to that obtained by applying the data-driven method to the MC sample, using extrapolation factors evaluated from MC.

The largest sources of experimental uncertainties are the following: jet energy scale uncertainties (9.2%)[4] for the opposite-sign 2ℓ channel; uncertainties relating to the RNN shape correction for WZ (200%), the estimate of the mis-identified lepton background (150%), and the estimate of the electron background with mis-identified charge (56%) for the same-sign 2ℓ channel; and uncertainties relating to the estimate of the mis-identified lepton background (11% and 2.9%) and the isolation of leptons (3.0% and 3.9%) for the 3ℓ and 4ℓ channels.

8.2 Theoretical uncertainties

The impact of the theoretical sources of uncertainty is evaluated by reweighting MC events or by using alternative MC samples, which are detailed in table 1. Uncertainties computed as differences between two samples are symmetrised. Uncertainties in background processes with negligible contributions in the signal regions are not considered. All uncertainties are computed using detector-level events unless specified otherwise.

For all processes, the uncertainty in missing higher-order corrections is computed as the maximum variation of the envelope resulting from simultaneous variations of the renormalisation and factorisation scales by factors of 0.5 and 2. The uncertainty in the central value of the PDF set is evaluated by comparing the nominal weight to alternative weights, the latter encapsulating the experimental and model-related uncertainties entering the PDF fit. The uncertainty in the central value of the strong coupling constant, $\alpha_s = 0.1180 \pm 0.0015$, is evaluated by varying it up and down by its uncertainty and recalculating the event weight for each case. The midpoint between these varied weights is symmetrised and assigned as the corresponding uncertainty in the nominal weight.

The uncertainty in the PS modelling for the Higgs boson processes is assigned as the difference between the nominal sample showered with PYTHIA 8 and an alternative sample showered with HERWIG 7. For the VH signal process, this uncertainty is computed using particle-level events with selections similar to those on detector-level and the same multivariate discriminants.

The merging of the NLO and LO matrix elements for the VV processes, which are modelled by SHERPA 2.2.2, is performed using the MEPS@NLO prescription [90]. A jet merging uncertainty (“CKKW”) is assigned by varying the nominal threshold (20 GeV) separating the ME and the PS up (30 GeV) and down (15 GeV). Similarly, a PS resummation uncertainty (“QSF”) is assigned by varying the resummation scale up and down by factors of

[4]The numbers quoted for the respective channels here and at the end of section 8.2 correspond to the average relative contribution of that source of uncertainty to the total uncertainty on the $VH/WH/ZH$ cross-section times the $H \to WW^*$ branching ratio as measured individually by that channel.

JHEP08(2025)034

2 and 0.5, respectively. The uncertainty due to the choice of the PS momentum recoil scheme ("CSSKIN") is computed by comparing the nominal sample, which uses the recoil scheme described in ref. [86], to an alternative sample, which uses the recoil scheme described in ref. [140]. In a manner analogous to the PS modelling uncertainty in VH, the CKKW, QSF, and CSSKIN uncertainties in VV are all computed using particle-level events.

The uncertainty in the ME and PS modelling for the VVV and Z+jets processes are assigned as the difference between the nominal SHERPA samples and alternative samples generated with MADGRAPH5_AMC@NLO and showered with PYTHIA 8.

The uncertainty in the hadronisation and fragmentation modelling for the $t\bar{t}$ sample is assigned as the difference between the nominal sample showered with PYTHIA 8 and an alternative sample showered with HERWIG 7. The uncertainty in the choice of generator and matching algorithm is assigned as the difference between the nominal sample generated with POWHEG and an alternative sample generated with MADGRAPH5_AMC@NLO. Uncertainties in the modelling of initial- and final-state radiation are assigned by varying scale, resummation, and showering parameters.

In the total cross-section measurement, signal modelling uncertainties are computed separately for the WH and ZH processes and decorrelated in the fit. The MC weights are varied using the inclusive samples and the uncertainties are computed in each signal and control region. In the differential cross-section measurement, signal modelling uncertainties are computed for each fiducial bin of the corresponding scheme, using the binning defined in the STXS Stage 1.2 convention and without applying any merging. For the missing higher-order QCD corrections to $V(\to \ell\nu/\ell\ell)H$, the uncertainty model described in ref. [141] is used, resulting in a set of uncertainties in the total cross-section correlated across fiducial bins and a set of migration uncertainties across the fiducial bin boundaries. Seven independent QCD uncertainty components are considered. One component affects the total production cross-section, while the other six are pure migration uncertainties. Four of these components are designed to model uncertainties across p_{T}^{V} boundaries (75, 150, 250, and 400 GeV) while the other two affect jet bin migrations across the $n_{\mathrm{jets}} = 1$ and 2 boundaries. A similar set of uncertainties are considered for $V(\to q\bar{q})H$: one affecting the total production cross-section and nine migration uncertainties relating to the fiducial selection criteria on the transverse momentum of the Higgs boson, the transverse momentum of the Higgs boson and leading dijet system, the invariant mass of the leading dijet system, and the number of jets. The uncertainties affect both the analysis acceptance, defined as the fraction of events in a fiducial region passing the analysis selection, and the predicted cross-section per fiducial region.

The largest sources of theoretical uncertainties are the following: uncertainties in the hadronisation/fragmentation modelling of $t\bar{t}$ production (19%) and on the ME/PS modelling of Z+jets production (17%) for the opposite-sign 2ℓ channel; uncertainties in the choice of PS recoil scheme for WZ production (99%) for the same-sign 2ℓ channel; uncertainties in the choice of PS recoil scheme for WZ production (9.7%) and on the ME/PS modelling of WWW production (9.4%) for the 3ℓ channel; and uncertainties in the choice of PS algorithm for ZH production (2.1%) for the 4ℓ channel.

JHEP08(2025)034

9 Fit procedure and results

9.1 Fit procedure

A binned likelihood function is constructed as a product of Poisson probability terms over the bins of the different SRs defined in section 6. The binned likelihood function is parameterised in terms of a signal strength, μ, defined as the ratio of the observed signal yield to that predicted by the SM. The signal strength constitutes the POI of the measurement. Additionally, a Poisson probability term is added for each CR and used to fit the normalisation of its corresponding background process in the combined measurement via a floating normalisation factor. Systematic uncertainties enter as nuisance parameters in the likelihood function — primarily in the form of Gaussian distributed constraints — and their correlations are taken into account. The final results are obtained using the profile likelihood method [142].

For the measurement of WH and ZH production, two fit scenarios are considered: a combined 1-POI fit, where the WH and ZH yields are simultaneously scaled by a single POI, μ_{VH}, and a combined 2-POI fit, where the WH and ZH yields are independently scaled by two POIs, μ_{WH} and μ_{ZH}, respectively. Table 7 summarises the regions entering the combined fits. In the case of the combined 1-POI fit, the SM expectation is assumed for the cross-section ratio of the WH and ZH production processes; for both combined fits, the cross-sections for non-VH Higgs boson processes are fixed to their SM expectations.

A similar prescription is followed for the differential measurements, where the SRs in table 7 are split according to table 5 and the four (p_{T}^{V} scheme) or seven (STXS scheme) fiducial cross-sections of interest are independently scaled by an equal number of POIs.

For both the total and differential cross-section measurements, the pure normalisation components of the signal theory uncertainties are factorised from the pure acceptance components — only the latter components enter the cross-section fits. Thus, the effect of theoretical uncertainties on the VH signal in a cross-section measurement should always be as small or smaller that in the corresponding signal strength measurement. For the cross-section measurement, the POIs are written as cross-sections times the $H \to WW^*$ branching ratio, $\sigma \times \mathcal{B}_{H\to WW^*}$, or those same quantities relative their SM expectations, $(\sigma \times \mathcal{B}_{H\to WW^*})/(\sigma \times \mathcal{B}_{H\to WW^*})_{\mathrm{SM}}$, to differentiate them from the POIs of the signal strength measurements, μ.

9.2 Results

9.2.1 Total cross-section results

The post-fit MC and data yields in each SR are shown in table 8. The observed data yields agree, in both the rate and shape, within uncertainties with the expected yields from MC in all SRs.

Table 9 shows the expected and observed values of the signal strengths for the single-channel, combined 1-POI, and combined 2-POI fits, and table 10 shows the observed values of the normalisation factors for the combined 2-POI fit. Figure 12 shows the observed values of the total WH, ZH, and VH cross-sections times the $H \to WW^*$ branching ratio, normalised to the SM predictions, and figure 13 shows the observed profile likelihood for the combined

Channel	SR	SR discriminant	Relevant CR(s)
Opposite-sign 2ℓ	—	$\text{ANN}^{VH}_{\text{DFOS}}$ (2(a))	Top, Z+jets, WW
Same-sign 2ℓ	SS2μ	RNN output (3(a))	–
	SS$2e$	RNN output (3(b))	
	SSDF	RNN output (3(c))	
3ℓ	Z-dominated	ANN_{Zdom} (4(a))	WZ 0-jet, WZ $\geq$1-jets
	Z-depleted	$\text{ANN}^{\Delta}_{\text{Zdep}}$ (4(b))	
4ℓ	1-SFOS	1-SFOS BDT output (5(a))	ZZ
	2-SFOS	2-SFOS BDT output (5(b))	

Table 7. Summary of SRs — including the chosen SR discriminants — and CRs in each channel entering the combined total cross-section fit. The SR discriminants enter the combined fit as histograms, and the corresponding figures showing the post-fit histograms are referred in parentheses after each SR discriminant; the CRs enter the combined fit as counters.

and single-channel results. Figure 14 shows the two-dimensional likelihood contours of the observed values of $\sigma_{ZH} \times \mathcal{B}_{H\to WW^*}$ vs. $\sigma_{WH} \times \mathcal{B}_{H\to WW^*}$ compared with the SM predictions.

For the combined 1-POI fit, the VH signal strength is measured to be:

$$\mu_{VH} = 0.92^{+0.21}_{-0.20}\,(\text{stat.})^{+0.13}_{-0.12}\,(\text{syst.})\,,$$

corresponding to a 4.5σ significance over the background-only hypothesis and consistent with the SM expectation with a p-value of 73%. The total VH cross-section times the $H \to WW^*$ branching ratio is measured to be:

$$\sigma_{VH} \times \mathcal{B}_{H\to WW^*} = 0.44^{+0.10}_{-0.09}\,(\text{stat.})^{+0.06}_{-0.05}\,(\text{syst.})\,\text{pb}\,,$$

in agreement with the SM expectation of $0.48 \pm 0.01\,\text{pb}$ [21].

For the combined 2-POI fit, the WH and ZH signal strengths are measured to be:

$$\begin{aligned} \mu_{WH} &= 0.48^{+0.26}_{-0.25}\,(\text{stat.})^{+0.18}_{-0.16}\,(\text{syst.})\,, \\ \mu_{ZH} &= 1.6^{+0.5}_{-0.4}\,(\text{stat.}) \pm 0.2\,(\text{syst.})\,. \end{aligned} \tag{9.1}$$

The observed values of μ_{WH} and μ_{ZH} are compatible at a level of 2.0σ, and they are consistent with the SM expectations with a p-value of 13%. The observed ZH result exceeds the SM prediction due to an excess in the 4ℓ 1-SFOS SR. The observed μ_{WH} is smaller than the SM prediction due to deficits in the 3ℓ Z-depleted SR and the same-sign 2ℓ channel. The total WH and ZH cross-sections times the $H \to WW^*$ branching ratio are measured to be:

$$\begin{aligned} \sigma_{WH} \times \mathcal{B}_{H\to WW^*} &= 0.14^{+0.08}_{-0.07}\,(\text{stat.}) \pm 0.05\,(\text{syst.})\,\text{pb}\,, \\ \sigma_{ZH} \times \mathcal{B}_{H\to WW^*} &= 0.31^{+0.09}_{-0.08}\,(\text{stat.}) \pm 0.03\,(\text{syst.})\,\text{pb}\,, \end{aligned} \tag{9.2}$$

while the SM expectations are $0.294 \pm 0.009\,\text{pb}$ (WH) and $0.190^{+0.009}_{-0.008}\,\text{pb}$ (ZH), respectively [21].

JHEP08(2025)034

Process	OS 2ℓ	SS 2ℓ		
		SS2μ	SS2e	SSDF
WH	11 ± 7	33 ± 21	12 ± 8	48 ± 31
ZH	20 ± 6	7.2 ± 2.2	4.1 ± 1.2	14 ± 4
Other Higgs	61 ± 14	19.0 ± 2.2	9.3 ± 1.1	33 ± 4
WW	260 ± 50	260 ± 40	109 ± 15	380 ± 50
WZ	41.5 ± 3.1	1420 ± 150	850 ± 90	2630 ± 270
ZZ	7.8 ± 0.7	144 ± 17	101 ± 8	309 ± 28
Z+γ	10 ± 7	—	—	—
VVV	19 ± 6	190 ± 50	86 ± 24	290 ± 80
Z+jets	302 ± 27	—	—	—
Top	1020 ± 70	33.0 ± 2.7	16.2 ± 1.3	54 ± 5
Mis-identified leptons	25 ± 6	320 ± 130	1090 ± 100	2080 ± 260
Charge-flip electrons	—	—	930 ± 70	109 ± 8
Total	1780 ± 40	2420 ± 50	3200 ± 50	5950 ± 70
Observed	1788	2438	3233	5906

Process	3ℓ		4ℓ	
	Z-dominated	Z-depleted	1-SFOS	2-SFOS
WH	12 ± 7	6 ± 4	—	—
ZH	4.4 ± 1.3	1.7 ± 0.5	15 ± 4	10.7 ± 3.2
Other Higgs	1.80 ± 0.17	2.83 ± 0.31	1.88 ± 0.22	0.68 ± 0.08
WZ	877 ± 20	24.6 ± 1.6	—	—
ZZ	130 ± 17	2.63 ± 0.28	29.2 ± 1.5	306 ± 9
WWW	64 ± 16	35 ± 9	—	—
WWZ	3.81 ± 0.09	1.64 ± 0.05	10.9 ± 1.0	1.58 ± 0.14
WZZ	0.310 ± 0.008	< 0.1	0.447 ± 0.034	< 0.1
Top	14.5 ± 1.3	4.8 ± 0.4	8.8 ± 0.9	1.45 ± 0.14
Mis-identified leptons	98 ± 14	12.5 ± 2.9	14.5 ± 3.2	5.5 ± 1.2
Total	1205 ± 23	92 ± 8	80 ± 5	326 ± 9
Observed	1237	88	79	316

Table 8. Post-fit signal, background, and observed data yields in each SR as measured by the 2-POI fit. The Z+jets and top processes for a given channel correspond to those with only prompt leptons, as described in section 7. The uncertainties correspond to the total of all statistical and systematic sources. The quadrature sum of the individual sources may differ from the total uncertainty due to correlations.

JHEP08(2025)034

Channel	POI / Z_0	Expected	Observed
Opposite-sign 2ℓ	μ_{VH}	1.0 ± 1.0	$1.9^{+1.1}_{-1.0}$
	Z_0	1.0	1.9
Same-sign 2ℓ	μ_{WH}	1.0 ± 0.5	0.1 ± 0.5
	Z_0	1.8	0.2
3ℓ	μ_{WH}	1.0 ± 0.4	0.6 ± 0.4
	Z_0	2.8	1.8
4ℓ	μ_{ZH}	$1.0^{+0.5}_{-0.4}$	1.6 ± 0.5
	Z_0	3.1	4.4
Combined 1-POI	μ_{VH}	$1.00^{+0.26}_{-0.24}$	$0.92^{+0.25}_{-0.23}$
	Z_0	4.8	4.5
Combined 2-POI	μ_{WH}	$1.00^{+0.35}_{-0.33}$	$0.48^{+0.32}_{-0.30}$
	μ_{ZH}	$1.0^{+0.5}_{-0.4}$	1.6 ± 0.5
	Z_0^{WH}	3.3	1.6
	Z_0^{ZH}	3.1	4.5

Table 9. The observed values of the signal strengths and the corresponding statistical significances, Z_0, for the single-channel fits and the combined 1- and 2-POI fits. For each fit, both the expected and observed results are shown. The uncertainties correspond to the total of all statistical and systematic sources. The statistical significances are quoted in units of standard deviations above the background-only hypothesis.

Channel	Background	Normalisation factor
Opposite-sign 2ℓ	Top	$1.0^{+0.3}_{-0.2}$
	Z+jets	$0.86^{+0.15}_{-0.14}$
	WW	$0.9^{+0.3}_{-0.2}$
Same-sign 2ℓ	WZ	$0.90^{+0.17}_{-0.16}$
3ℓ	WZ 0-jet	1.03 ± 0.06
	WZ $\geq$1-jets	$0.88^{+0.16}_{-0.15}$
	WWW	$2.2^{+0.7}_{-0.6}$
4ℓ	ZZ	0.98 ± 0.07

Table 10. The observed values of the background normalisation factors for the combined 2-POI fit. The uncertainties correspond to the total of all statistical and systematic sources.

JHEP08(2025)034

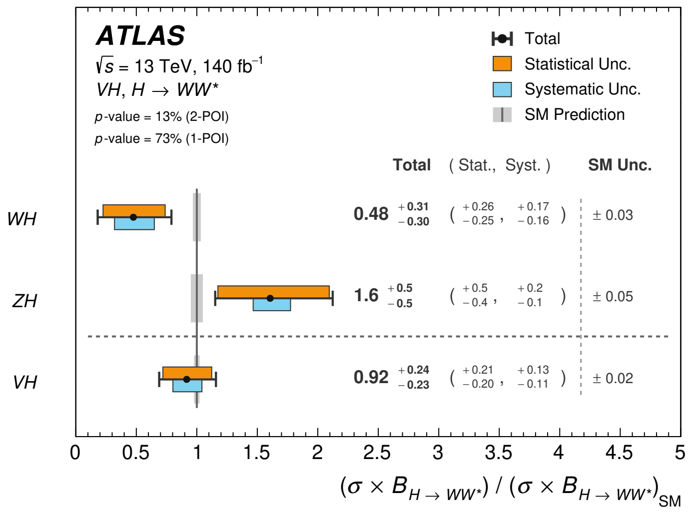

Figure 12. Best-fit values of the total WH, ZH, and VH cross-sections times the $H \to WW^*$ branching ratio. The WH/ZH and VH results are obtained from the combined 2- and 1-POI cross-section fits, respectively. Each measurement is normalised to its SM prediction. The black error bars, orange boxes, and blue boxes show the total, statistical, and systematic uncertainties in the measurements, respectively. The grey bands represent the theory uncertainty of the corresponding Higgs boson production mode, calculated from the sources of uncertainty described in section 8.2.

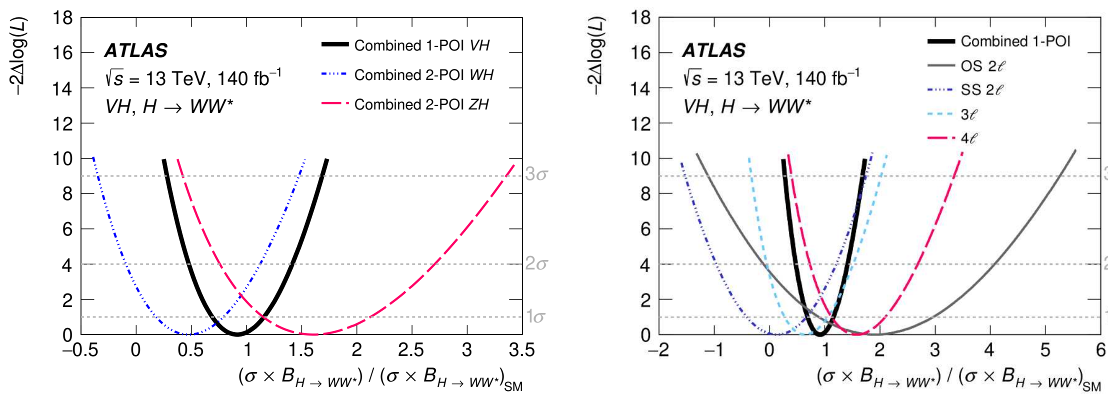

(a) (b)

Figure 13. Observed profile likelihood as a function of $\sigma \times \mathcal{B}_{H \to WW^*}$ normalised by the SM expectation for (a) the VH and WH/ZH measurements from the combined 1- and 2-POI fits, respectively, and (b) the single-channel measurements.

Table 11 shows the relative impact of the different sources of uncertainty in the observed values of the total cross-sections. For all fit scenarios, the observed results are dominated by statistical uncertainties in data. For the WH measurement, the RNN shape uncertainty for WZ (23%) and the WZ 0-jet (11%) and VVV (12%) background uncertainties are the dominant systematic uncertainties; for the ZH measurement, muon experimental uncertainties (4.1%), primarily on the efficiency of the isolation selection, are the dominant systematic uncertainties.

JHEP08(2025)034

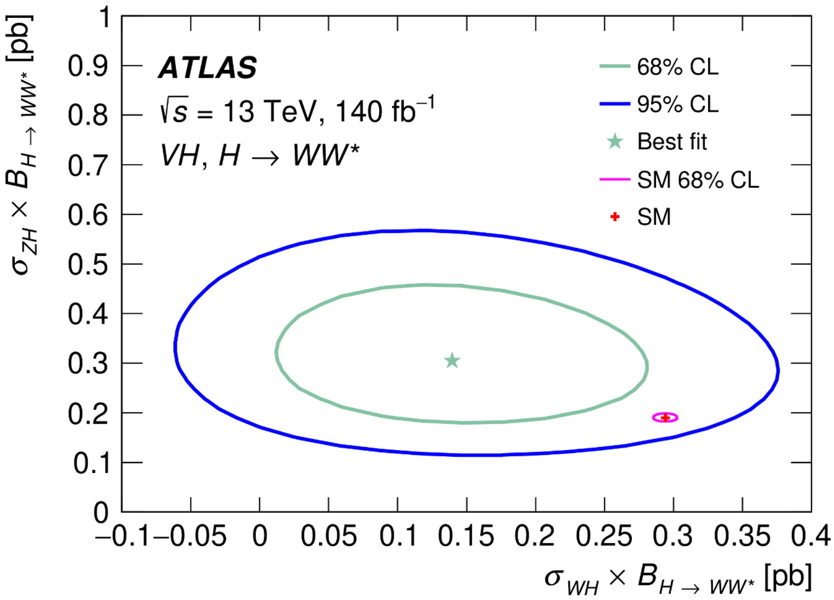

Figure 14. Two-dimensional likelihood contours of the observed values of $\sigma_{ZH} \times \mathcal{B}_{H\to WW^*}$ vs. $\sigma_{WH} \times \mathcal{B}_{H\to WW^*}$ at the 68% and 95% confidence levels (CLs) compared with the predictions from the SM. The 68% confidence level on the SM predictions for the ZH and WH cross-sections times branching fraction is indicated by the magenta ellipse.

9.2.2 Differential cross-section results

For the differential cross-section measurement, two fits are performed: one for the p_{T}^{V} scheme and one for the STXS scheme. The analysis regions are the same for both the fits. The signal samples are split into signal templates following the STXS Stage 1.2 categorisation. The cross-section for each template is scaled by its own POI, $(\sigma \times \mathcal{B}_{H\to WW^*})/(\sigma \times \mathcal{B}_{H\to WW^*})_{\mathrm{SM}}$. The POIs are correlated (i.e., coherently tuned via a single POI) to provide the results in merged bins of the STXS categorisation; for example, the POIs for different jet multiplicity bins are correlated as are the POIs for the $250 \leq p_{\mathrm{T}}^{V} < 400\,\mathrm{GeV}$ and $p_{\mathrm{T}}^{V} \geq 400\,\mathrm{GeV}$ bins.

For the p_{T}^{V} scheme, the POIs for the WH and ZH production modes are correlated to provide combined VH production mode POIs; for the $V \to q\bar{q}$ signal template fit, the signal is split into four p_{T}^{V} bins and the POIs are correlated with those of the $V \to \ell\ell/\nu\nu$ channels.

The fitted POIs and normalisation factors for the p_{T}^{V} and STXS schemes are summarised in tables 12 and 13, respectively. The POIs are plotted in figure 15.

Due to deficits in data in several bins of the analysis — in particular the SS2μ region — some of observed POIs are close to zero. Moreover, the expected total yield becomes negative for large negative values of the POIs; therefore, a constraint was imposed on the POI for the $VH, p_{\mathrm{T}}^{V} \geq 250\,\mathrm{GeV}$ category in the p_{T}^{V} scheme and on the POI for the $\ell\ell H, p_{\mathrm{T}}^{V} \geq 150\,\mathrm{GeV}$ category in the STXS scheme. In both the cases, the lower limit of the 68% confidence interval cannot be reached before the likelihood becomes ill-defined due to negative expected yields in some bins. The value at which this happens is specified in tables 12 and 13. Given that this indicates a very low expected signal yield, a test of the validity of the asymptotic approximation was performed on such parameters. A small degree of over-coverage (70% with

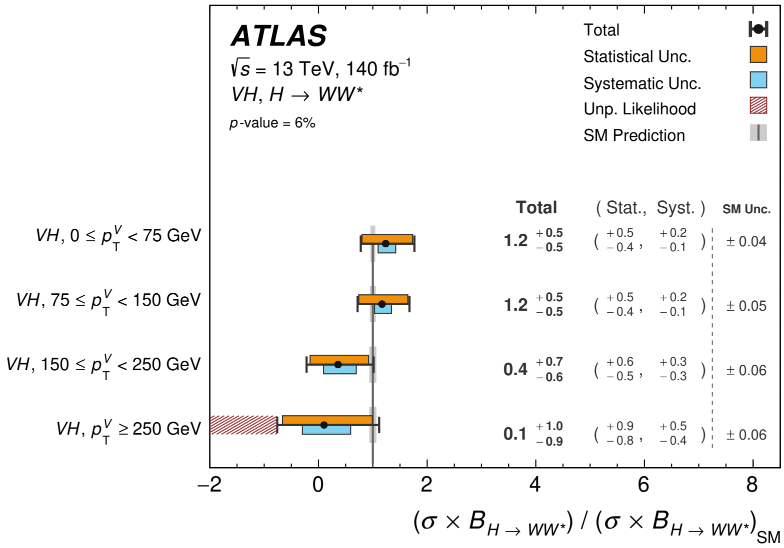

(a)

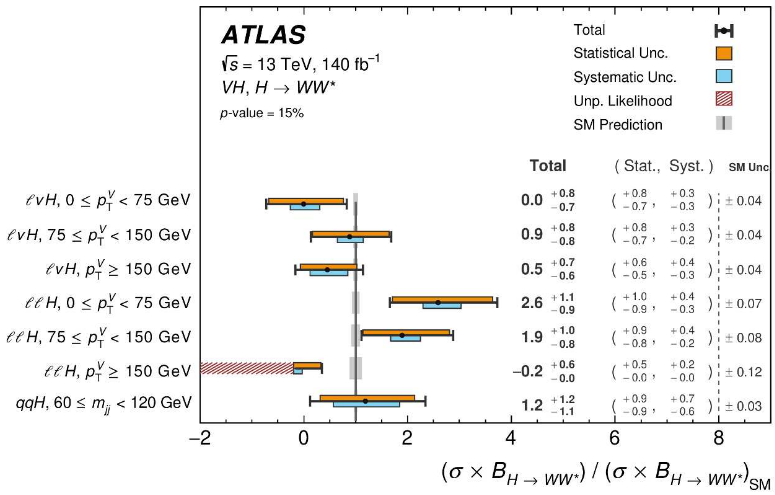

(b)

Figure 15. Best-fit values of the cross-sections times the $H \to WW^*$ branching ratio measured in the (a) p_{T}^{V} and (b) STXS schemes. Each cross-section is normalised to its SM prediction. The black error bars, orange boxes, and blue boxes show the total, statistical, and systematic uncertainties in the measurements, respectively. The grey bands represent the theory uncertainty of the corresponding Higgs boson production mode, calculated from the sources of uncertainty described in Section 8.2. The hatched band indicated with "Unp. Likelihood" shows the region of the parameter space where the likelihood becomes unphysical.

JHEP08(2025)034

Source	$\frac{\Delta(\sigma_{VH}\times\mathcal{B}_{H\to WW^*})}{\sigma_{VH}\times\mathcal{B}_{H\to WW^*}}$ [%]	$\frac{\Delta(\sigma_{WH}\times\mathcal{B}_{H\to WW^*})}{\sigma_{WH}\times\mathcal{B}_{H\to WW^*}}$ [%]	$\frac{\Delta(\sigma_{ZH}\times\mathcal{B}_{H\to WW^*})}{\sigma_{ZH}\times\mathcal{B}_{H\to WW^*}}$ [%]
Statistical uncertainties in data	22	54	29
Statistical uncertainties in SR data	20	46	28
Statistical uncertainties in CR data	10	29	6.3
Systematic uncertainties	13	35	10
Statistical uncertainties in simulation	6.2	13	5.9
Experimental systematic uncertainties	5.4	12	5.7
Electrons	1.1	1.6	1.6
Muons	2.7	3.0	4.1
Jet energy scale	1.0	3.1	0.5
Jet energy resolution	0.5	2.4	0.6
Flavour tagging	1.0	1.5	0.8
Missing transverse momentum	0.6	0.2	0.9
Pile-up	1.0	1.3	0.8
Luminosity	1.1	1.2	1.1
Mis-identified leptons	3.7	10	2.8
Charge-flip electrons	1.7	5.0	0.0
Theoretical uncertainties	6.9	20	4.2
WH	2.1	2.3	0.1
ZH	0.5	0.3	2.4
Other H	1.2	2.4	0.9
WW	1.2	3.7	0.2
WZ 0-jet	3.2	11	0.2
WZ $\geq$1-jets	3.2	9.7	0.4
ZZ	1.2	2.1	0.8
VVV	2.7	12	1.0
Top	2.8	5.0	2.4
Z+jets	1.6	2.9	1.5
RNN shape uncertainty for WZ	7.5	23	0.7
Total	26	64	30

Table 11. Breakdown of the average contributions to the total uncertainties (in percentage) in the observed values of the cross-sections for the combined 1-POI ($\sigma_{VH} \times \mathcal{B}_{H\to WW^*}$) and 2-POI ($\sigma_{WH} \times \mathcal{B}_{H\to WW^*}$ and $\sigma_{ZH} \times \mathcal{B}_{H\to WW^*}$) fits. Indentation is used to denote subcategories. The quadrature sum of the individual sources may differ from the total uncertainty due to correlations.

respect to 68%) of the confidence interval was observed for the POI for the $\ell\ell H, p_{\mathrm{T}}^{V} \geq 150$ GeV category. The confidence interval is defined as in ref. [142].

There are also some notable differences in the normalisation factors obtained from the total and differential cross-section measurements. For the opposite-sign 2ℓ channel, the top normalisation factor in the differential cross-section measurement is smaller than that obtained in the total cross-section measurement. The nuisance parameter which tunes the $t\bar{t}$ parton-shower modelling uncertainty is sensitive to the p_{T}^{V} modelling; therefore, it can be pulled differently in the two measurements. In the case of the differential cross-section

Fit results for the p_{T}^{V} scheme					
Normalisation factors		$(\sigma_{\text{category}} \times \mathcal{B}_{H\to WW^*})/(\sigma_{\text{category}} \times \mathcal{B}_{H\to WW^*})_{\text{SM}}$			
Parameter	Fit result	Category	Fit result	Stat. unc.	Syst. unc.
Top	$0.9^{+0.3}_{-0.2}$	$VH, 0 \leq p_{\mathrm{T}}^{V} < 75\,\text{GeV}$	1.2 ± 0.5	$^{+0.5}_{-0.4}$	$^{+0.2}_{-0.1}$
Z+jets	$0.86^{+0.12}_{-0.11}$	$VH, 75 \leq p_{\mathrm{T}}^{V} < 150\,\text{GeV}$	1.2 ± 0.5	$^{+0.5}_{-0.4}$	$^{+0.2}_{-0.1}$
WW	$0.9^{+0.3}_{-0.2}$	$VH, 150 \leq p_{\mathrm{T}}^{V} < 250\,\text{GeV}$	$0.4^{+0.7}_{-0.6}$	$^{+0.6}_{-0.5}$	± 0.3
WZ (SS 2ℓ)	$1.12^{+0.17}_{-0.15}$	$VH, p_{\mathrm{T}}^{V} \geq 250\,\text{GeV}$	$0.1^{+1.0}_{-0.9\,\text{(LL)}}$	$^{+0.9}_{-0.8}$	$^{+0.5}_{-0.4}$
WZ 0-jet	1.00 ± 0.06				
WZ $\geq$1-jets	$0.89^{+0.16}_{-0.15}$				
WWW	$2.0^{+0.6}_{-0.5}$				
ZZ	1.00 ± 0.03				

Table 12. Observed fit results for the p_{T}^{V} scheme. "Stat. unc." and "Syst. unc." indicate the statistical and systematic components, respectively, of the total uncertainty in the corresponding POI. For the normalisation factors, only the total uncertainties are quoted. A lower limit on the POI for the $VH, p_{\mathrm{T}}^{V} \geq 250\,\text{GeV}$ category was set at -0.76 to prevent the likelihood from reaching an unphysical region with zero observed and zero expected events in any bin of the analysis. The label "LL" indicates that the interval reaches its minimum allowed value. A 95% confidence level upper limit on the POI for the $VH, p_{\mathrm{T}}^{V} \geq 250\,\text{GeV}$ category was computed and found to be 2.1. In the limit computation, the other POIs were left free to float.

Fit results for the STXS scheme					
Normalisation factors		$(\sigma_{\text{STXS category}} \times \mathcal{B}_{H\to WW^*})/(\sigma_{\text{STXS category}} \times \mathcal{B}_{H\to WW^*})_{\text{SM}}$			
Parameter	Fit result	STXS category	Fit result	Stat. unc.	Syst. unc.
Top	$0.9^{+0.3}_{-0.2}$	$\ell\nu H, 0 \leq p_{\mathrm{T}}^{V} < 75\,\text{GeV}$	$0.0^{+0.8}_{-0.7}$	$^{+0.8}_{-0.7}$	± 0.3
Z+jets	$0.85^{+0.12}_{-0.11}$	$\ell\nu H, 75 \leq p_{\mathrm{T}}^{V} < 150\,\text{GeV}$	0.9 ± 0.8	$^{+0.8}_{-0.7}$	$^{+0.3}_{-0.2}$
WW	$0.9^{+0.3}_{-0.2}$	$\ell\nu H, p_{\mathrm{T}}^{V} \geq 150\,\text{GeV}$	$0.5^{+0.7}_{-0.6}$	$^{+0.6}_{-0.5}$	$^{+0.4}_{-0.3}$
WZ (SS 2ℓ)	$1.14^{+0.17}_{-0.15}$	$\ell\ell H, 0 \leq p_{\mathrm{T}}^{V} < 75\,\text{GeV}$	$2.6^{+1.1}_{-0.9}$	$^{+1.0}_{-0.9}$	$^{+0.4}_{-0.3}$
WZ 0-jet	1.00 ± 0.06	$\ell\ell H, 75 \leq p_{\mathrm{T}}^{V} < 150\,\text{GeV}$	$1.9^{+1.0}_{-0.8}$	$^{+0.9}_{-0.8}$	$^{+0.4}_{-0.2}$
WZ $\geq$1-jets	$0.88^{+0.16}_{-0.15}$	$\ell\ell H, p_{\mathrm{T}}^{V} \geq 150\,\text{GeV}$	$-0.2^{+0.6}_{-0.0\,\text{(LL)}}$	$^{+0.5}_{-0.0\,\text{(LL)}}$	$^{+0.2}_{-0.0\,\text{(LL)}}$
WWW	$2.2^{+0.7}_{-0.6}$	$qqH, 60 \leq m_{jj} < 120\,\text{GeV}$	$1.2^{+1.2}_{-1.1}$	± 0.9	$^{+0.7}_{-0.6}$
ZZ	0.99 ± 0.03				

Table 13. Observed fit results for the STXS scheme. "Stat. unc." and "Syst. unc." indicate the statistical and systematic components, respectively, of the total uncertainty in the corresponding POI. For the normalisation factors, only the total uncertainties are quoted. A lower limit on the POI for the $\ell\ell H, p_{\mathrm{T}}^{V} \geq 150\,\text{GeV}$ category was set at -0.2 to prevent the likelihood from reaching an unphysical region with zero observed and zero expected events in any bin of the analysis. The label "LL" indicates that the interval reaches its minimum allowed value. A 95% confidence level upper limit on the POI for the $\ell\ell H, p_{\mathrm{T}}^{V} \geq 150\,\text{GeV}$ category was computed and found to be 1.6. In the limit computation, the other POIs were left free to float.

JHEP08(2025)034

$\sigma \times \mathcal{B}_{H\to WW^*}$ [fb]									
p_{T}^{V} scheme ($\lvert y_H\rvert < 2.5$)					STXS scheme				
p_{T}^{V} interval [GeV]	Value	Stat. unc.	Syst. unc.	SM	STXS category [p_{T}^{V} and m_{jj} in GeV]	Value	Stat. unc.	Syst. unc.	SM
$VH\,(0 \leq p_{\mathrm{T}}^{V} < 75)$	270	$^{+110}_{-100}$	$^{+40}_{-30}$	220 ± 40	$\ell\nu H\,(0 \leq p_{\mathrm{T}}^{V} < 75)$	0	$^{+40}_{-30}$	± 10	46.3 ± 1.8
$VH\,(75 \leq p_{\mathrm{T}}^{V} < 150)$	180	$^{+70}_{-60}$	$^{+30}_{-20}$	151 ± 34	$\ell\nu H\,(75 \leq p_{\mathrm{T}}^{V} < 150)$	26	$^{+22}_{-21}$	$^{+8}_{-7}$	28.9 ± 1.2
$VH\,(150 \leq p_{\mathrm{T}}^{V} < 250)$	18	$^{+28}_{-26}$	$^{+17}_{-13}$	50 ± 15	$\ell\nu H\,(p_{\mathrm{T}}^{V} \geq 150)$	5	± 6	± 4	11.5 ± 0.5
$VH\,(p_{\mathrm{T}}^{V} \geq 250)$	1	$^{+12}_{-11}$	$^{+7}_{-6}$	14 ± 4	$\ell\ell H\,(0 \leq p_{\mathrm{T}}^{V} < 75)$	62	$^{+25}_{-21}$	$^{+11}_{-7}$	24.1 ± 1.7
					$\ell\ell H\,(75 \leq p_{\mathrm{T}}^{V} < 150)$	35	$^{+17}_{-14}$	$^{+7}_{-4}$	18.7 ± 1.5
					$\ell\ell H\,(p_{\mathrm{T}}^{V} \geq 150)$	-2	$^{+5}_{-0\,\text{(LL)}}$	$^{+1}_{-0\,\text{(LL)}}$	8.7 ± 1.0
					$qqH\,(60 \leq m_{jj} < 120)$	110	$^{+90}_{-80}$	± 60	91.8 ± 3.3

Table 14. Observed cross-sections times the $H \to WW^*$ branching ratio for the p_{T}^{V} and STXS schemes. "Stat. unc." and "Syst. unc." indicate the statistical and systematic components, respectively, of the total uncertainty on the corresponding POI. "SM" indicates the SM expectation, whose uncertainty is calculated from the sources described in section 8.2. Lower limits on $(\sigma \times \mathcal{B}_{H\to WW^*})/(\sigma \times \mathcal{B}_{H\to WW^*})_{\mathrm{SM}}$ for the $VH, p_{\mathrm{T}}^{V} \geq 250\,\mathrm{GeV}$ category in the p_{T}^{V} scheme and the $\ell\ell H, p_{\mathrm{T}}^{V} \geq 150\,\mathrm{GeV}$ category in the STXS scheme were set at -0.76 and -0.2, respectively, to prevent the likelihoods from reaching unphysical regions. The label "LL" indicates that the interval reaches its minimum allowed value.

measurement, the best-fit value of this nuisance parameter increases the $t\bar{t}$ yield in the top CR. To compensate for such an increase, the top normalisation factor decreases. For the same-sign 2ℓ channel, the WZ normalisation factor in the differential cross-section measurement is larger than that obtained in the total cross-section measurement. The WZ normalisation factor is driven by the background-like bins of the signal regions in the same-sign 2ℓ channel. As those signal regions are split differently in the two measurement scenarios, the resulting WZ normalisation factors are also different.

The POIs were converted to fiducial cross-sections by multiplying the POIs by the cross-sections used to normalise the signal templates in each bin of the p_{T}^{V} and STXS schemes. The resulting values are shown in table 14. The differential cross-section as a function of p_{T}^{V} is shown in figure 16.

Finally, tables 20 and 21 of appendix C show the fractional contributions from statistical and systematic sources to the total uncertainties reported in p_{T}^{V} and STXS schemes, respectively. As for the total cross-section measurement, the differential results are dominated by statistical uncertainties in data.

10 Conclusions

A measurement of the total Higgs boson production cross-sections via associated WH and ZH production using $H \to WW^* \to \ell\nu\ell\nu$ and $H \to WW^* \to \ell\nu jj$ decays is presented. Results for combined WH and ZH production are also presented. The analysis uses proton-proton events delivered by the Large Hadron Collider at a centre-of-mass energy of 13 TeV and recorded by the ATLAS detector between 2015 and 2018. The data correspond to an integrated luminosity of $140\,\mathrm{fb}^{-1}$. The VH signal strength is measured to be $0.92^{+0.21}_{-0.20}\,(\text{stat.})^{+0.13}_{-0.12}\,(\text{syst.})$, corresponding to a 4.5σ significance over the background-only hypothesis. The products of the $H \to WW^*$ branching fraction times the WH and ZH cross-sections are measured to be $0.14^{+0.08}_{-0.07}\,(\text{stat.}) \pm 0.05\,(\text{syst.})$ pb and $0.31^{+0.09}_{-0.08}\,(\text{stat.}) \pm 0.03\,(\text{syst.})$ pb, respectively, in agreement with the Standard Model predictions. Differential cross-sections have also been

JHEP08(2025)034

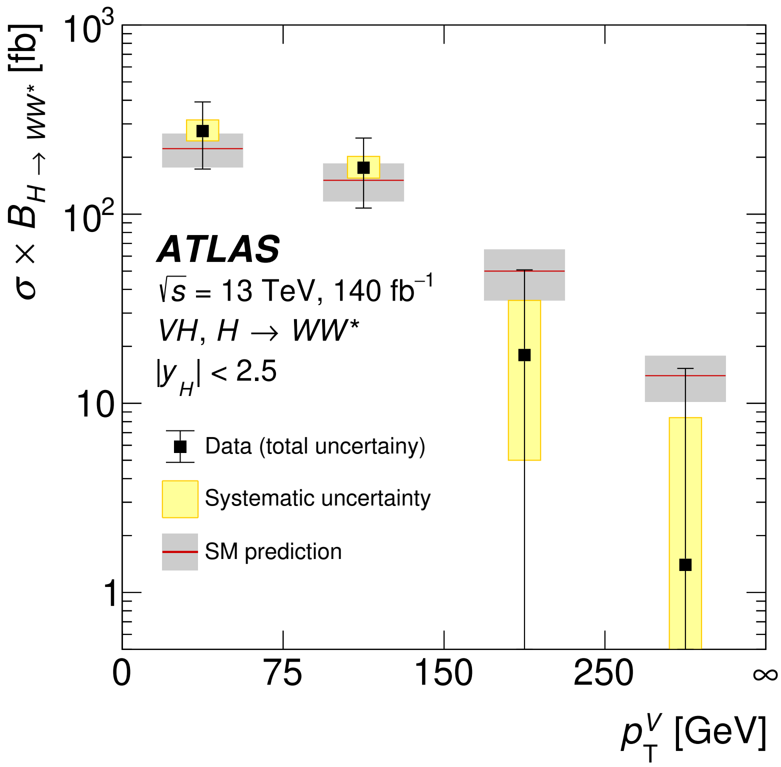

Figure 16. Differential VH production cross-section as a function of the $p_{\rm T}$ of the associated vector boson. The theoretical expectation is also shown, whose uncertainty is calculated from the sources described in section 8.2.

measured, $\sigma_{VH} \times \mathcal{B}_{H\to WW^*}$ as a function of the $p_{\rm T}$ of the associated vector boson and Simplified Template Cross-Sections for VH and EW qqH production. The results obtained are in agreement with their Standard Model expectations.

Acknowledgments

We thank CERN for the very successful operation of the LHC and its injectors, as well as the support staff at CERN and at our institutions worldwide without whom ATLAS could not be operated efficiently.

The crucial computing support from all WLCG partners is acknowledged gratefully, in particular from CERN, the ATLAS Tier-1 facilities at TRIUMF/SFU (Canada), NDGF (Denmark, Norway, Sweden), CC-IN2P3 (France), KIT/GridKA (Germany), INFN-CNAF (Italy), NL-T1 (Netherlands), PIC (Spain), RAL (U.K.) and BNL (U.S.A.), the Tier-2 facilities worldwide and large non-WLCG resource providers. Major contributors of computing resources are listed in ref. [143].

JHEP08(2025)034

We gratefully acknowledge the support of ANPCyT, Argentina; YerPhI, Armenia; ARC, Australia; BMWFW and FWF, Austria; ANAS, Azerbaijan; CNPq and FAPESP, Brazil; NSERC, NRC and CFI, Canada; CERN; ANID, Chile; CAS, MOST and NSFC, China; Minciencias, Colombia; MEYS CR, Czech Republic; DNRF and DNSRC, Denmark; IN2P3-CNRS and CEA-DRF/IRFU, France; SRNSFG, Georgia; BMBF, HGF and MPG, Germany; GSRI, Greece; RGC and Hong Kong SAR, China; ISF and Benoziyo Center, Israel; INFN, Italy; MEXT and JSPS, Japan; CNRST, Morocco; NWO, Netherlands; RCN, Norway; MNiSW, Poland; FCT, Portugal; MNE/IFA, Romania; MSTDI, Serbia; MSSR, Slovakia; ARIS and MVZI, Slovenia; DSI/NRF, South Africa; MICIU/AEI, Spain; SRC and Wallenberg Foundation, Sweden; SERI, SNSF and Cantons of Bern and Geneva, Switzerland; NSTC, Taipei; TENMAK, Türkiye; STFC/UKRI, United Kingdom; DOE and NSF, United States of America.

Individual groups and members have received support from BCKDF, CANARIE, CRC and DRAC, Canada; CERN-CZ, FORTE and PRIMUS, Czech Republic; COST, ERC, ERDF, Horizon 2020, ICSC-NextGenerationEU and Marie Skłodowska-Curie Actions, European Union; Investissements d'Avenir Labex, Investissements d'Avenir Idex and ANR, France; DFG and AvH Foundation, Germany; Herakleitos, Thales and Aristeia programmes co-financed by EU-ESF and the Greek NSRF, Greece; BSF-NSF and MINERVA, Israel; NCN and NAWA, Poland; La Caixa Banking Foundation, CERCA Programme Generalitat de Catalunya and PROMETEO and GenT Programmes Generalitat Valenciana, Spain; Göran Gustafssons Stiftelse, Sweden; The Royal Society and Leverhulme Trust, United Kingdom.

In addition, individual members wish to acknowledge support from Armenia: Yerevan Physics Institute (FAPERJ); CERN: European Organization for Nuclear Research (CERN PJAS); Chile: Agencia Nacional de Investigación y Desarrollo (FONDECYT 1230812, FONDECYT 1230987, FONDECYT 1240864); China: Chinese Ministry of Science and Technology (MOST-2023YFA1605700, MOST-2023YFA1609300), National Natural Science Foundation of China (NSFC — 12175119, NSFC — 12275265, NSFC — 12075060); Czech Republic: Czech Science Foundation (GACR — 24-11373S), Ministry of Education Youth and Sports (ERC-CZ-LL2327, FORTE CZ.02.01.01/00/22_008/0004632), PRIMUS Research Programme (PRIMUS/21/SCI/017); EU: H2020 European Research Council (ERC — 101002463); European Union: European Research Council (ERC — 948254, ERC 101089007), Horizon 2020 Framework Programme (MUCCA — CHIST-ERA-19-XAI-00), European Union, Future Artificial Intelligence Research (FAIR-NextGenerationEU PE00000013), Italian Center for High Performance Computing, Big Data and Quantum Computing (ICSC, NextGenerationEU); France: Agence Nationale de la Recherche (ANR-20-CE31-0013, ANR-21-CE31-0013, ANR-21-CE31-0022, ANR-22-EDIR-0002), Investissements d'Avenir Labex (ANR-11-LABX-0012); Germany: Baden-Württemberg Stiftung (BW Stiftung-Postdoc Eliteprogramme), Deutsche Forschungsgemeinschaft (DFG — 469666862, DFG — CR 312/5-2); Italy: Istituto Nazionale di Fisica Nucleare (ICSC, NextGenerationEU), Ministero dell'Università e della Ricerca (NextGenEU I53D23000820006 M4C2.1.1); Japan: Japan Society for the Promotion of Science (JSPS KAKENHI JP22H01227, JSPS KAKENHI JP22H04944, JSPS KAKENHI JP22KK0227, JSPS KAKENHI JP23KK0245); Netherlands: Netherlands Organisation for Scientific Research (NWO Veni 2020 — VI.Veni.202.179);

JHEP08(2025)034

Norway: Research Council of Norway (RCN-314472); Poland: Ministry of Science and Higher Education (IDUB AGH, POB8, D4 no 9722), Polish National Agency for Academic Exchange (PPN/PPO/2020/1/00002/U/00001), Polish National Science Centre (NCN 2021/42/E/ST2/00350, NCN OPUS 2022/47/B/ST2/03059, NCN UMO-2019/34/E/ST2/00393, NCN & H2020 MSCA 945339, UMO-2020/37/B/ST2/01043, UMO-2021/40/C/ST2/00187, UMO-2022/47/O/ST2/00148, UMO-2023/49/B/ST2/04085, UMO-2023/51/B/ST2/00920); Portugal: Foundation for Science and Technology (FCT); Slovenia: Slovenian Research Agency (ARIS grant J1-3010); Spain: Generalitat Valenciana (Artemisa, FEDER, IDIFEDER/2018/048), Ministry of Science and Innovation (MCIN & NextGenEU PCI2022-135018-2, MICIN & FEDER PID2021-125273NB, RYC2019-028510-I, RYC2020-030254-I, RYC2021-031273-I, RYC2022-038164-I); Sweden: Carl Trygger Foundation (CTS 22:2312), Swedish Research Council (VR 2023-04654, VR 2018-00482, VR 2021-03651, VR 2022-03845, VR 2022-04683, VR 2023-03403), Knut and Alice Wallenberg Foundation (KAW 2018.0458, KAW 2019.0447, KAW 2022.0358); Switzerland: Swiss National Science Foundation (SNSF — PCEFP2_194658); United Kingdom: Leverhulme Trust (Leverhulme Trust RPG-2020-004), Royal Society (NIF-R1-231091); United States of America: U.S. Department of Energy (ECA DE-AC02-76SF00515), Neubauer Family Foundation.

Variable(s)	Description
$p_{\mathrm{T}}^{\ell_0}$, $p_{\mathrm{T}}^{\ell_1}$	Leading and subleading lepton transverse momentum
$m_{\ell\ell}$	Dilepton invariant mass
$\Delta\phi_{\ell\ell}$	Dilepton azimuthal separation
$\lvert\Delta y_{\ell\ell}\rvert$	Dilepton rapidity separation
m_{T}	Transverse mass (eq. 6.1)
$p_{\mathrm{T}}^{j_0}$, $p_{\mathrm{T}}^{j_1}$	Leading and subleading jet transverse momentum
m_{jj}	Dijet invariant mass
$\Delta\phi_{jj}$	Dijet azimuthal separation
$\lvert\Delta y_{jj}\rvert$	Dijet rapidity separation
$m_{\ell_0 j_0}$, $m_{\ell_0 j_1}$, $m_{\ell_1 j_0}$, $m_{\ell_1 j_1}$	All lepton-jet invariant mass combinations
$m_{\tau\tau}$	Invariant mass of the τ-lepton pair using the collinear approximation [133], assuming the electrons and muons result from τ-lepton decays
$E_{\mathrm{T}}^{\mathrm{miss}}$	Missing transverse momentum
$\mathcal{S}_{\mathrm{miss}}$	Object-based $E_{\mathrm{T}}^{\mathrm{miss}}$ significance
H_{T}	Transverse momentum sum of all hard objects

Table 15. Summary of input variables for the ANN in the opposite-sign 2ℓ channel.

A Input variables for multivariate discriminants

This appendix describes the input variables for each of the multivariate discriminants utilised by this measurement.

Opposite-sign 2ℓ channel. The input variables for the ANN utilised by the opposite-sign 2ℓ channel — see section 6.1 — are shown in table 15.

3ℓ channel. The input variables for the ANN utilised by the 3ℓ Z-dominated channel — see section 6.3 — are shown in table 16. The transverse mass (eq. 6.1) of the W boson, m_{T}^{W}. It is constructed from the $E_{\mathrm{T}}^{\mathrm{miss}}$ and the lepton not belonging to the SFOS pair with an invariant mass closest to the mass of the Z boson, either ℓ_1 or ℓ_2.

The input variables for the ANN utilised by the 3ℓ Z-depleted channel are shown in table 17. An input deserving additional explanation is the compatibility of the event with the WZ hypothesis, F_{α}. Given the reconstructed charged lepton momenta and the $\vec{p}_{\mathrm{T}}^{\mathrm{miss}}$, the event kinematics can be calculated under the WZ with $Z \to \tau\tau$ hypothesis and using the collinear approximation for the τ-lepton decays with one remaining unknown — for example, the ratio of one τ-lepton's energy to the energy of the lepton from the same τ-lepton's decay. This unknown is varied, and the number of physical kinematic solutions is taken as a measure of the compatibility with the WZ hypothesis.

4ℓ channel. The input variables for the BDTs utilised by the 4ℓ channel — see section 6.4 — are shown in table 18. The azimuthal separation between the leptons from the Higgs boson candidate in the frame where the Higgs boson p_{T} is zero is denoted by $\Delta\phi_{\ell_0\ell_1}^{\mathrm{boost}}$. The Higgs

Variable(s)	Description
$p_{\mathrm{T}}^{\ell_0}$	Transverse momentum of ℓ_0
$\left\lvert\sum_{i=0}^{2}\vec{p}_{\mathrm{T}}^{\,\ell_i}\right\rvert$	Magnitude of the vectorial sum of the lepton transverse momenta
$\lvert\Delta\eta_{\ell_0\ell_1}\rvert$, $\lvert\Delta\eta_{\ell_1\ell_2}\rvert$	Pseudorapidity separation between ℓ_0 and ℓ_1 and between ℓ_1 and ℓ_2
$\Delta\phi_{\ell_0\ell_2}$	Azimuthal separation between ℓ_0 and ℓ_2
$\Delta R_{\ell_0\ell_1}$, $\Delta R_{\ell_0\ell_2}$	Angular separation between ℓ_0 and ℓ_1 and between ℓ_0 and ℓ_2
$m_{\ell_0\ell_1}$, $m_{\ell_0\ell_2}$, $m_{\ell_1\ell_2}$	Dilepton invariant mass for each combination of leptons
$E_{\mathrm{T}}^{\mathrm{miss}}$	Missing transverse momentum
$\Delta\phi_{\ell_0,\mathrm{miss}}$, $\Delta\phi_{\ell_1,\mathrm{miss}}$, $\Delta\phi_{\ell_2,\mathrm{miss}}$	Azimuthal separation between each lepton and the $E_{\mathrm{T}}^{\mathrm{miss}}$
m_{T}^{W}	Transverse mass of the W boson (eq. 6.1)

Table 16. Summary of input variables for the ANN in the 3ℓ Z-dominated channel.

Variable(s)	Description
$p_{\mathrm{T}}^{\ell_0}$, $p_{\mathrm{T}}^{\ell_1}$, $p_{\mathrm{T}}^{\ell_2}$	Transverse momentum for each lepton
$\lvert\Delta\eta_{\ell_0\ell_1}\rvert$, $\lvert\Delta\eta_{\ell_0\ell_2}\rvert$, $\lvert\Delta\eta_{\ell_1\ell_2}\rvert$	Dilepton pseudorapidity separation for each combination of leptons
$\Delta R_{\ell_0\ell_1}$, $\Delta R_{\ell_0\ell_2}$, $\Delta R_{\ell_1\ell_2}$	Dilepton angular separation for each combination of leptons
$m_{\ell_0\ell_1}$, $m_{\ell_0\ell_2}$, $m_{\ell_1\ell_2}$	Dilepton invariant mass for each combination of leptons
$m_{\mathrm{T}}^{\ell_0\ell_1}$, $m_{\mathrm{T}}^{\ell_0\ell_2}$, $m_{\mathrm{T}}^{\ell_1\ell_2}$	Dilepton transverse mass for each combination of leptons
$\left\lvert\sum_{i=0}^{2}\vec{p}_{\mathrm{T}}^{\,\ell_i}\right\rvert$	Magnitude of the vectorial sum of the lepton transverse momenta
$m_{\ell\ell\ell}$	Trilepton invariant mass
n_{jets}	Number of jets
$n_{b\text{-jets}}$	Number of b-tagged jets
$p_{\mathrm{T}}^{j_0}$	Transverse momentum of the leading jet
$E_{\mathrm{T}}^{\mathrm{miss}}$	Missing transverse momentum
$\Delta\phi_{\ell_0,\mathrm{miss}}$, $\Delta\phi_{\ell_1,\mathrm{miss}}$, $\Delta\phi_{\ell_2,\mathrm{miss}}$	Azimuthal separation between each lepton and the $E_{\mathrm{T}}^{\mathrm{miss}}$
$\mathcal{S}_{\mathrm{miss}}/E_{\mathrm{T}}^{\mathrm{miss}}$	Ratio of the $E_{\mathrm{T}}^{\mathrm{miss}}$ significance to the $E_{\mathrm{T}}^{\mathrm{miss}}$
F_{α}	Compatibility of the event with the WZ hypothesis

Table 17. Summary of input variables for the ANN in the 3ℓ Z-depleted channel.

boson transverse momentum is approximated with $\vec{p}_{\mathrm{T}}^{\,H} \approx -\vec{p}_{\mathrm{T}}^{\,Z}$ or $\vec{p}_{\mathrm{T}}^{\,H} \approx -\vec{p}_{\mathrm{T}}^{\,Z} - \sum \vec{p}_{\mathrm{T}}^{\,\mathrm{jet}}$, if at least one jet is in the event.

STXS categorisation. Table 19 shows the input variables for the ANN regressing the W boson's p_{T}. This ANN is utilised by the 3ℓ channels for their differential measurement — see section 6.5.

B Additional plots for the STXS categorisation

This appendix includes additional plots supporting the STXS categorisation scheme described in section 6.5.

Figure 17 shows the Stage 1.2 STXS categorisation scheme for VH production. Figure 18 shows the correlation between p_{T}^{V} and the proxy used for its reconstruction for several channels.

JHEP08(2025)034

Variable(s)	Description
$p_{\mathrm{T}}^{\ell_0}$, $p_{\mathrm{T}}^{\ell_1}$, $p_{\mathrm{T}}^{\ell_2}$, $p_{\mathrm{T}}^{\ell_3}$	Transverse momentum for each lepton
$m_{\ell_0\ell_1}$	Invariant mass of the Higgs boson candidate
$m_{\ell_2\ell_3}$	Invariant mass of the Z candidate
$p_{\mathrm{T}}^{4\ell}$	Transverse momentum of the 4-lepton system
$m_{4\ell}$	Invariant mass of the 4-lepton system
$m_{\tau\tau}$	Invariant mass of the τ-lepton pair using the collinear approximation [133],
	assuming the electrons and muons result from τ-lepton decays
n_{jets}	Number of jets
$E_{\mathrm{T}}^{\mathrm{miss}}$	Missing transverse momentum
$\Delta\phi_{\ell_0\ell_1,\mathrm{miss}}$	Azimuthal separation between the dilepton system composed of ℓ_0 and ℓ_1 and the $E_{\mathrm{T}}^{\mathrm{miss}}$
$\Delta\phi_{\ell_0\ell_1}^{\mathrm{boost}}$	Azimuthal separation between ℓ_0 and ℓ_1 in the Higgs boson candidate's frame

Table 18. Summary of input variables for the BDTs in the 4ℓ channel.

Variable(s)	Description
$p_{\mathrm{T}}^{\ell_0}$, $p_{\mathrm{T}}^{\ell_1}$, $p_{\mathrm{T}}^{\ell_2}$	Transverse momentum for each lepton
$\Delta R_{\ell_0\ell_1}$, $\Delta R_{\ell_0\ell_2}$, $\Delta R_{\ell_1\ell_2}$	Dilepton angular separation for each combination of leptons
$m_{\ell_0\ell_1}$, $m_{\ell_0\ell_2}$, $m_{\ell_1\ell_2}$	Dilepton invariant mass for each combination of leptons
$m_{\mathrm{T}}^{\ell_0\ell_1}$, $m_{\mathrm{T}}^{\ell_0\ell_2}$, $m_{\mathrm{T}}^{\ell_1\ell_2}$	Dilepton transverse mass for each combination of leptons
$\sum_{i=0}^{2} p_{\mathrm{T}}^{\ell_i}$	Scalar sum of the lepton transverse momenta
$E_{\mathrm{T}}^{\mathrm{miss}}$	Missing transverse momentum
$\Delta\phi_{\ell_0,\mathrm{miss}}$, $\Delta\phi_{\ell_1,\mathrm{miss}}$, $\Delta\phi_{\ell_2,\mathrm{miss}}$	Azimuthal separation between each lepton and the $E_{\mathrm{T}}^{\mathrm{miss}}$

Table 19. Summary of input variables for the regression ANN in the 3ℓ channel.

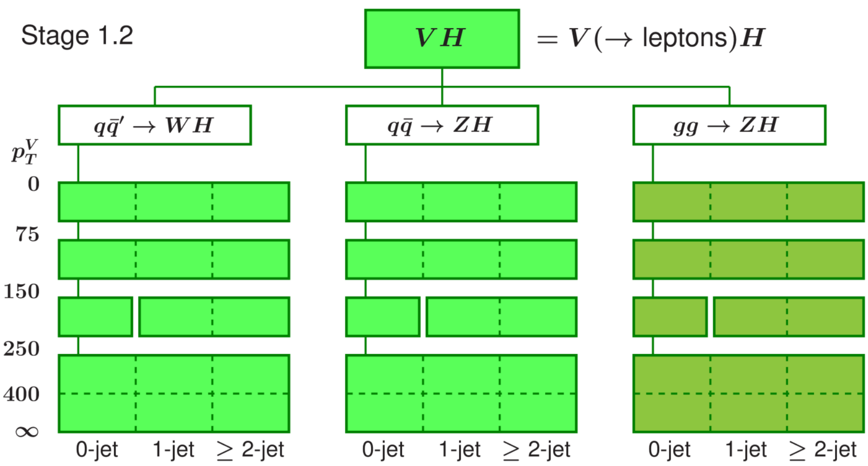

Figure 17. The Stage 1.2 STXS categorisation scheme for VH production [22].

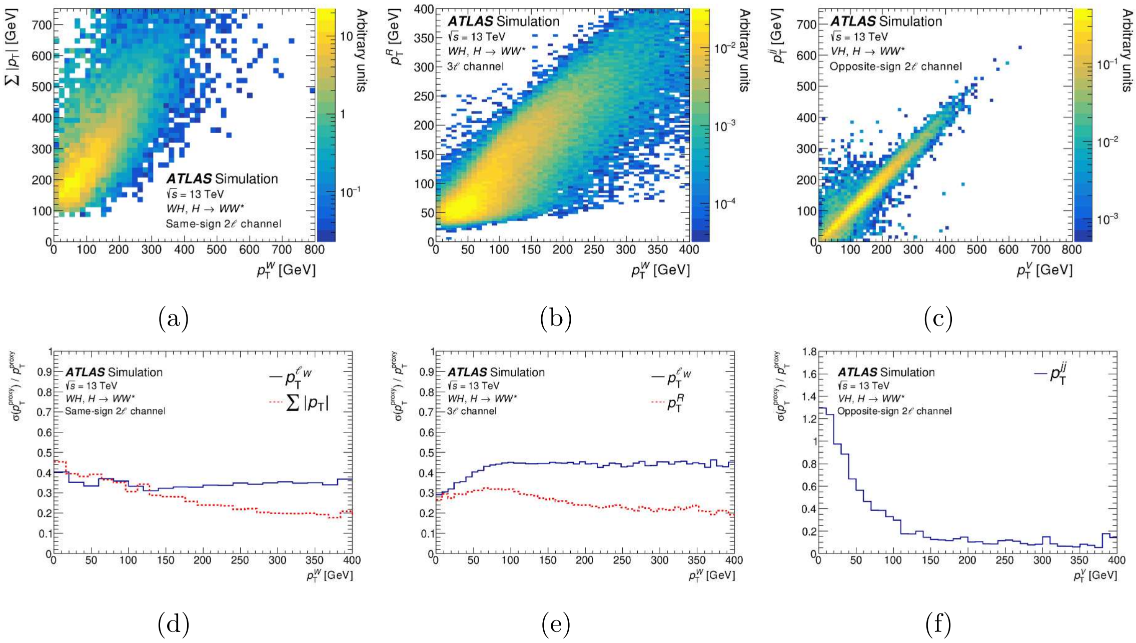

Figure 18. Performance of the p_{T}^{V} proxies for several channels: (a), (b), (c) the correlation between the p_{T} of the associated boson and the proxy and (d), (e), (f) the fractional resolution of the proxy as a function of p_{T}^{V}. Shown are (a), (d) the $\sum |p_{\mathrm{T}}|$ of all objects in the SS2e channel, (b), (e) the regression neural network output, p_{T}^{R}, in the 3ℓ Z-dominated channel, and (c), (f) the dijet p_{T}, p_{T}^{jj}, in the opposite-sign 2ℓ channel. The p_{T}^{R} resolution is compared with that obtained using as a proxy the p_{T} of the lepton identified as that from the W boson decay, while the $\sum |p_{\mathrm{T}}|$ resolution is compared with that obtained using as a proxy the highest p_{T} lepton.

C Breakdown of uncertainties contributing to observed results

This appendix includes tables which show the breakdown of uncertainties contributing to the observed results presented in section 9.2.

Tables 20 and 21 show the fractional contributions from statistical and systematic sources to the total uncertainties in the observed values of the differential cross-sections, presented in section 9.2.2.

JHEP08(2025)034

	$\frac{\Delta_i\,(\sigma_{VH}\,(X\leq p_{\mathrm{T}}^{V}<Y)\times\mathcal{B}_{H\to WW^*})}{\Delta\,(\sigma_{VH}(X\leq p_{\mathrm{T}}^{V}<Y)\times\mathcal{B}_{H\to WW^*})}$ [%], $[X,Y)$: $X \leq p_{\mathrm{T}}^{V} < Y$ GeV			
Source	$VH\,[0,75)$	$VH\,[75,150)$	$VH\,[150,250)$	$VH\,[250,\infty)$
Statistical uncertainties in data	95	95	87	81
Statistical uncertainties in SR data	92	93	87	81
Statistical uncertainties in CR data	22	18	5.9	5.7
Systematic uncertainties	33	32	49	44
Statistical uncertainties in simulation	20	22	24	33
Experimental systematic uncertainties	17	13	13	10
Electrons	3.8	1.6	1.5	1.2
Muons	6.6	3.8	6.6	4.9
Jet energy scale	4.0	2.9	6.5	5.6
Jet energy resolution	7.1	5.7	7.4	5.1
Flavour tagging	1.3	1.4	1.7	1.6
Missing transverse momentum	5.1	1.6	1.2	0.9
Pile-up	4.4	1.2	0.8	0.6
Luminosity	3.1	2.5	1.3	1.1
Mis-identified leptons	9.2	9.0	4.4	3.7
Charge-flip electrons	2.1	2.2	4.0	3.1
Theoretical uncertainties	16	16	21	11
WH	0.6	0.7	1.1	0.6
ZH	0.6	0.7	1.2	0.6
STXS bin migration	2.1	4.2	3.2	1.7
Other H	0.6	1.3	7.7	7.3
WW	1.2	4.4	12.1	2.2
WZ 0-jet	2.5	5.3	5.0	4.0
WZ $\geq$1-jets	2.2	3.1	3.6	2.5
ZZ	14	11	6.3	2.0
VVV	4.5	2.8	4.5	2.7
Top	2.3	8.4	4.8	5.0
Z+jets	0.6	3.0	1.8	2.9
RNN shape uncertainty for WZ	1.1	8.0	36	7.7
Total relative uncertainty (non-fractional)	40	41	170	1000

Table 20. Breakdown of the average contributions to the total uncertainties in the differential cross-sections measured in the p_{T}^{V} scheme. The uncertainties of a single source, Δ_i, are expressed in percentage of the total uncertainty, Δ. Indentation is used to denote subcategories. Also shown is the total relative (non-fractional) uncertainty in the cross-section, $\Delta\,(\sigma \times \mathcal{B}_{H\to WW^*})/(\sigma \times \mathcal{B}_{H\to WW^*})$, in percent. The quadrature sum of the individual sources may differ from the total uncertainty due to correlations.

JHEP08(2025)034

Source	$\frac{\Delta_i\,(\sigma_{\text{STXS category}}\times\mathcal{B}_{H\to WW^*})}{\Delta\,(\sigma_{\text{STXS category}}\times\mathcal{B}_{H\to WW^*})}$ [%], $[X,Y)$: $X \leq (p_{\text{T}}^{V}$ or $m_{jj}) < Y$ GeV						
	$\ell\nu H\,[0,75)$	$\ell\nu H\,[75,150)$	$\ell\nu H\,[150,\infty)$	$\ell\ell H\,[0,75)$	$\ell\ell H\,[75,150)$	$\ell\ell H\,[150,\infty)$	$qqH\,[60,120)$
Statistical uncertainties in data	93	95	83	94	95	96	82
Statistical uncertainties in SR data	90	94	83	92	94	95	82
Statistical uncertainties in CR data	23	15	8.1	14	12	7.6	5.7
Systematic uncertainties	36	32	56	35	32	30	57
Statistical uncertainties in simulation	22	24	18	31	28	20	28
Experimental systematic uncertainties	23	18	11	8.7	8.3	20	23
Electrons	2.6	1.2	1.6	3.6	2.0	0.9	2.1
Muons	2.6	1.7	2.0	3.1	2.5	19	2.4
Jet energy scale	4.8	3.7	2.4	1.7	2.2	1.3	20
Jet energy resolution	11	9.4	2.2	1.9	1.0	0.8	10
Flavour tagging	0.9	1.5	2.3	0.8	1.3	1.2	3.5
Missing transverse momentum	3.4	1.9	0.9	4.0	1.7	1.2	1.1
Pile-up	3.2	1.1	0.4	1.4	1.1	0.3	0.8
Luminosity	1.2	0.9	1.3	2.3	2.3	0.9	2.0
Mis-identified leptons	18	13	7.3	4.2	6.2	4.2	7.1
Charge-flip electrons	3.8	4.2	6.3	0.9	0.8	0.1	1.3
Theoretical uncertainties	12	12	19	15	13	11	44
WH	0.5	0.8	0.7	0.9	0.8	<0.1	0.7
ZH	0.3	0.3	0.5	1.0	0.7	0.3	0.7
STXS bin migration	1.6	2.5	2.0	2.5	3.6	4.7	1.0
Other H	0.3	0.3	0.5	0.9	0.8	<0.1	14.2
WW	0.6	3.7	0.7	0.9	0.8	0.1	19
WZ 0-jet	5.7	6.8	11	1.1	0.9	0.4	0.7
WZ ≥1-jets	3.8	6.2	9.5	1.0	0.8	0.5	1.9
ZZ	3.9	1.8	2.7	14	12	9.6	0.6
VVV	8.4	2.2	10	1.8	0.8	1.1	0.6
Top	2.1	1.3	0.7	1.0	0.8	0.5	32
Z+jets	0.7	0.9	0.5	0.9	0.8	<0.1	4.5
RNN shape uncertainty for WZ	2.2	6.9	49	0.9	0.9	0.9	0.6
Total relative uncertainty (non-fractional)	19 000	88	140	40	47	140	93

Table 21. Breakdown of the average contributions to the total uncertainties in the differential cross-sections measured in the STXS scheme. The uncertainties of a single source, Δ_i, are expressed in percentage of the total uncertainty, Δ. Indentation is used to denote subcategories. Also shown is the total relative (non-fractional) uncertainty in the cross-section, $\Delta\,(\sigma \times \mathcal{B}_{H\to WW^*})/(\sigma \times \mathcal{B}_{H\to WW^*})$, in percent. The quadrature sum of the individual sources may differ from the total uncertainty due to correlations.

Data Availability Statement. The public release of data supporting the findings of this article will follow the CERN Open Data Policy [144]. The values of relevant plots and tables associated with this article are stored in HEPData (https://www.hepdata.net/record/157861).

Code Availability Statement. The ATLAS Collaboration's Athena software, including the configuration of the event generators, is open source (http://gitlab.cern.ch/atlas/athena).

References

[1] T.D. Lee, *A theory of spontaneous T violation*, *Phys. Rev. D* **8** (1973) 1226 [INSPIRE].

[2] G.C. Branco et al., *Theory and phenomenology of two-Higgs-doublet models*, *Phys. Rept.* **516** (2012) 1 [arXiv:1106.0034] [INSPIRE].

[3] J. de Blas, J.M. Lizana and M. Pérez-Victoria, *Combining searches of Z' and W' bosons*, *JHEP* **01** (2013) 166 [arXiv:1211.2229] [INSPIRE].

[4] D. Pappadopulo, A. Thamm, R. Torre and A. Wulzer, *Heavy vector triplets: bridging theory and data*, *JHEP* **09** (2014) 060 [arXiv:1402.4431] [INSPIRE].

[5] ATLAS collaboration, *The ATLAS experiment at the CERN Large Hadron Collider*, 2008 *JINST* **3** S08003 [INSPIRE].

[6] L. Evans and P. Bryant, *LHC machine*, 2008 *JINST* **3** S08001 [INSPIRE].

[7] ATLAS collaboration, *Study of $(W/Z)H$ production and Higgs boson couplings using $H \to WW^*$ decays with the ATLAS detector*, *JHEP* **08** (2015) 137 [arXiv:1506.06641] [INSPIRE].

[8] CMS collaboration, *Measurement of Higgs boson production and properties in the WW decay channel with leptonic final states*, *JHEP* **01** (2014) 096 [arXiv:1312.1129] [INSPIRE].

[9] CMS collaboration, *Measurements of the Higgs boson production cross section and couplings in the W boson pair decay channel in proton-proton collisions at $\sqrt{s} = 13$ TeV*, *Eur. Phys. J. C* **83** (2023) 667 [arXiv:2206.09466] [INSPIRE].

[10] ATLAS collaboration, *Measurement of the production cross section for a Higgs boson in association with a vector boson in the $H \to WW^* \to \ell\nu\ell\nu$ channel in pp collisions at $\sqrt{s} = 13$ TeV with the ATLAS detector*, *Phys. Lett. B* **798** (2019) 134949 [arXiv:1903.10052] [INSPIRE].

[11] ATLAS collaboration, *Measurements of Higgs boson production by gluon-gluon fusion and vector-boson fusion using $H \to WW^* \to e\nu\mu\nu$ decays in pp collisions at $\sqrt{s} = 13$ TeV with the ATLAS detector*, *Phys. Rev. D* **108** (2023) 032005 [arXiv:2207.00338] [INSPIRE].

[12] ATLAS collaboration, *Higgs boson production cross-section measurements and their EFT interpretation in the 4ℓ decay channel at $\sqrt{s} = 13$ TeV with the ATLAS detector*, *Eur. Phys. J. C* **80** (2020) 957 [*Erratum ibid.* **81** (2021) 29] [arXiv:2004.03447] [INSPIRE].

[13] CMS collaboration, *Measurements of production cross sections of the Higgs boson in the four-lepton final state in proton–proton collisions at $\sqrt{s} = 13$ TeV*, *Eur. Phys. J. C* **81** (2021) 488 [arXiv:2103.04956] [INSPIRE].

[14] ATLAS collaboration, *Measurement of the properties of Higgs boson production at $\sqrt{s} = 13$ TeV in the $H \to \gamma\gamma$ channel using 139 fb^{-1} of pp collision data with the ATLAS experiment*, *JHEP* **07** (2023) 088 [arXiv:2207.00348] [INSPIRE].

[15] CMS collaboration, *Measurements of Higgs boson production cross sections and couplings in the diphoton decay channel at $\sqrt{s} = 13$ TeV*, *JHEP* **07** (2021) 027 [arXiv:2103.06956] [INSPIRE].

[16] ATLAS collaboration, *Measurements of WH and ZH production in the $H \to b\bar{b}$ decay channel in pp collisions at 13 TeV with the ATLAS detector*, *Eur. Phys. J. C* **81** (2021) 178 [arXiv:2007.02873] [INSPIRE].

[17] CMS collaboration, *Observation of Higgs boson decay to bottom quarks*, *Phys. Rev. Lett.* **121** (2018) 121801 [arXiv:1808.08242] [INSPIRE].

JHEP08(2025)034

[18] ATLAS collaboration, *Measurements of Higgs boson production cross-sections in the $H \to \tau^+\tau^-$ decay channel in pp collisions at $\sqrt{s} = 13$ TeV with the ATLAS detector*, JHEP **08** (2022) 175 [arXiv:2201.08269] [INSPIRE].

[19] CMS collaboration, *Measurements of Higgs boson production in the decay channel with a pair of τ leptons in proton–proton collisions at $\sqrt{s} = 13$ TeV*, Eur. Phys. J. C **83** (2023) 562 [arXiv:2204.12957] [INSPIRE].

[20] J.R. Andersen et al., *Les Houches 2015: physics at TeV colliders Standard Model working group report*, in the proceedings of the *9th Les Houches workshop on physics at TeV colliders*, (2016) [arXiv:1605.04692] [INSPIRE].

[21] LHC Higgs Cross Section Working Group collaboration, *Handbook of LHC Higgs cross sections: 4. Deciphering the nature of the Higgs sector*, CERN Yellow Rep. Monogr. **2** (2017) 1 [arXiv:1610.07922] [INSPIRE].

[22] N. Berger et al., *Simplified template cross sections — stage 1.1 and 1.2*, arXiv:1906.02754 [INSPIRE].

[23] F. Chollet et al., *Keras*, https://keras.io (2015).

[24] M. Abadi et al., *TensorFlow: a system for large-scale machine learning*, arXiv:1605.08695 [INSPIRE].

[25] A. Hoecker et al., *TMVA — toolkit for multivariate data analysis*, physics/0703039.

[26] ATLAS collaboration, *ATLAS Insertable B-Layer technical design report*, CERN-LHCC-2010-013, CERN, Geneva, Switzerland (2010).

[27] ATLAS IBL collaboration, *Production and integration of the ATLAS Insertable B-Layer*, 2018 JINST **13** T05008 [arXiv:1803.00844] [INSPIRE].

[28] ATLAS collaboration, *Performance of the ATLAS trigger system in 2015*, Eur. Phys. J. C **77** (2017) 317 [arXiv:1611.09661] [INSPIRE].

[29] ATLAS collaboration, *ATLAS data quality operations and performance for 2015–2018 data-taking*, 2020 JINST **15** P04003 [arXiv:1911.04632] [INSPIRE].

[30] ATLAS collaboration, *Luminosity determination in pp collisions at $\sqrt{s} = 13$ TeV using the ATLAS detector at the LHC*, Eur. Phys. J. C **83** (2023) 982 [arXiv:2212.09379] [INSPIRE].

[31] ATLAS collaboration, *Software and computing for run 3 of the ATLAS experiment at the LHC*, Eur. Phys. J. C **85** (2025) 234 [arXiv:2404.06335] [INSPIRE].

[32] ATLAS and CMS collaborations, *Combined measurement of the Higgs boson mass in pp collisions at $\sqrt{s} = 7$ and 8 TeV with the ATLAS and CMS experiments*, Phys. Rev. Lett. **114** (2015) 191803 [arXiv:1503.07589] [INSPIRE].

[33] A. Djouadi, J. Kalinowski and M. Spira, *HDECAY: a program for Higgs boson decays in the Standard Model and its supersymmetric extension*, Comput. Phys. Commun. **108** (1998) 56 [hep-ph/9704448] [INSPIRE].

[34] M. Spira, *QCD effects in Higgs physics*, Fortsch. Phys. **46** (1998) 203 [hep-ph/9705337] [INSPIRE].

[35] A. Djouadi, M.M. Mühlleitner and M. Spira, *Decays of supersymmetric particles: the program SUSY-HIT (SUspect-SdecaY-Hdecay-InTerface)*, Acta Phys. Polon. B **38** (2007) 635 [hep-ph/0609292] [INSPIRE].

[36] A. Bredenstein, A. Denner, S. Dittmaier and M.M. Weber, *Radiative corrections to the semileptonic and hadronic Higgs-boson decays $H \to WW/ZZ \to 4$ fermions*, JHEP **02** (2007) 080 [hep-ph/0611234] [INSPIRE].

[37] A. Bredenstein, A. Denner, S. Dittmaier and M.M. Weber, *Precise predictions for the Higgs-boson decay $H \to WW/ZZ \to 4$ leptons*, Phys. Rev. D **74** (2006) 013004 [hep-ph/0604011] [INSPIRE].

[38] A. Bredenstein, A. Denner, S. Dittmaier and M.M. Weber, *Precision calculations for the Higgs decays $H \to ZZ/WW \to 4$ leptons*, Nucl. Phys. B Proc. Suppl. **160** (2006) 131 [hep-ph/0607060] [INSPIRE].

[39] J. Butterworth et al., *PDF4LHC recommendations for LHC run II*, J. Phys. G **43** (2016) 023001 [arXiv:1510.03865] [INSPIRE].

[40] T. Sjöstrand et al., *An introduction to PYTHIA 8.2*, Comput. Phys. Commun. **191** (2015) 159 [arXiv:1410.3012] [INSPIRE].

[41] ATLAS collaboration, *Measurement of the Z/γ^* boson transverse momentum distribution in pp collisions at $\sqrt{s} = 7$ TeV with the ATLAS detector*, JHEP **09** (2014) 145 [arXiv:1406.3660] [INSPIRE].

[42] ATLAS collaboration, *ATLAS Pythia 8 tunes to 7 TeV data*, ATL-PHYS-PUB-2014-021, CERN, Geneva, Switzerland (2014).

[43] D.J. Lange, *The EvtGen particle decay simulation package*, Nucl. Instrum. Meth. A **462** (2001) 152 [INSPIRE].

[44] P. Nason, *A new method for combining NLO QCD with shower Monte Carlo algorithms*, JHEP **11** (2004) 040 [hep-ph/0409146] [INSPIRE].

[45] S. Frixione, P. Nason and C. Oleari, *Matching NLO QCD computations with parton shower simulations: the POWHEG method*, JHEP **11** (2007) 070 [arXiv:0709.2092] [INSPIRE].

[46] P. Nason and C. Oleari, *NLO Higgs boson production via vector-boson fusion matched with shower in POWHEG*, JHEP **02** (2010) 037 [arXiv:0911.5299] [INSPIRE].

[47] S. Alioli, P. Nason, C. Oleari and E. Re, *A general framework for implementing NLO calculations in shower Monte Carlo programs: the POWHEG BOX*, JHEP **06** (2010) 043 [arXiv:1002.2581] [INSPIRE].

[48] G. Luisoni, P. Nason, C. Oleari and F. Tramontano, *$HW^{\pm}/HZ + 0$ and 1 jet at NLO with the POWHEG BOX interfaced to GoSam and their merging within MiNLO*, JHEP **10** (2013) 083 [arXiv:1306.2542] [INSPIRE].

[49] M.L. Ciccolini, S. Dittmaier and M. Krämer, *Electroweak radiative corrections to associated WH and ZH production at hadron colliders*, Phys. Rev. D **68** (2003) 073003 [hep-ph/0306234] [INSPIRE].

[50] O. Brein, A. Djouadi and R. Harlander, *NNLO QCD corrections to the Higgs-strahlung processes at hadron colliders*, Phys. Lett. B **579** (2004) 149 [hep-ph/0307206] [INSPIRE].

[51] O. Brein, R. Harlander, M. Wiesemann and T. Zirke, *Top-quark mediated effects in hadronic Higgs-strahlung*, Eur. Phys. J. C **72** (2012) 1868 [arXiv:1111.0761] [INSPIRE].

[52] O. Brein, R.V. Harlander and T.J.E. Zirke, *vh@nnlo — Higgs-strahlung at hadron colliders*, Comput. Phys. Commun. **184** (2013) 998 [arXiv:1210.5347] [INSPIRE].

[53] A. Denner, S. Dittmaier, S. Kallweit and A. Mück, *HAWK 2.0: a Monte Carlo program for Higgs production in vector-boson fusion and Higgs-strahlung at hadron colliders*, Comput. Phys. Commun. **195** (2015) 161 [arXiv:1412.5390] [INSPIRE].

[54] L. Altenkamp et al., *Gluon-induced Higgs-strahlung at next-to-leading order QCD*, JHEP **02** (2013) 078 [arXiv:1211.5015] [INSPIRE].

[55] R.V. Harlander, A. Kulesza, V. Theeuwes and T. Zirke, *Soft gluon resummation for gluon-induced Higgs-strahlung*, JHEP **11** (2014) 082 [arXiv:1410.0217] [INSPIRE].

[56] K. Hamilton, P. Nason, E. Re and G. Zanderighi, *NNLOPS simulation of Higgs boson production*, JHEP **10** (2013) 222 [arXiv:1309.0017] [INSPIRE].

[57] K. Hamilton, P. Nason and G. Zanderighi, *MINLO: Multi-scale Improved NLO*, JHEP **10** (2012) 155 [arXiv:1206.3572] [INSPIRE].

[58] J.M. Campbell et al., *NLO Higgs boson production plus one and two jets using the POWHEG BOX, MadGraph4 and MCFM*, JHEP **07** (2012) 092 [arXiv:1202.5475] [INSPIRE].

[59] K. Hamilton, P. Nason, C. Oleari and G. Zanderighi, *Merging $H/W/Z + 0$ and 1 jet at NLO with no merging scale: a path to parton shower + NNLO matching*, JHEP **05** (2013) 082 [arXiv:1212.4504] [INSPIRE].

[60] S. Catani and M. Grazzini, *An NNLO subtraction formalism in hadron collisions and its application to Higgs boson production at the LHC*, Phys. Rev. Lett. **98** (2007) 222002 [hep-ph/0703012] [INSPIRE].

[61] S. Actis, G. Passarino, C. Sturm and S. Uccirati, *NLO electroweak corrections to Higgs boson production at hadron colliders*, Phys. Lett. B **670** (2008) 12 [arXiv:0809.1301] [INSPIRE].

[62] S. Actis, G. Passarino, C. Sturm and S. Uccirati, *NNLO computational techniques: the cases $H \to \gamma\gamma$ and $H \to gg$*, Nucl. Phys. B **811** (2009) 182 [arXiv:0809.3667] [INSPIRE].

[63] R.V. Harlander and K.J. Ozeren, *Top mass effects in Higgs production at next-to-next-to-leading order QCD: virtual corrections*, Phys. Lett. B **679** (2009) 467 [arXiv:0907.2997] [INSPIRE].

[64] R.V. Harlander and K.J. Ozeren, *Finite top mass effects for hadronic Higgs production at next-to-next-to-leading order*, JHEP **11** (2009) 088 [arXiv:0909.3420] [INSPIRE].

[65] A. Pak, M. Rogal and M. Steinhauser, *Finite top quark mass effects in NNLO Higgs boson production at LHC*, JHEP **02** (2010) 025 [arXiv:0911.4662] [INSPIRE].

[66] R.V. Harlander, H. Mantler, S. Marzani and K.J. Ozeren, *Higgs production in gluon fusion at next-to-next-to-leading order QCD for finite top mass*, Eur. Phys. J. C **66** (2010) 359 [arXiv:0912.2104] [INSPIRE].

[67] C. Anastasiou et al., *Higgs boson gluon-fusion production in QCD at three loops*, Phys. Rev. Lett. **114** (2015) 212001 [arXiv:1503.06056] [INSPIRE].

[68] C. Anastasiou et al., *High precision determination of the gluon fusion Higgs boson cross-section at the LHC*, JHEP **05** (2016) 058 [arXiv:1602.00695] [INSPIRE].

[69] M. Bonetti, K. Melnikov and L. Tancredi, *Higher order corrections to mixed QCD-EW contributions to Higgs boson production in gluon fusion*, Phys. Rev. D **97** (2018) 056017 [*Erratum ibid.* **97** (2018) 099906] [arXiv:1801.10403] [INSPIRE].

[70] F. Dulat, A. Lazopoulos and B. Mistlberger, *iHixs 2 — inclusive Higgs cross sections*, Comput. Phys. Commun. **233** (2018) 243 [arXiv:1802.00827] [INSPIRE].

[71] M. Ciccolini, A. Denner and S. Dittmaier, *Strong and electroweak corrections to the production of Higgs + 2 jets via weak interactions at the LHC*, *Phys. Rev. Lett.* **99** (2007) 161803 [arXiv:0707.0381] [INSPIRE].

[72] M. Ciccolini, A. Denner and S. Dittmaier, *Electroweak and QCD corrections to Higgs production via vector-boson fusion at the LHC*, *Phys. Rev. D* **77** (2008) 013002 [arXiv:0710.4749] [INSPIRE].

[73] P. Bolzoni, F. Maltoni, S.-O. Moch and M. Zaro, *Higgs production via vector-boson fusion at NNLO in QCD*, *Phys. Rev. Lett.* **105** (2010) 011801 [arXiv:1003.4451] [INSPIRE].

[74] S. Frixione, P. Nason and G. Ridolfi, *A positive-weight next-to-leading-order Monte Carlo for heavy flavour hadroproduction*, *JHEP* **09** (2007) 126 [arXiv:0707.3088] [INSPIRE].

[75] H.B. Hartanto, B. Jäger, L. Reina and D. Wackeroth, *Higgs boson production in association with top quarks in the POWHEG BOX*, *Phys. Rev. D* **91** (2015) 094003 [arXiv:1501.04498] [INSPIRE].

[76] SHERPA collaboration, *Event generation with Sherpa 2.2*, *SciPost Phys.* **7** (2019) 034 [arXiv:1905.09127] [INSPIRE].

[77] T. Gleisberg and S. Höche, *Comix, a new matrix element generator*, *JHEP* **12** (2008) 039 [arXiv:0808.3674] [INSPIRE].

[78] F. Cascioli, P. Maierhöfer and S. Pozzorini, *Scattering amplitudes with OpenLoops*, *Phys. Rev. Lett.* **108** (2012) 111601 [arXiv:1111.5206] [INSPIRE].

[79] A. Denner, S. Dittmaier and L. Hofer, *Collier: a fortran-based Complex One-Loop LIbrary in Extended Regularizations*, *Comput. Phys. Commun.* **212** (2017) 220 [arXiv:1604.06792] [INSPIRE].

[80] F. Buccioni et al., *OpenLoops 2*, *Eur. Phys. J. C* **79** (2019) 866 [arXiv:1907.13071] [INSPIRE].

[81] C. Anastasiou, L.J. Dixon, K. Melnikov and F. Petriello, *High precision QCD at hadron colliders: electroweak gauge boson rapidity distributions at NNLO*, *Phys. Rev. D* **69** (2004) 094008 [hep-ph/0312266] [INSPIRE].

[82] F. Buccioni, S. Pozzorini and M. Zoller, *On-the-fly reduction of open loops*, *Eur. Phys. J. C* **78** (2018) 70 [arXiv:1710.11452] [INSPIRE].

[83] F. Caola, K. Melnikov, R. Röntsch and L. Tancredi, *QCD corrections to W^+W^- production through gluon fusion*, *Phys. Lett. B* **754** (2016) 275 [arXiv:1511.08617] [INSPIRE].

[84] M. Grazzini, S. Kallweit, M. Wiesemann and J.Y. Yook, *ZZ production at the LHC: NLO QCD corrections to the loop-induced gluon fusion channel*, *JHEP* **03** (2019) 070 [arXiv:1811.09593] [INSPIRE].

[85] NNPDF collaboration, *Parton distributions for the LHC run II*, *JHEP* **04** (2015) 040 [arXiv:1410.8849] [INSPIRE].

[86] S. Schumann and F. Krauss, *A parton shower algorithm based on Catani-Seymour dipole factorisation*, *JHEP* **03** (2008) 038 [arXiv:0709.1027] [INSPIRE].

[87] S. Catani, F. Krauss, R. Kuhn and B.R. Webber, *QCD matrix elements + parton showers*, *JHEP* **11** (2001) 063 [hep-ph/0109231] [INSPIRE].

[88] S. Höche, F. Krauss, S. Schumann and F. Siegert, *QCD matrix elements and truncated showers*, *JHEP* **05** (2009) 053 [arXiv:0903.1219] [INSPIRE].

[89] S. Höche, F. Krauss, M. Schönherr and F. Siegert, *A critical appraisal of NLO+PS matching methods*, *JHEP* **09** (2012) 049 [arXiv:1111.1220] [INSPIRE].

JHEP08(2025)034

[90] S. Höche, F. Krauss, M. Schönherr and F. Siegert, *QCD matrix elements + parton showers: the NLO case*, *JHEP* **04** (2013) 027 [arXiv:1207.5030] [INSPIRE].

[91] J. Alwall et al., *The automated computation of tree-level and next-to-leading order differential cross sections, and their matching to parton shower simulations*, *JHEP* **07** (2014) 079 [arXiv:1405.0301] [INSPIRE].

[92] ATLAS collaboration, *Studies on top-quark Monte Carlo modelling for Top2016*, ATL-PHYS-PUB-2016-020, CERN, Geneva, Switzerland (2016).

[93] M. Beneke, P. Falgari, S. Klein and C. Schwinn, *Hadronic top-quark pair production with NNLL threshold resummation*, *Nucl. Phys. B* **855** (2012) 695 [arXiv:1109.1536] [INSPIRE].

[94] M. Cacciari et al., *Top-pair production at hadron colliders with next-to-next-to-leading logarithmic soft-gluon resummation*, *Phys. Lett. B* **710** (2012) 612 [arXiv:1111.5869] [INSPIRE].

[95] P. Bärnreuther, M. Czakon and A. Mitov, *Percent level precision physics at the Tevatron: first genuine NNLO QCD corrections to $q\bar{q} \to t\bar{t} + X$*, *Phys. Rev. Lett.* **109** (2012) 132001 [arXiv:1204.5201] [INSPIRE].

[96] M. Czakon and A. Mitov, *NNLO corrections to top-pair production at hadron colliders: the all-fermionic scattering channels*, *JHEP* **12** (2012) 054 [arXiv:1207.0236] [INSPIRE].

[97] M. Czakon and A. Mitov, *NNLO corrections to top pair production at hadron colliders: the quark-gluon reaction*, *JHEP* **01** (2013) 080 [arXiv:1210.6832] [INSPIRE].

[98] M. Czakon, P. Fiedler and A. Mitov, *Total top-quark pair-production cross section at hadron colliders through $O(\alpha_S^4)$*, *Phys. Rev. Lett.* **110** (2013) 252004 [arXiv:1303.6254] [INSPIRE].

[99] M. Czakon and A. Mitov, *Top++: a program for the calculation of the top-pair cross-section at hadron colliders*, *Comput. Phys. Commun.* **185** (2014) 2930 [arXiv:1112.5675] [INSPIRE].

[100] E. Re, *Single-top Wt-channel production matched with parton showers using the POWHEG method*, *Eur. Phys. J. C* **71** (2011) 1547 [arXiv:1009.2450] [INSPIRE].

[101] S. Frixione et al., *Single-top hadroproduction in association with a W boson*, *JHEP* **07** (2008) 029 [arXiv:0805.3067] [INSPIRE].

[102] GEANT4 collaboration, *GEANT4 — a simulation toolkit*, *Nucl. Instrum. Meth. A* **506** (2003) 250 [INSPIRE].

[103] ATLAS collaboration, *The ATLAS simulation infrastructure*, *Eur. Phys. J. C* **70** (2010) 823 [arXiv:1005.4568] [INSPIRE].

[104] ATLAS collaboration, *Software and computing for run 3 of the ATLAS experiment at the LHC*, *Eur. Phys. J. C* **85** (2025) 234 [arXiv:2404.06335] [INSPIRE].

[105] T. Sjöstrand, S. Mrenna and P.Z. Skands, *A brief introduction to PYTHIA 8.1*, *Comput. Phys. Commun.* **178** (2008) 852 [arXiv:0710.3820] [INSPIRE].

[106] R.D. Ball et al., *Parton distributions with LHC data*, *Nucl. Phys. B* **867** (2013) 244 [arXiv:1207.1303] [INSPIRE].

[107] ATLAS collaboration, *The Pythia 8 A3 tune description of ATLAS minimum bias and inelastic measurements incorporating the Donnachie-Landshoff diffractive model*, ATL-PHYS-PUB-2016-017, CERN, Geneva, Switzerland (2016).

[108] M. Bähr et al., *Herwig++ physics and manual*, *Eur. Phys. J. C* **58** (2008) 639 [arXiv:0803.0883] [INSPIRE].

[109] J. Bellm et al., *Herwig 7.0/Herwig++ 3.0 release note*, *Eur. Phys. J. C* **76** (2016) 196 [arXiv:1512.01178] [INSPIRE].

[110] F. Cascioli et al., *Precise Higgs-background predictions: merging NLO QCD and squared quark-loop corrections to four-lepton + 0,1 jet production*, *JHEP* **01** (2014) 046 [arXiv:1309.0500] [INSPIRE].

[111] T. Binoth, G. Ossola, C.G. Papadopoulos and R. Pittau, *NLO QCD corrections to tri-boson production*, *JHEP* **06** (2008) 082 [arXiv:0804.0350] [INSPIRE].

[112] N. Kidonakis, *Two-loop soft anomalous dimensions for single top quark associated production with a W^- or H^-*, *Phys. Rev. D* **82** (2010) 054018 [arXiv:1005.4451] [INSPIRE].

[113] N. Kidonakis, *Top quark production*, in the proceedings of the *Helmholtz international Summer school on physics of heavy quarks and hadrons*, (2014) [DOI:10.3204/DESY-PROC-2013-03/Kidonakis] [arXiv:1311.0283] [INSPIRE].

[114] A. Broggio et al., *Top-quark pair hadroproduction in association with a heavy boson at NLO+NNLL including EW corrections*, *JHEP* **08** (2019) 039 [arXiv:1907.04343] [INSPIRE].

[115] J. Campbell, R.K. Ellis and R. Röntsch, *Single top production in association with a Z boson at the LHC*, *Phys. Rev. D* **87** (2013) 114006 [arXiv:1302.3856] [INSPIRE].

[116] F. Maltoni, L. Mantani and K. Mimasu, *Top-quark electroweak interactions at high energy*, *JHEP* **10** (2019) 004 [arXiv:1904.05637] [INSPIRE].

[117] ATLAS collaboration, *Performance of electron and photon triggers in ATLAS during LHC run 2*, *Eur. Phys. J. C* **80** (2020) 47 [arXiv:1909.00761] [INSPIRE].

[118] ATLAS collaboration, *Performance of the ATLAS muon triggers in run 2*, 2020 *JINST* **15** P09015 [arXiv:2004.13447] [INSPIRE].

[119] ATLAS collaboration, *Vertex reconstruction performance of the ATLAS detector at $\sqrt{s} = 13$ TeV*, ATL-PHYS-PUB-2015-026, CERN, Geneva, Switzerland (2015).

[120] ATLAS collaboration, *Electron and photon efficiencies in LHC run 2 with the ATLAS experiment*, *JHEP* **05** (2024) 162 [arXiv:2308.13362] [INSPIRE].

[121] ATLAS collaboration, *Muon reconstruction and identification efficiency in ATLAS using the full run 2 pp collision data set at $\sqrt{s} = 13$ TeV*, *Eur. Phys. J. C* **81** (2021) 578 [arXiv:2012.00578] [INSPIRE].

[122] ATLAS collaboration, *Electron and photon performance measurements with the ATLAS detector using the 2015–2017 LHC proton-proton collision data*, 2019 *JINST* **14** P12006 [arXiv:1908.00005] [INSPIRE].

[123] M. Cacciari, G.P. Salam and G. Soyez, *The anti-k_t jet clustering algorithm*, *JHEP* **04** (2008) 063 [arXiv:0802.1189] [INSPIRE].

[124] M. Cacciari, G.P. Salam and G. Soyez, *FastJet user manual*, *Eur. Phys. J. C* **72** (2012) 1896 [arXiv:1111.6097] [INSPIRE].

[125] ATLAS collaboration, *Jet reconstruction and performance using particle flow with the ATLAS detector*, *Eur. Phys. J. C* **77** (2017) 466 [arXiv:1703.10485] [INSPIRE].

[126] ATLAS collaboration, *Jet energy scale and resolution measured in proton–proton collisions at $\sqrt{s} = 13$ TeV with the ATLAS detector*, *Eur. Phys. J. C* **81** (2021) 689 [arXiv:2007.02645] [INSPIRE].

JHEP08(2025)034

[127] ATLAS collaboration, *Performance of pile-up mitigation techniques for jets in pp collisions at* $\sqrt{s} = 8$ *TeV using the ATLAS detector*, Eur. Phys. J. C **76** (2016) 581 [arXiv:1510.03823] [INSPIRE].

[128] ATLAS collaboration, *Identification and rejection of pile-up jets at high pseudorapidity with the ATLAS detector*, Eur. Phys. J. C **77** (2017) 580 [*Erratum ibid.* **77** (2017) 712] [arXiv:1705.02211] [INSPIRE].

[129] ATLAS collaboration, *Forward jet vertex tagging using the particle flow algorithm*, ATL-PHYS-PUB-2019-026, CERN, Geneva, Switzerland (2019).

[130] ATLAS collaboration, *ATLAS flavour-tagging algorithms for the LHC run 2 pp collision dataset*, Eur. Phys. J. C **83** (2023) 681 [arXiv:2211.16345] [INSPIRE].

[131] ATLAS collaboration, *ATLAS b-jet identification performance and efficiency measurement with* $t\bar{t}$ *events in pp collisions at* $\sqrt{s} = 13$ *TeV*, Eur. Phys. J. C **79** (2019) 970 [arXiv:1907.05120] [INSPIRE].

[132] ATLAS collaboration, *The performance of missing transverse momentum reconstruction and its significance with the ATLAS detector using* $140\,fb^{-1}$ *of* $\sqrt{s} = 13$ *TeV pp collisions*, Eur. Phys. J. C **85** (2025) 606 [arXiv:2402.05858] [INSPIRE].

[133] T. Plehn, D.L. Rainwater and D. Zeppenfeld, *A method for identifying* $H \to \tau^+\tau^- \to e^\pm\mu^\mp p_T$ *at the CERN LHC*, Phys. Rev. D **61** (2000) 093005 [hep-ph/9911385] [INSPIRE].

[134] ATLAS collaboration, *Measurement and interpretation of same-sign W boson pair production in association with two jets in pp collisions at* $\sqrt{s} = 13$ *TeV with the ATLAS detector*, JHEP **04** (2024) 026 [arXiv:2312.00420] [INSPIRE].

[135] S. Hochreiter and J. Schmidhuber, *Long short-term memory*, Neural Comput. **9** (1997) 1735 [INSPIRE].

[136] ATLAS collaboration, *Observation of WWW production in pp collisions at* $\sqrt{s} = 13$ *TeV with the ATLAS detector*, Phys. Rev. Lett. **129** (2022) 061803 [arXiv:2201.13045] [INSPIRE].

[137] ATLAS collaboration, *Electron and photon energy calibration with the ATLAS detector using LHC run 2 data*, 2024 JINST **19** P02009 [arXiv:2309.05471] [INSPIRE].

[138] ATLAS collaboration, *Studies of the muon momentum calibration and performance of the ATLAS detector with pp collisions at* $\sqrt{s} = 13$ *TeV*, Eur. Phys. J. C **83** (2023) 686 [arXiv:2212.07338] [INSPIRE].

[139] G. Avoni et al., *The new LUCID-2 detector for luminosity measurement and monitoring in ATLAS*, 2018 JINST **13** P07017 [INSPIRE].

[140] S. Höche, S. Schumann and F. Siegert, *Hard photon production and matrix-element parton-shower merging*, Phys. Rev. D **81** (2010) 034026 [arXiv:0912.3501] [INSPIRE].

[141] ATLAS collaboration, *Evaluation of theoretical uncertainties for simplified template cross section measurements of V-associated production of the Higgs boson*, ATL-PHYS-PUB-2018-035, CERN, Geneva, Switzerland (2018).

[142] G. Cowan, K. Cranmer, E. Gross and O. Vitells, *Asymptotic formulae for likelihood-based tests of new physics*, Eur. Phys. J. C **71** (2011) 1554 [*Erratum ibid.* **73** (2013) 2501] [arXiv:1007.1727] [INSPIRE].

[143] ATLAS collaboration, *ATLAS computing acknowledgements*, ATL-SOFT-PUB-2025-001, CERN, Geneva, Switzerland (2025).

[144] CERN, *CERN open data policy for the LHC experiments*, CERN-OPEN-2020-013, CERN, Geneva, Switzerland (2020) [DOI:10.17181/CERN.QXNK.8L2G].

JHEP08(2025)034

The ATLAS collaboration

G. Aad[105], E. Aakvaag[17], B. Abbott[124], S. Abdelhameed[120a], K. Abeling[57], N.J. Abicht[51], S.H. Abidi[30], M. Aboelela[46], A. Aboulhorma[36e], H. Abramowicz[156], H. Abreu[155], Y. Abulaiti[121], B.S. Acharya[71a,71b,l], A. Ackermann[65a], C. Adam Bourdarios[4], L. Adamczyk[88a], S.V. Addepalli[27], M.J. Addison[104], J. Adelman[119], A. Adiguzel[22c], T. Adye[138], A.A. Affolder[140], Y. Afik[41], M.N. Agaras[13], J. Agarwala[75a,75b], A. Aggarwal[103], C. Agheorghiesei[28c], F. Ahmadov[40,aa], W.S. Ahmed[107], S. Ahuja[98], X. Ai[64e], G. Aielli[78a,78b], A. Aikot[168], M. Ait Tamlihat[36e], B. Aitbenchikh[36a], M. Akbiyik[103], T.P.A. Åkesson[101], A.V. Akimov[150], D. Akiyama[173], N.N. Akolkar[25], S. Aktas[22a], K. Al Khoury[43], G.L. Alberghi[24b], J. Albert[170], P. Albicocco[55], G.L. Albouy[62], S. Alderweireldt[54], Z.L. Alegria[125], M. Aleksa[37], I.N. Aleksandrov[40], C. Alexa[28b], T. Alexopoulos[10], F. Alfonsi[24b], M. Algren[58], M. Alhroob[172], B. Ali[136], H.M.J. Ali[94,t], S. Ali[32], S.W. Alibocus[95], M. Aliev[34c], G. Alimonti[73a], W. Alkakhi[57], C. Allaire[68], B.M.M. Allbrooke[151], J.S. Allen[104], J.F. Allen[54], C.A. Allendes Flores[141f], P.P. Allport[21], A. Aloisio[74a,74b], F. Alonso[93], C. Alpigiani[143], Z.M.K. Alsolami[94], M. Alvarez Estevez[102], A. Alvarez Fernandez[103], M. Alves Cardoso[58], M.G. Alviggi[74a,74b], M. Aly[104], Y. Amaral Coutinho[85b], A. Ambler[107], C. Amelung[37], M. Amerl[104], C.G. Ames[112], D. Amidei[109], B. Amini[56], K. Amirie[159], S.P. Amor Dos Santos[134a], K.R. Amos[168], D. Amperiadou[157], S. An[86], V. Ananiev[129], C. Anastopoulos[144], T. Andeen[11], J.K. Anders[37], A.C. Anderson[61], S.Y. Andrean[49a,49b], A. Andreazza[73a,73b], S. Angelidakis[9], A. Angerami[43], A.V. Anisenkov[39], A. Annovi[76a], C. Antel[58], E. Antipov[150], M. Antonelli[55], F. Anulli[77a], M. Aoki[86], T. Aoki[158], M.A. Aparo[151], L. Aperio Bella[50], C. Appelt[156], A. Apyan[27], S.J. Arbiol Val[89], C. Arcangeletti[55], A.T.H. Arce[53], J-F. Arguin[111], S. Argyropoulos[157], J.-H. Arling[50], O. Arnaez[4], H. Arnold[150], G. Artoni[77a,77b], H. Asada[114], K. Asai[122], S. Asai[158], N.A. Asbah[37], R.A. Ashby Pickering[172], K. Assamagan[30], R. Astalos[29a], K.S.V. Astrand[101], S. Atashi[163], R.J. Atkin[34a], M. Atkinson[167], H. Atmani[36f], P.A. Atmasiddha[132], K. Augsten[136], S. Auricchio[74a,74b], A.D. Auriol[21], V.A. Austrup[104], G. Avolio[37], K. Axiotis[58], G. Azuelos[111,af], D. Babal[29b], H. Bachacou[139], K. Bachas[157,p], A. Bachiu[35], E. Bachmann[52], F. Backman[49a,49b], A. Badea[41], T.M. Baer[109], P. Bagnaia[77a,77b], M. Bahmani[19], D. Bahner[56], K. Bai[127], J.T. Baines[138], L. Baines[97], O.K. Baker[177], E. Bakos[16], D. Bakshi Gupta[8], L.E. Balabram Filho[85b], V. Balakrishnan[124], R. Balasubramanian[4], E.M. Baldin[39], P. Balek[88a], E. Ballabene[24b,24a], F. Balli[139], L.M. Baltes[65a], W.K. Balunas[33], J. Balz[103], I. Bamwidhi[120b], E. Banas[89], M. Bandieramonte[133], A. Bandyopadhyay[25], S. Bansal[25], L. Barak[156], M. Barakat[50], E.L. Barberio[108], D. Barberis[59b,59a], M. Barbero[105], M.Z. Barel[118], T. Barillari[113], M-S. Barisits[37], T. Barklow[148], P. Baron[126], D.A. Baron Moreno[104], A. Baroncelli[64a], A.J. Barr[130], J.D. Barr[99], F. Barreiro[102], J. Barreiro Guimarães da Costa[14], U. Barron[156], M.G. Barros Teixeira[134a], S. Barsov[39], F. Bartels[65a], R. Bartoldus[148], A.E. Barton[94], P. Bartos[29a], A. Basan[103], M. Baselga[51], A. Bassalat[68,b], M.J. Basso[160a], S. Bataju[46], R. Bate[169], R.L. Bates[61], S. Batlamous[102], B. Batool[146], M. Battaglia[140], D. Battulga[19], M. Bauce[77a,77b], M. Bauer[81], P. Bauer[25], L.T. Bazzano Hurrell[31], J.B. Beacham[53], T. Beau[131], J.Y. Beaucamp[93], P.H. Beauchemin[162], P. Bechtle[25], H.P. Beck[20,o],

JHEP08(2025)034

K. Becker[172], A.J. Beddall[84], V.A. Bednyakov[40], C.P. Bee[150], L.J. Beemster[16], T.A. Beermann[37], M. Begalli[85d], M. Begel[30], A. Behera[150], J.K. Behr[50], J.F. Beirer[37], F. Beisiegel[25], M. Belfkir[120b], G. Bella[156], L. Bellagamba[24b], A. Bellerive[35], P. Bellos[21], K. Beloborodov[39], D. Benchekroun[36a], F. Bendebba[36a], Y. Benhammou[156], K.C. Benkendorfer[63], L. Beresford[50], M. Beretta[55], E. Bergeaas Kuutmann[166], N. Berger[4], B. Bergmann[136], J. Beringer[18a], G. Bernardi[5], C. Bernius[148], F.U. Bernlochner[25], F. Bernon[37], A. Berrocal Guardia[13], T. Berry[98], P. Berta[137], A. Berthold[52], S. Bethke[113], A. Betti[77a,77b], A.J. Bevan[97], N.K. Bhalla[56], S. Bhatta[150], D.S. Bhattacharya[171], P. Bhattarai[148], Z.M. Bhatti[121], K.D. Bhide[56], V.S. Bhopatkar[125], R.M. Bianchi[133], G. Bianco[24b,24a], O. Biebel[112], R. Bielski[127], M. Biglietti[79a], C.S. Billingsley[46], Y. Bimgdi[36f], M. Bindi[57], A. Bingham[176], A. Bingul[22b], C. Bini[77a,77b], G.A. Bird[33], M. Birman[174], M. Biros[137], S. Biryukov[151], T. Bisanz[51], E. Bisceglie[45b,45a], J.P. Biswal[138], D. Biswas[146], I. Bloch[50], A. Blue[61], U. Blumenschein[97], J. Blumenthal[103], V.S. Bobrovnikov[39], M. Boehler[56], B. Boehm[171], D. Bogavac[37], A.G. Bogdanchikov[39], L.S. Boggia[131], C. Bohm[49a], V. Boisvert[98], P. Bokan[37], T. Bold[88a], M. Bomben[5], M. Bona[97], M. Boonekamp[139], C.D. Booth[98], A.G. Borbély[61], I.S. Bordulev[39], G. Borissov[94], D. Bortoletto[130], D. Boscherini[24b], M. Bosman[13], J.D. Bossio Sola[37], K. Bouaouda[36a], N. Bouchhar[168], L. Boudet[4], J. Boudreau[133], E.V. Bouhova-Thacker[94], D. Boumediene[42], R. Bouquet[59b,59a], A. Boveia[123], J. Boyd[37], D. Boye[30], I.R. Boyko[40], L. Bozianu[58], J. Bracinik[21], N. Brahimi[4], G. Brandt[176], O. Brandt[33], F. Braren[50], B. Brau[106], J.E. Brau[127], R. Brener[174], L. Brenner[118], R. Brenner[166], S. Bressler[174], G. Brianti[80a,80b], D. Britton[61], D. Britzger[113], I. Brock[25], R. Brock[110], G. Brooijmans[43], A.J. Brooks[70], E.M. Brooks[160b], E. Brost[30], L.M. Brown[170,160a], L.E. Bruce[63], T.L. Bruckler[130], P.A. Bruckman de Renstrom[89], B. Brüers[50], A. Bruni[24b], G. Bruni[24b], M. Bruschi[24b], N. Bruscino[77a,77b], T. Buanes[17], Q. Buat[143], D. Buchin[113], A.G. Buckley[61], O. Bulekov[39], B.A. Bullard[148], S. Burdin[95], C.D. Burgard[51], A.M. Burger[37], B. Burghgrave[8], O. Burlayenko[56], J. Burleson[167], J.T.P. Burr[33], J.C. Burzynski[147], E.L. Busch[43], V. Büscher[103], P.J. Bussey[61], J.M. Butler[26], C.M. Buttar[61], J.M. Butterworth[99], W. Buttinger[138], C.J. Buxo Vazquez[110], A.R. Buzykaev[39], S. Cabrera Urbán[168], L. Cadamuro[68], D. Caforio[60], H. Cai[133], Y. Cai[14,115c], Y. Cai[115a], V.M.M. Cairo[37], O. Cakir[3a], N. Calace[37], P. Calafiura[18a], G. Calderini[131], P. Calfayan[35], G. Callea[61], L.P. Caloba[85b], D. Calvet[42], S. Calvet[42], M. Calvetti[76a,76b], R. Camacho Toro[131], S. Camarda[37], D. Camarero Munoz[27], P. Camarri[78a,78b], M.T. Camerlingo[74a,74b], D. Cameron[37], C. Camincher[170], M. Campanelli[99], A. Camplani[44], V. Canale[74a,74b], A.C. Canbay[3a], E. Canonero[98], J. Cantero[168], Y. Cao[167], F. Capocasa[27], M. Capua[45b,45a], A. Carbone[73a,73b], R. Cardarelli[78a], J.C.J. Cardenas[8], G. Carducci[45b,45a], T. Carli[37], G. Carlino[74a], J.I. Carlotto[13], B.T. Carlson[133,q], E.M. Carlson[170,160a], J. Carmignani[95], L. Carminati[73a,73b], A. Carnelli[139], M. Carnesale[37], S. Caron[117], E. Carquin[141f], I.B. Carr[108], S. Carrá[73a], G. Carratta[24b,24a], A.M. Carroll[127], M.P. Casado[13,i], M. Caspar[50], F.L. Castillo[4], L. Castillo Garcia[13], V. Castillo Gimenez[168], N.F. Castro[134a,134e], A. Catinaccio[37], J.R. Catmore[129], T. Cavaliere[4], V. Cavaliere[30], N. Cavalli[24b,24a], L.J. Caviedes Betancourt[23b], Y.C. Cekmecelioglu[50], E. Celebi[84],

JHEP08(2025)034

S. Cella[37], M.S. Centonze[72a,72b], V. Cepaitis[58], K. Cerny[126], A.S. Cerqueira[85a], A. Cerri[151], L. Cerrito[78a,78b], F. Cerutti[18a], B. Cervato[146], A. Cervelli[24b], G. Cesarini[55], S.A. Cetin[84], D. Chakraborty[119], J. Chan[18a], W.Y. Chan[158], J.D. Chapman[33], E. Chapon[139], B. Chargeishvili[154b], D.G. Charlton[21], M. Chatterjee[20], C. Chauhan[137], Y. Che[115a], S. Chekanov[6], S.V. Chekulaev[160a], G.A. Chelkov[40,a], A. Chen[109], B. Chen[156], B. Chen[170], H. Chen[115a], H. Chen[30], J. Chen[64c], J. Chen[147], M. Chen[130], S. Chen[90], S.J. Chen[115a], X. Chen[64c], X. Chen[15,ae], Y. Chen[64a], C.L. Cheng[175], H.C. Cheng[66a], S. Cheong[148], A. Cheplakov[40], E. Cheremushkina[50], E. Cherepanova[118], R. Cherkaoui El Moursli[36e], E. Cheu[7], K. Cheung[67], L. Chevalier[139], V. Chiarella[55], G. Chiarelli[76a], N. Chiedde[105], G. Chiodini[72a], A.S. Chisholm[21], A. Chitan[28b], M. Chitishvili[168], M.V. Chizhov[40,r], K. Choi[11], Y. Chou[143], E.Y.S. Chow[117], K.L. Chu[174], M.C. Chu[66a], X. Chu[14,115c], Z. Chubinidze[55], J. Chudoba[135], J.J. Chwastowski[89], D. Cieri[113], K.M. Ciesla[88a], V. Cindro[96], A. Ciocio[18a], F. Cirotto[74a,74b], Z.H. Citron[174], M. Citterio[73a], D.A. Ciubotaru[28b], A. Clark[58], P.J. Clark[54], N. Clarke Hall[99], C. Clarry[159], J.M. Clavijo Columbie[50], S.E. Clawson[50], C. Clement[49a,49b], Y. Coadou[105], M. Cobal[71a,71c], A. Coccaro[59b], R.F. Coelho Barrue[134a], R. Coelho Lopes De Sa[106], S. Coelli[73a], L.S. Colangeli[159], B. Cole[43], J. Collot[62], P. Conde Muiño[134a,134g], M.P. Connell[34c], S.H. Connell[34c], E.I. Conroy[130], F. Conventi[74a,ag], H.G. Cooke[21], A.M. Cooper-Sarkar[130], F.A. Corchia[24b,24a], A. Cordeiro Oudot Choi[131], L.D. Corpe[42], M. Corradi[77a,77b], F. Corriveau[107,y], A. Cortes-Gonzalez[19], M.J. Costa[168], F. Costanza[4], D. Costanzo[144], B.M. Cote[123], J. Couthures[4], G. Cowan[98], K. Cranmer[175], L. Cremer[51], D. Cremonini[24b,24a], S. Crépé-Renaudin[62], F. Crescioli[131], M. Cristinziani[146], M. Cristoforetti[80a,80b], V. Croft[118], J.E. Crosby[125], G. Crosetti[45b,45a], A. Cueto[102], H. Cui[99], Z. Cui[7], W.R. Cunningham[61], F. Curcio[168], J.R. Curran[54], P. Czodrowski[37], M.J. Da Cunha Sargedas De Sousa[59b,59a], J.V. Da Fonseca Pinto[85b], C. Da Via[104], W. Dabrowski[88a], T. Dado[37], S. Dahbi[153], T. Dai[109], D. Dal Santo[20], C. Dallapiccola[106], M. Dam[44], G. D'amen[30], V. D'Amico[112], J. Damp[103], J.R. Dandoy[35], D. Dannheim[37], M. Danninger[147], V. Dao[150], G. Darbo[59b], S.J. Das[30], F. Dattola[50], S. D'Auria[73a,73b], A. D'Avanzo[74a,74b], C. David[34a], T. Davidek[137], I. Dawson[97], H.A. Day-hall[136], K. De[8], R. De Asmundis[74a], N. De Biase[50], S. De Castro[24b,24a], N. De Groot[117], P. de Jong[118], H. De la Torre[119], A. De Maria[115a], A. De Salvo[77a], U. De Sanctis[78a,78b], F. De Santis[72a,72b], A. De Santo[151], J.B. De Vivie De Regie[62], J. Debevc[96], D.V. Dedovich[40], J. Degens[95], A.M. Deiana[46], F. Del Corso[24b,24a], J. Del Peso[102], L. Delagrange[131], F. Deliot[139], C.M. Delitzsch[51], M. Della Pietra[74a,74b], D. Della Volpe[58], A. Dell'Acqua[37], L. Dell'Asta[73a,73b], M. Delmastro[4], C.C. Delogu[103], P.A. Delsart[62], S. Demers[177], M. Demichev[40], S.P. Denisov[39], L. D'Eramo[42], D. Derendarz[89], F. Derue[131], P. Dervan[95], K. Desch[25], C. Deutsch[25], F.A. Di Bello[59b,59a], A. Di Ciaccio[78a,78b], L. Di Ciaccio[4], A. Di Domenico[77a,77b], C. Di Donato[74a,74b], A. Di Girolamo[37], G. Di Gregorio[37], A. Di Luca[80a,80b], B. Di Micco[79a,79b], R. Di Nardo[79a,79b], K.F. Di Petrillo[41], M. Diamantopoulou[35], F.A. Dias[118], T. Dias Do Vale[147], M.A. Diaz[141a,141b], F.G. Diaz Capriles[25], A.R. Didenko[40], M. Didenko[168], E.B. Diehl[109], S. Díez Cornell[50], C. Diez Pardos[146], C. Dimitriadi[166], A. Dimitrievska[21], J. Dingfelder[25],

T. Dingley[130], I-M. Dinu[28b], S.J. Dittmeier[65b], F. Dittus[37], M. Divisek[137], B. Dixit[95], F. Djama[105], T. Djobava[154b], C. Doglioni[104,101], A. Dohnalova[29a], J. Dolejsi[137], Z. Dolezal[137], K. Domijan[88a], K.M. Dona[41], M. Donadelli[85d], B. Dong[110], J. Donini[42], A. D'Onofrio[74a,74b], M. D'Onofrio[95], J. Dopke[138], A. Doria[74a], N. Dos Santos Fernandes[134a], P. Dougan[104], M.T. Dova[93], A.T. Doyle[61], M.A. Draguet[130], M.P. Drescher[57], E. Dreyer[174], I. Drivas-koulouris[10], M. Drnevich[121], M. Drozdova[58], D. Du[64a], T.A. du Pree[118], F. Dubinin[39], M. Dubovsky[29a], E. Duchovni[174], G. Duckeck[112], O.A. Ducu[28b], D. Duda[54], A. Dudarev[37], E.R. Duden[27], M. D'uffizi[104], L. Duflot[68], M. Dührssen[37], I. Duminica[28g], A.E. Dumitriu[28b], M. Dunford[65a], S. Dungs[51], K. Dunne[49a,49b], A. Duperrin[105], H. Duran Yildiz[3a], M. Düren[60], A. Durglishvili[154b], D. Duvnjak[35], B.L. Dwyer[119], G.I. Dyckes[18a], M. Dyndal[88a], B.S. Dziedzic[37], Z.O. Earnshaw[151], G.H. Eberwein[130], B. Eckerova[29a], S. Eggebrecht[57], E. Egidio Purcino De Souza[85e], L.F. Ehrke[58], G. Eigen[17], K. Einsweiler[18a], T. Ekelof[166], P.A. Ekman[101], S. El Farkh[36b], Y. El Ghazali[64a], H. El Jarrari[37], A. El Moussaouy[36a], V. Ellajosyula[166], M. Ellert[166], F. Ellinghaus[176], N. Ellis[37], J. Elmsheuser[30], M. Elsawy[120a], M. Elsing[37], D. Emeliyanov[138], Y. Enari[86], I. Ene[18a], S. Epari[13], P.A. Erland[89], D. Ernani Martins Neto[89], M. Errenst[176], M. Escalier[68], C. Escobar[168], E. Etzion[156], G. Evans[134a,134b], H. Evans[70], L.S. Evans[98], A. Ezhilov[39], S. Ezzarqtouni[36a], F. Fabbri[24b,24a], L. Fabbri[24b,24a], G. Facini[99], V. Fadeyev[140], R.M. Fakhrutdinov[39], D. Fakoudis[103], S. Falciano[77a], L.F. Falda Ulhoa Coelho[37], F. Fallavollita[113], G. Falsetti[45b,45a], J. Faltova[137], C. Fan[167], K.Y. Fan[66b], Y. Fan[14], Y. Fang[14,115c], M. Fanti[73a,73b], M. Faraj[71a,71b], Z. Farazpay[100], A. Farbin[8], A. Farilla[79a], T. Farooque[110], S.M. Farrington[138,54], F. Fassi[36e], D. Fassouliotis[9], M. Faucci Giannelli[78a,78b], W.J. Fawcett[33], L. Fayard[68], P. Federic[137], P. Federicova[135], O.L. Fedin[39,a], M. Feickert[175], L. Feligioni[105], D.E. Fellers[127], C. Feng[64b], Z. Feng[118], M.J. Fenton[163], L. Ferencz[50], R.A.M. Ferguson[94], S.I. Fernandez Luengo[141f], P. Fernandez Martinez[69], M.J.V. Fernoux[105], J. Ferrando[94], A. Ferrari[166], P. Ferrari[118,117], R. Ferrari[75a], D. Ferrere[58], C. Ferretti[109], D. Fiacco[77a,77b], F. Fiedler[103], P. Fiedler[136], S. Filimonov[39], A. Filipčič[96], E.K. Filmer[160a], F. Filthaut[117], M.C.N. Fiolhais[134a,134c,c], L. Fiorini[168], W.C. Fisher[110], T. Fitschen[104], P.M. Fitzhugh[139], I. Fleck[146], P. Fleischmann[109], T. Flick[176], M. Flores[34d,ac], L.R. Flores Castillo[66a], L. Flores Sanz De Acedo[37], F.M. Follega[80a,80b], N. Fomin[33], J.H. Foo[159], A. Formica[139], A.C. Forti[104], E. Fortin[37], A.W. Fortman[18a], M.G. Foti[18a], L. Fountas[9,j], D. Fournier[68], H. Fox[94], P. Francavilla[76a,76b], S. Francescato[63], S. Franchellucci[58], M. Franchini[24b,24a], S. Franchino[65a], D. Francis[37], L. Franco[117], V. Franco Lima[37], L. Franconi[50], M. Franklin[63], G. Frattari[27], Y.Y. Frid[156], J. Friend[61], N. Fritzsche[37], A. Froch[56], D. Froidevaux[37], J.A. Frost[130], Y. Fu[64a], S. Fuenzalida Garrido[141f], M. Fujimoto[105], K.Y. Fung[66a], E. Furtado De Simas Filho[85e], M. Furukawa[158], J. Fuster[168], A. Gaa[57], A. Gabrielli[24b,24a], A. Gabrielli[159], P. Gadow[37], G. Gagliardi[59b,59a], L.G. Gagnon[18a], S. Gaid[165], S. Galantzan[156], J. Gallagher[1], E.J. Gallas[130], B.J. Gallop[138], K.K. Gan[123], S. Ganguly[158], Y. Gao[54], F.M. Garay Walls[141a,141b], B. Garcia[30], C. García[168], A. Garcia Alonso[118], A.G. Garcia Caffaro[177], J.E. García Navarro[168], M. Garcia-Sciveres[18a], G.L. Gardner[132], R.W. Gardner[41], N. Garelli[162], D. Garg[82], R.B. Garg[148],

JHEP08(2025)034

J.M. Gargan[54], C.A. Garner[159], C.M. Garvey[34a], V.K. Gassmann[162], G. Gaudio[75a], V. Gautam[13], P. Gauzzi[77a,77b], J. Gavranovic[96], I.L. Gavrilenko[39], A. Gavrilyuk[39], C. Gay[169], G. Gaycken[127], E.N. Gazis[10], A.A. Geanta[28b], C.M. Gee[140], A. Gekow[123], C. Gemme[59b], M.H. Genest[62], A.D. Gentry[116], S. George[98], W.F. George[21], T. Geralis[48], P. Gessinger-Befurt[37], M.E. Geyik[176], M. Ghani[172], K. Ghorbanian[97], A. Ghosal[146], A. Ghosh[163], A. Ghosh[7], B. Giacobbe[24b], S. Giagu[77a,77b], T. Giani[118], A. Giannini[64a], S.M. Gibson[98], M. Gignac[140], D.T. Gil[88b], A.K. Gilbert[88a], B.J. Gilbert[43], D. Gillberg[35], G. Gilles[118], L. Ginabat[131], D.M. Gingrich[2,af], M.P. Giordani[71a,71c], P.F. Giraud[139], G. Giugliarelli[71a,71c], D. Giugni[73a], F. Giuli[78a,78b], I. Gkialas[9,j], L.K. Gladilin[39], C. Glasman[102], G.R. Gledhill[127], G. Glemža[50], M. Glisic[127], I. Gnesi[45b], Y. Go[30], M. Goblirsch-Kolb[37], B. Gocke[51], D. Godin[111], B. Gokturk[22a], S. Goldfarb[108], T. Golling[58], M.G.D. Gololo[34g], D. Golubkov[39], J.P. Gombas[110], A. Gomes[134a,134b], G. Gomes Da Silva[146], A.J. Gomez Delegido[168], R. Gonçalo[134a], L. Gonella[21], A. Gongadze[154c], F. Gonnella[21], J.L. Gonski[148], R.Y. González Andana[54], S. González de la Hoz[168], R. Gonzalez Lopez[95], C. Gonzalez Renteria[18a], M.V. Gonzalez Rodrigues[50], R. Gonzalez Suarez[166], S. Gonzalez-Sevilla[58], L. Goossens[37], B. Gorini[37], E. Gorini[72a,72b], A. Gorišek[96], T.C. Gosart[132], A.T. Goshaw[53], M.I. Gostkin[40], S. Goswami[125], C.A. Gottardo[37], S.A. Gotz[112], M. Gouighri[36b], V. Goumarre[50], A.G. Goussiou[143], N. Govender[34c], R.P. Grabarczyk[130], I. Grabowska-Bold[88a], K. Graham[35], E. Gramstad[129], S. Grancagnolo[72a,72b], C.M. Grant[1,139], P.M. Gravila[28f], F.G. Gravili[72a,72b], H.M. Gray[18a], M. Greco[72a,72b], M.J. Green[1], C. Grefe[25], A.S. Grefsrud[17], I.M. Gregor[50], K.T. Greif[163], P. Grenier[148], S.G. Grewe[113], A.A. Grillo[140], K. Grimm[32], S. Grinstein[13,u], J.-F. Grivaz[68], E. Gross[174], J. Grosse-Knetter[57], L. Guan[109], J.G.R. Guerrero Rojas[168], G. Guerrieri[37], R. Gugel[103], J.A.M. Guhit[109], A. Guida[19], E. Guilloton[172], S. Guindon[37], F. Guo[14,115c], J. Guo[64c], L. Guo[50], L. Guo[14], Y. Guo[109], A. Gupta[51], R. Gupta[133], S. Gurbuz[25], S.S. Gurdasani[56], G. Gustavino[77a,77b], P. Gutierrez[124], L.F. Gutierrez Zagazeta[132], M. Gutsche[52], C. Gutschow[99], C. Gwenlan[130], C.B. Gwilliam[95], E.S. Haaland[129], A. Haas[121], M. Habedank[61], C. Haber[18a], H.K. Hadavand[8], A. Hadef[52], S. Hadzic[113], A.I. Hagan[94], J.J. Hahn[146], E.H. Haines[99], M. Haleem[171], J. Haley[125], G.D. Hallewell[105], L. Halser[20], K. Hamano[170], M. Hamer[25], E.J. Hampshire[98], J. Han[64b], L. Han[115a], L. Han[64a], S. Han[18a], Y.F. Han[159], K. Hanagaki[86], M. Hance[140], D.A. Hangal[43], H. Hanif[147], M.D. Hank[132], J.B. Hansen[44], P.H. Hansen[44], D. Harada[58], T. Harenberg[176], S. Harkusha[178], M.L. Harris[106], Y.T. Harris[25], J. Harrison[13], N.M. Harrison[123], P.F. Harrison[172], N.M. Hartman[113], N.M. Hartmann[112], R.Z. Hasan[98,138], Y. Hasegawa[145], F. Haslbeck[130], S. Hassan[17], R. Hauser[110], C.M. Hawkes[21], R.J. Hawkings[37], Y. Hayashi[158], D. Hayden[110], C. Hayes[109], R.L. Hayes[118], C.P. Hays[130], J.M. Hays[97], H.S. Hayward[95], F. He[64a], M. He[14,115c], Y. He[50], Y. He[99], N.B. Heatley[97], V. Hedberg[101], A.L. Heggelund[129], N.D. Hehir[97,*], C. Heidegger[56], K.K. Heidegger[56], J. Heilman[35], S. Heim[50], T. Heim[18a], J.G. Heinlein[132], J.J. Heinrich[127], L. Heinrich[113,ad], J. Hejbal[135], A. Held[175], S. Hellesund[17], C.M. Helling[169], S. Hellman[49a,49b], R.C.W. Henderson[94], L. Henkelmann[33], A.M. Henriques Correia[37], H. Herde[101], Y. Hernández Jiménez[150], L.M. Herrmann[25],

JHEP08(2025)034

T. Herrmann[52], G. Herten[56], R. Hertenberger[112], L. Hervas[37], M.E. Hesping[103], N.P. Hessey[160a], J. Hessler[113], M. Hidaoui[36b], N. Hidic[137], E. Hill[159], S.J. Hillier[21], J.R. Hinds[110], F. Hinterkeuser[25], M. Hirose[128], S. Hirose[161], D. Hirschbuehl[176], T.G. Hitchings[104], B. Hiti[96], J. Hobbs[150], R. Hobincu[28e], N. Hod[174], M.C. Hodgkinson[144], B.H. Hodkinson[130], A. Hoecker[37], D.D. Hofer[109], J. Hofer[168], T. Holm[25], M. Holzbock[37], L.B.A.H. Hommels[33], B.P. Honan[104], J.J. Hong[70], J. Hong[64c], T.M. Hong[133], B.H. Hooberman[167], W.H. Hopkins[6], M.C. Hoppesch[167], Y. Horii[114], M.E. Horstmann[113], S. Hou[153], M.R. Housenga[167], A.S. Howard[96], J. Howarth[61], J. Hoya[6], M. Hrabovsky[126], A. Hrynevich[50], T. Hryn'ova[4], P.J. Hsu[67], S.-C. Hsu[143], T. Hsu[68], M. Hu[18a], Q. Hu[64a], S. Huang[33], X. Huang[14,115c], Y. Huang[144], Y. Huang[103], Y. Huang[14], Z. Huang[104], Z. Hubacek[136], M. Huebner[25], F. Huegging[25], T.B. Huffman[130], M. Hufnagel Maranha De Faria[85a], C.A. Hugli[50], M. Huhtinen[37], S.K. Huiberts[17], R. Hulsken[107], N. Huseynov[12,g], J. Huston[110], J. Huth[63], R. Hyneman[148], G. Iacobucci[58], G. Iakovidis[30], L. Iconomidou-Fayard[68], J.P. Iddon[37], P. Iengo[74a,74b], R. Iguchi[158], Y. Iiyama[158], T. Iizawa[130], Y. Ikegami[86], N. Ilic[159], H. Imam[85c], G. Inacio Goncalves[85d], T. Ingebretsen Carlson[49a,49b], J.M. Inglis[97], G. Introzzi[75a,75b], M. Iodice[79a], V. Ippolito[77a,77b], R.K. Irwin[95], M. Ishino[158], W. Islam[175], C. Issever[19], S. Istin[22a,aj], H. Ito[173], R. Iuppa[80a,80b], A. Ivina[174], J.M. Izen[47], V. Izzo[74a], P. Jacka[135], P. Jackson[1], C.S. Jagfeld[112], G. Jain[160a], P. Jain[50], K. Jakobs[56], T. Jakoubek[174], J. Jamieson[61], W. Jang[158], M. Javurkova[106], P. Jawahar[104], L. Jeanty[127], J. Jejelava[154a,ab], P. Jenni[56,f], C.E. Jessiman[35], C. Jia[64b], H. Jia[169], J. Jia[150], X. Jia[14,115c], Z. Jia[115a], C. Jiang[54], S. Jiggins[50], J. Jimenez Pena[13], S. Jin[115a], A. Jinaru[28b], O. Jinnouchi[142], P. Johansson[144], K.A. Johns[7], J.W. Johnson[140], F.A. Jolly[50], D.M. Jones[151], E. Jones[50], K.S. Jones[8], P. Jones[33], R.W.L. Jones[94], T.J. Jones[95], H.L. Joos[57,37], R. Joshi[123], J. Jovicevic[16], X. Ju[18a], J.J. Junggeburth[37], T. Junkermann[65a], A. Juste Rozas[13,u], M.K. Juzek[89], S. Kabana[141e], A. Kaczmarska[89], M. Kado[113], H. Kagan[123], M. Kagan[148], A. Kahn[132], C. Kahra[103], T. Kaji[158], E. Kajomovitz[155], N. Kakati[174], I. Kalaitzidou[56], C.W. Kalderon[30], N.J. Kang[140], D. Kar[34g], K. Karava[130], M.J. Kareem[160b], E. Karentzos[25], O. Karkout[118], S.N. Karpov[40], Z.M. Karpova[40], V. Kartvelishvili[94], A.N. Karyukhin[39], E. Kasimi[157], J. Katzy[50], S. Kaur[35], K. Kawade[145], M.P. Kawale[124], C. Kawamoto[90], T. Kawamoto[64a], E.F. Kay[37], F.I. Kaya[162], S. Kazakos[110], V.F. Kazanin[39], Y. Ke[150], J.M. Keaveney[34a], R. Keeler[170], G.V. Kehris[63], J.S. Keller[35], J.J. Kempster[151], O. Kepka[135], B.P. Kerridge[138], S. Kersten[176], B.P. Kerševan[96], L. Keszeghova[29a], S. Ketabchi Haghighat[159], R.A. Khan[133], A. Khanov[125], A.G. Kharlamov[39], T. Kharlamova[39], E.E. Khoda[143], M. Kholodenko[134a], T.J. Khoo[19], G. Khoriauli[171], J. Khubua[154b,*], Y.A.R. Khwaira[131], B. Kibirige[34g], D. Kim[6], D.W. Kim[49a,49b], Y.K. Kim[41], N. Kimura[99], M.K. Kingston[57], A. Kirchhoff[57], C. Kirfel[25], F. Kirfel[25], J. Kirk[138], A.E. Kiryunin[113], S. Kita[161], C. Kitsaki[10], O. Kivernyk[25], M. Klassen[162], C. Klein[35], L. Klein[171], M.H. Klein[46], S.B. Klein[58], U. Klein[95], A. Klimentov[30], T. Klioutchnikova[37], P. Kluit[118], S. Kluth[113], E. Kneringer[81], T.M. Knight[159], A. Knue[51], M. Kobel[52], D. Kobylianskii[174], S.F. Koch[130], M. Kocian[148], P. Kodyš[137], D.M. Koeck[127], P.T. Koenig[25], T. Koffas[35],

O. Kolay[52], I. Koletsou[4], T. Komarek[89], K. Köneke[56], A.X.Y. Kong[1], T. Kono[122], N. Konstantinidis[99], P. Kontaxakis[58], B. Konya[101], R. Kopeliansky[43], S. Koperny[88a], K. Korcyl[89], K. Kordas[157,e], A. Korn[99], S. Korn[57], I. Korolkov[13], N. Korotkova[39], B. Kortman[118], O. Kortner[113], S. Kortner[113], W.H. Kostecka[119], V.V. Kostyukhin[146], A. Kotsokechagia[37], A. Kotwal[53], A. Koulouris[37], A. Kourkoumeli-Charalampidi[75a,75b], C. Kourkoumelis[9], E. Kourlitis[113], O. Kovanda[127], R. Kowalewski[170], W. Kozanecki[127], A.S. Kozhin[39], V.A. Kramarenko[39], G. Kramberger[96], P. Kramer[25], M.W. Krasny[131], A. Krasznahorkay[37], A.C. Kraus[119], J.W. Kraus[176], J.A. Kremer[50], T. Kresse[52], L. Kretschmann[176], J. Kretzschmar[95], K. Kreul[19], P. Krieger[159], M. Krivos[137], K. Krizka[21], K. Kroeninger[51], H. Kroha[113], J. Kroll[135], J. Kroll[132], K.S. Krowpman[110], U. Kruchonak[40], H. Krüger[25], N. Krumnack[83], M.C. Kruse[53], O. Kuchinskaia[39], S. Kuday[3a], S. Kuehn[37], R. Kuesters[56], T. Kuhl[50], V. Kukhtin[40], Y. Kulchitsky[40], S. Kuleshov[141d,141b], M. Kumar[34g], N. Kumari[50], P. Kumari[160b], A. Kupco[135], T. Kupfer[51], A. Kupich[39], O. Kuprash[56], H. Kurashige[87], L.L. Kurchaninov[160a], O. Kurdysh[68], Y.A. Kurochkin[38], A. Kurova[39], M. Kuze[142], A.K. Kvam[106], J. Kvita[126], T. Kwan[107], N.G. Kyriacou[109], L.A.O. Laatu[105], C. Lacasta[168], F. Lacava[77a,77b], H. Lacker[19], D. Lacour[131], N.N. Lad[99], E. Ladygin[40], A. Lafarge[42], B. Laforge[131], T. Lagouri[177], F.Z. Lahbabi[36a], S. Lai[57], J.E. Lambert[170], S. Lammers[70], W. Lampl[7], C. Lampoudis[157,e], G. Lamprinoudis[103], A.N. Lancaster[119], E. Lançon[30], U. Landgraf[56], M.P.J. Landon[97], V.S. Lang[56], O.K.B. Langrekken[129], A.J. Lankford[163], F. Lanni[37], K. Lantzsch[25], A. Lanza[75a], M. Lanzac Berrocal[168], J.F. Laporte[139], T. Lari[73a], F. Lasagni Manghi[24b], M. Lassnig[37], V. Latonova[135], A. Laurier[155], S.D. Lawlor[144], Z. Lawrence[104], R. Lazaridou[172], M. Lazzaroni[73a,73b], B. Le[104], H.D.M. Le[110], E.M. Le Boulicaut[177], L.T. Le Pottier[18a], B. Leban[24b,24a], A. Lebedev[83], M. LeBlanc[104], F. Ledroit-Guillon[62], S.C. Lee[153], S. Lee[49a,49b], T.F. Lee[95], L.L. Leeuw[34c], H.P. Lefebvre[98], M. Lefebvre[170], C. Leggett[18a], G. Lehmann Miotto[37], M. Leigh[58], W.A. Leight[106], W. Leinonen[117], A. Leisos[157,s], M.A.L. Leite[85c], C.E. Leitgeb[19], R. Leitner[137], K.J.C. Leney[46], T. Lenz[25], S. Leone[76a], C. Leonidopoulos[54], A. Leopold[149], R. Les[110], C.G. Lester[33], M. Levchenko[39], J. Levêque[4], L.J. Levinson[174], G. Levrini[24b,24a], M.P. Lewicki[89], C. Lewis[143], D.J. Lewis[4], L. Lewitt[144], A. Li[30], B. Li[64b], C. Li[64a], C-Q. Li[113], H. Li[64a], H. Li[64b], H. Li[115a], H. Li[15], H. Li[64b], J. Li[64c], K. Li[14], L. Li[64c], M. Li[14,115c], S. Li[14,115c], S. Li[64d,64c,d], T. Li[5], X. Li[107], Z. Li[158], Z. Li[14,115c], Z. Li[64a], S. Liang[14,115c], Z. Liang[14], M. Liberatore[139], B. Liberti[78a], K. Lie[66c], J. Lieber Marin[85e], H. Lien[70], H. Lin[109], K. Lin[110], L. Linden[112], R.E. Lindley[7], J.H. Lindon[2], J. Ling[63], E. Lipeles[132], A. Lipniacka[17], A. Lister[169], J.D. Little[70], B. Liu[14], B.X. Liu[115b], D. Liu[64d,64c], E.H.L. Liu[21], J.B. Liu[64a], J.K.K. Liu[33], K. Liu[64d], K. Liu[64d,64c], M. Liu[64a], M.Y. Liu[64a], P. Liu[14], Q. Liu[64d,143,64c], X. Liu[64a], X. Liu[64b], Y. Liu[115b,115c], Y.L. Liu[64b], Y.W. Liu[64a], S.L. Lloyd[97], E.M. Lobodzinska[50], P. Loch[7], E. Lodhi[159], T. Lohse[19], K. Lohwasser[144], E. Loiacono[50], J.D. Lomas[21], J.D. Long[43], I. Longarini[163], R. Longo[167], I. Lopez Paz[69], A. Lopez Solis[50], N.A. Lopez-canelas[7], N. Lorenzo Martinez[4], A.M. Lory[112], M. Losada[120a], G. Löschcke Centeno[151], O. Loseva[39], X. Lou[49a,49b], X. Lou[14,115c], A. Lounis[68], P.A. Love[94], G. Lu[14,115c], M. Lu[68], S. Lu[132], Y.J. Lu[67], H.J. Lubatti[143],

JHEP08(2025)034

C. Luci[77a,77b], F.L. Lucio Alves[115a], F. Luehring[70], O. Lukianchuk[68], B.S. Lunday[132], O. Lundberg[149], B. Lund-Jensen[149,*], N.A. Luongo[6], M.S. Lutz[37], A.B. Lux[26], D. Lynn[30], R. Lysak[135], E. Lytken[101], V. Lyubushkin[40], T. Lyubushkina[40], M.M. Lyukova[150], M.Firdaus M. Soberi[54], H. Ma[30], K. Ma[64a], L.L. Ma[64b], W. Ma[64a], Y. Ma[125], J.C. MacDonald[103], P.C. Machado De Abreu Farias[85e], R. Madar[42], T. Madula[99], J. Maeda[87], T. Maeno[30], H. Maguire[144], V. Maiboroda[139], A. Maio[134a,134b,134d], K. Maj[88a], O. Majersky[50], S. Majewski[127], N. Makovec[68], V. Maksimovic[16], B. Malaescu[131], Pa. Malecki[89], V.P. Maleev[39], F. Malek[62,n], M. Mali[96], D. Malito[98], U. Mallik[82,*], S. Maltezos[10], S. Malyukov[40], J. Mamuzic[13], G. Mancini[55], M.N. Mancini[27], G. Manco[75a,75b], J.P. Mandalia[97], S.S. Mandarry[151], I. Mandić[96], L. Manhaes de Andrade Filho[85a], I.M. Maniatis[174], J. Manjarres Ramos[92], D.C. Mankad[174], A. Mann[112], S. Manzoni[37], L. Mao[64c], X. Mapekula[34c], A. Marantis[157,s], G. Marchiori[5], M. Marcisovsky[135], C. Marcon[73a], M. Marinescu[21], S. Marium[50], M. Marjanovic[124], A. Markhoos[56], M. Markovitch[68], M.K. Maroun[106], E.J. Marshall[94], Z. Marshall[18a], S. Marti-Garcia[168], J. Martin[99], T.A. Martin[138], V.J. Martin[54], B. Martin dit Latour[17], L. Martinelli[77a,77b], M. Martinez[13,u], P. Martinez Agullo[168], V.I. Martinez Outschoorn[106], P. Martinez Suarez[13], S. Martin-Haugh[138], G. Martinovicova[137], V.S. Martoiu[28b], A.C. Martyniuk[99], A. Marzin[37], D. Mascione[80a,80b], L. Masetti[103], J. Masik[104], A.L. Maslennikov[39], S.L. Mason[43], P. Massarotti[74a,74b], P. Mastrandrea[76a,76b], A. Mastroberardino[45b,45a], T. Masubuchi[128], T.T. Mathew[127], T. Mathisen[166], J. Matousek[137], D.M. Mattern[51], J. Maurer[28b], T. Maurin[61], A.J. Maury[68], B. Maček[96], D.A. Maximov[39], A.E. May[104], R. Mazini[34g], I. Maznas[119], M. Mazza[110], S.M. Mazza[140], E. Mazzeo[73a,73b], C. Mc Ginn[30], J.P. Mc Gowan[170], S.P. Mc Kee[109], C.A. Mc Lean[6], C.C. McCracken[169], E.F. McDonald[108], A.E. McDougall[118], J.A. Mcfayden[151], R.P. McGovern[132], R.P. Mckenzie[34g], T.C. Mclachlan[50], D.J. Mclaughlin[99], S.J. McMahon[138], C.M. Mcpartland[95], R.A. McPherson[170,y], S. Mehlhase[112], A. Mehta[95], D. Melini[168], B.R. Mellado Garcia[34g], A.H. Melo[57], F. Meloni[50], A.M. Mendes Jacques Da Costa[104], H.Y. Meng[159], L. Meng[94], S. Menke[113], M. Mentink[37], E. Meoni[45b,45a], G. Mercado[119], S. Merianos[157], C. Merlassino[71a,71c], L. Merola[74a,74b], C. Meroni[73a,73b], J. Metcalfe[6], A.S. Mete[6], E. Meuser[103], C. Meyer[70], J-P. Meyer[139], R.P. Middleton[138], L. Mijović[54], G. Mikenberg[174], M. Mikestikova[135], M. Mikuž[96], H. Mildner[103], A. Milic[37], D.W. Miller[41], E.H. Miller[148], L.S. Miller[35], A. Milov[174], D.A. Milstead[49a,49b], T. Min[115a], A.A. Minaenko[39], I.A. Minashvili[154b], L. Mince[61], A.I. Mincer[121], B. Mindur[88a], M. Mineev[40], Y. Mino[90], L.M. Mir[13], M. Miralles Lopez[61], M. Mironova[18a], M.C. Missio[117], A. Mitra[172], V.A. Mitsou[168], Y. Mitsumori[114], O. Miu[159], P.S. Miyagawa[97], T. Mkrtchyan[65a], M. Mlinarevic[99], T. Mlinarevic[99], M. Mlynarikova[37], S. Mobius[20], P. Mogg[112], M.H. Mohamed Farook[116], A.F. Mohammed[14,115c], S. Mohapatra[43], G. Mokgatitswane[34g], L. Moleri[174], B. Mondal[146], S. Mondal[136], K. Mönig[50], E. Monnier[105], L. Monsonis Romero[168], J. Montejo Berlingen[13], A. Montella[49a,49b], M. Montella[123], F. Montereali[79a,79b], F. Monticelli[93], S. Monzani[71a,71c], A. Morancho Tarda[44], N. Morange[68], A.L. Moreira De Carvalho[50], M. Moreno Llácer[168], C. Moreno Martinez[58], J.M. Moreno Perez[23b], P. Morettini[59b], S. Morgenstern[37], M. Morii[63],

M. Morinaga[158], M. Moritsu[91], F. Morodei[77a,77b], P. Moschovakos[37], B. Moser[130], M. Mosidze[154b], T. Moskalets[46], P. Moskvitina[117], J. Moss[32,k], P. Moszkowicz[88a], A. Moussa[36d], Y. Moyal[174], E.J.W. Moyse[106], O. Mtintsilana[34g], S. Muanza[105], J. Mueller[133], D. Muenstermann[94], R. Müller[37], G.A. Mullier[166], A.J. Mullin[33], J.J. Mullin[132], A.E. Mulski[63], D.P. Mungo[159], D. Munoz Perez[168], F.J. Munoz Sanchez[104], M. Murin[104], W.J. Murray[172,138], M. Muškinja[96], C. Mwewa[30], A.G. Myagkov[39,a], A.J. Myers[8], G. Myers[109], M. Myska[136], B.P. Nachman[18a], O. Nackenhorst[51], K. Nagai[130], K. Nagano[86], R. Nagasaka[158], J.L. Nagle[30,ah], E. Nagy[105], A.M. Nairz[37], Y. Nakahama[86], K. Nakamura[86], K. Nakkalil[5], H. Nanjo[128], E.A. Narayanan[46], I. Naryshkin[39], L. Nasella[73a,73b], M. Naseri[35], S. Nasri[120b], C. Nass[25], G. Navarro[23a], J. Navarro-Gonzalez[168], R. Nayak[156], A. Nayaz[19], P.Y. Nechaeva[39], S. Nechaeva[24b,24a], F. Nechansky[135], L. Nedic[130], T.J. Neep[21], A. Negri[75a,75b], M. Negrini[24b], C. Nellist[118], C. Nelson[107], K. Nelson[109], S. Nemecek[135], M. Nessi[37,h], M.S. Neubauer[167], F. Neuhaus[103], J. Neundorf[50], J. Newell[95], P.R. Newman[21], C.W. Ng[133], Y.W.Y. Ng[50], B. Ngair[120a], H.D.N. Nguyen[111], R.B. Nickerson[130], R. Nicolaidou[139], J. Nielsen[140], M. Niemeyer[57], J. Niermann[57], N. Nikiforou[37], V. Nikolaenko[39,a], I. Nikolic-Audit[131], K. Nikolopoulos[21], P. Nilsson[30], I. Ninca[50], G. Ninio[156], A. Nisati[77a], N. Nishu[2], R. Nisius[113], N. Nitika[71a,71c], J-E. Nitschke[52], E.K. Nkadimeng[34g], T. Nobe[158], T. Nommensen[152], M.B. Norfolk[144], B.J. Norman[35], M. Noury[36a], J. Novak[96], T. Novak[96], L. Novotny[136], R. Novotny[116], L. Nozka[126], K. Ntekas[163], N.M.J. Nunes De Moura Junior[85b], J. Ocariz[131], A. Ochi[87], I. Ochoa[134a], S. Oerdek[50,v], J.T. Offermann[41], A. Ogrodnik[137], A. Oh[104], C.C. Ohm[149], H. Oide[86], R. Oishi[158], M.L. Ojeda[37], Y. Okumura[158], L.F. Oleiro Seabra[134a], I. Oleksiyuk[58], S.A. Olivares Pino[141d], G. Oliveira Correa[13], D. Oliveira Damazio[30], J.L. Oliver[163], Ö.O. Öncel[56], A.P. O'Neill[20], A. Onofre[134a,134e], P.U.E. Onyisi[11], M.J. Oreglia[41], G.E. Orellana[93], D. Orestano[79a,79b], N. Orlando[13], R.S. Orr[159], L.M. Osojnak[132], R. Ospanov[64a], Y. Osumi[114], G. Otero y Garzon[31], H. Otono[91], P.S. Ott[65a], G.J. Ottino[18a], M. Ouchrif[36d], F. Ould-Saada[129], T. Ovsiannikova[143], M. Owen[61], R.E. Owen[138], V.E. Ozcan[22a], F. Ozturk[89], N. Ozturk[8], S. Ozturk[84], H.A. Pacey[130], A. Pacheco Pages[13], C. Padilla Aranda[13], G. Padovano[77a,77b], S. Pagan Griso[18a], G. Palacino[70], A. Palazzo[72a,72b], J. Pampel[25], J. Pan[177], T. Pan[66a], D.K. Panchal[11], C.E. Pandini[118], J.G. Panduro Vazquez[138], H.D. Pandya[1], H. Pang[15], P. Pani[50], G. Panizzo[71a,71c], L. Panwar[131], L. Paolozzi[58], S. Parajuli[167], A. Paramonov[6], C. Paraskevopoulos[55], D. Paredes Hernandez[66b], A. Pareti[75a,75b], K.R. Park[43], T.H. Park[159], M.A. Parker[33], F. Parodi[59b,59a], E.W. Parrish[119], V.A. Parrish[54], J.A. Parsons[43], U. Parzefall[56], B. Pascual Dias[111], L. Pascual Dominguez[102], E. Pasqualucci[77a], S. Passaggio[59b], F. Pastore[98], P. Patel[89], U.M. Patel[53], J.R. Pater[104], T. Pauly[37], F. Pauwels[137], C.I. Pazos[162], M. Pedersen[129], R. Pedro[134a], S.V. Peleganchuk[39], O. Penc[37], E.A. Pender[54], S. Peng[15], G.D. Penn[177], K.E. Penski[112], M. Penzin[39], B.S. Peralva[85d], A.P. Pereira Peixoto[143], L. Pereira Sanchez[148], D.V. Perepelitsa[30,ah], G. Perera[106], E. Perez Codina[160a], M. Perganti[10], H. Pernegger[37], S. Perrella[77a,77b], O. Perrin[42], K. Peters[50], R.F.Y. Peters[104], B.A. Petersen[37], T.C. Petersen[44], E. Petit[105], V. Petousis[136], C. Petridou[157,e], T. Petru[137],

JHEP08(2025)034

A. Petrukhin[146], M. Pettee[18a], A. Petukhov[39], K. Petukhova[37], R. Pezoa[141f], L. Pezzotti[37], G. Pezzullo[177], A.J. Pfleger[37], T.M. Pham[175], T. Pham[108], P.W. Phillips[138], G. Piacquadio[150], E. Pianori[18a], F. Piazza[127], R. Piegaia[31], D. Pietreanu[28b], A.D. Pilkington[104], M. Pinamonti[71a,71c], J.L. Pinfold[2], B.C. Pinheiro Pereira[134a], J. Pinol Bel[13], A.E. Pinto Pinoargote[139,139], L. Pintucci[71a,71c], K.M. Piper[151], A. Pirttikoski[58], D.A. Pizzi[35], L. Pizzimento[66b], A. Pizzini[118], M.-A. Pleier[30], V. Pleskot[137], E. Plotnikova[40], G. Poddar[97], R. Poettgen[101], L. Poggioli[131], I. Pokharel[57], S. Polacek[137], G. Polesello[75a], A. Poley[147,160a], A. Polini[24b], C.S. Pollard[172], Z.B. Pollock[123], E. Pompa Pacchi[77a,77b], N.I. Pond[99], D. Ponomarenko[70], L. Pontecorvo[37], S. Popa[28a], G.A. Popeneciu[28d], A. Poreba[37], D.M. Portillo Quintero[160a], S. Pospisil[136], M.A. Postill[144], P. Postolache[28c], K. Potamianos[172], P.A. Potepa[88a], I.N. Potrap[40], C.J. Potter[33], H. Potti[152], J. Poveda[168], M.E. Pozo Astigarraga[37], A. Prades Ibanez[78a,78b], J. Pretel[170], D. Price[104], M. Primavera[72a], L. Primomo[71a,71c], M.A. Principe Martin[102], R. Privara[126], T. Procter[61], M.L. Proffitt[143], N. Proklova[132], K. Prokofiev[66c], G. Proto[113], J. Proudfoot[6], M. Przybycien[88a], W.W. Przygoda[88b], A. Psallidas[48], J.E. Puddefoot[144], D. Pudzha[56], D. Pyatiizbyantseva[39], J. Qian[109], R. Qian[110], D. Qichen[104], Y. Qin[13], T. Qiu[54], A. Quadt[57], M. Queitsch-Maitland[104], G. Quetant[58], R.P. Quinn[169], G. Rabanal Bolanos[63], D. Rafanoharana[56], F. Raffaeli[78a,78b], F. Ragusa[73a,73b], J.L. Rainbolt[41], J.A. Raine[58], S. Rajagopalan[30], E. Ramakoti[39], L. Rambelli[59b,59a], I.A. Ramirez-Berend[35], K. Ran[50,115c], D.S. Rankin[132], N.P. Rapheeha[34g], H. Rasheed[28b], V. Raskina[131], D.F. Rassloff[65a], A. Rastogi[18a], S. Rave[103], S. Ravera[59b,59a], B. Ravina[57], I. Ravinovich[174], M. Raymond[37], A.L. Read[129], N.P. Readioff[144], D.M. Rebuzzi[75a,75b], G. Redlinger[30], A.S. Reed[113], K. Reeves[27], J.A. Reidelsturz[176], D. Reikher[127], A. Rej[51], C. Rembser[37], M. Renda[28b], F. Renner[50], A.G. Rennie[163], A.L. Rescia[50], S. Resconi[73a], M. Ressegotti[59b,59a], S. Rettie[37], J.G. Reyes Rivera[110], E. Reynolds[18a], O.L. Rezanova[39], P. Reznicek[137], H. Riani[36d], N. Ribaric[53], E. Ricci[80a,80b], R. Richter[113], S. Richter[49a,49b], E. Richter-Was[88b], M. Ridel[131], S. Ridouani[36d], P. Rieck[121], P. Riedler[37], E.M. Riefel[49a,49b], J.O. Rieger[118], M. Rijssenbeek[150], M. Rimoldi[37], L. Rinaldi[24b,24a], P. Rincke[57], T.T. Rinn[30], M.P. Rinnagel[112], G. Ripellino[166], I. Riu[13], J.C. Rivera Vergara[170], F. Rizatdinova[125], E. Rizvi[97], B.R. Roberts[18a], S.S. Roberts[140], S.H. Robertson[107,y], D. Robinson[33], M. Robles Manzano[103], A. Robson[61], A. Rocchi[78a,78b], C. Roda[76a,76b], S. Rodriguez Bosca[37], Y. Rodriguez Garcia[23a], A. Rodriguez Rodriguez[56], A.M. Rodríguez Vera[119], S. Roe[37], J.T. Roemer[37], A.R. Roepe-Gier[140], O. Røhne[129], R.A. Rojas[37], C.P.A. Roland[131], J. Roloff[30], A. Romaniouk[81], E. Romano[75a,75b], M. Romano[24b], A.C. Romero Hernandez[167], N. Rompotis[95], L. Roos[131], S. Rosati[77a], B.J. Rosser[41], E. Rossi[130], E. Rossi[74a,74b], L.P. Rossi[63], L. Rossini[56], R. Rosten[123], M. Rotaru[28b], B. Rottler[56], C. Rougier[92], D. Rousseau[68], D. Rousso[50], A. Roy[167], S. Roy-Garand[159], A. Rozanov[105], Z.M.A. Rozario[61], Y. Rozen[155], A. Rubio Jimenez[168], A.J. Ruby[95], V.H. Ruelas Rivera[19], T.A. Ruggeri[1], A. Ruggiero[130], A. Ruiz-Martinez[168], A. Rummler[37], Z. Rurikova[56], N.A. Rusakovich[40], H.L. Russell[170], G. Russo[77a,77b], J.P. Rutherfoord[7], S. Rutherford Colmenares[33], M. Rybar[137], E.B. Rye[129], A. Ryzhov[46], J.A. Sabater Iglesias[58], H.F-W. Sadrozinski[140], F. Safai Tehrani[77a], B. Safarzadeh Samani[138],

JHEP08(2025)034

S. Saha[1], M. Sahinsoy[84], A. Saibel[168], M. Saimpert[139], M. Saito[158], T. Saito[158], A. Sala[73a,73b], D. Salamani[37], A. Salnikov[148], J. Salt[168], A. Salvador Salas[156], D. Salvatore[45b,45a], F. Salvatore[151], A. Salzburger[37], D. Sammel[56], E. Sampson[94], D. Sampsonidis[157,e], D. Sampsonidou[127], J. Sánchez[168], V. Sanchez Sebastian[168], H. Sandaker[129], C.O. Sander[50], J.A. Sandesara[106], M. Sandhoff[176], C. Sandoval[23b], L. Sanfilippo[65a], D.P.C. Sankey[138], T. Sano[90], A. Sansoni[55], L. Santi[37,77b], C. Santoni[42], H. Santos[134a,134b], A. Santra[174], E. Sanzani[24b,24a], K.A. Saoucha[165], J.G. Saraiva[134a,134d], J. Sardain[7], O. Sasaki[86], K. Sato[161], C. Sauer[37], E. Sauvan[4], P. Savard[159,af], R. Sawada[158], C. Sawyer[138], L. Sawyer[100], C. Sbarra[24b], A. Sbrizzi[24b,24a], T. Scanlon[99], J. Schaarschmidt[143], U. Schäfer[103], A.C. Schaffer[68,46], D. Schaile[112], R.D. Schamberger[150], C. Scharf[19], M.M. Schefer[20], V.A. Schegelsky[39], D. Scheirich[137], M. Schernau[141e], C. Scheulen[57], C. Schiavi[59b,59a], M. Schioppa[45b,45a], B. Schlag[148], S. Schlenker[37], J. Schmeing[176], M.A. Schmidt[176], K. Schmieden[103], C. Schmitt[103], N. Schmitt[103], S. Schmitt[50], L. Schoeffel[139], A. Schoening[65b], P.G. Scholer[35], E. Schopf[130], M. Schott[25], J. Schovancova[37], S. Schramm[58], T. Schroer[58], H-C. Schultz-Coulon[65a], M. Schumacher[56], B.A. Schumm[140], Ph. Schune[139], A.J. Schuy[143], H.R. Schwartz[140], A. Schwartzman[148], T.A. Schwarz[109], Ph. Schwemling[139], R. Schwienhorst[110], F.G. Sciacca[20], A. Sciandra[30], G. Sciolla[27], F. Scuri[76a], C.D. Sebastiani[95], K. Sedlaczek[119], S.C. Seidel[116], A. Seiden[140], B.D. Seidlitz[43], C. Seitz[50], J.M. Seixas[85b], G. Sekhniaidze[74a], L. Selem[62], N. Semprini-Cesari[24b,24a], D. Sengupta[58], V. Senthilkumar[168], L. Serin[68], M. Sessa[78a,78b], H. Severini[124], F. Sforza[59b,59a], A. Sfyrla[58], Q. Sha[14], E. Shabalina[57], A.H. Shah[33], R. Shaheen[149], J.D. Shahinian[132], D. Shaked Renous[174], L.Y. Shan[14], M. Shapiro[18a], A. Sharma[37], A.S. Sharma[169], P. Sharma[82], P.B. Shatalov[39], K. Shaw[151], S.M. Shaw[104], Q. Shen[64c], D.J. Sheppard[147], P. Sherwood[99], L. Shi[99], X. Shi[14], S. Shimizu[86], C.O. Shimmin[177], J.D. Shinner[98], I.P.J. Shipsey[130,*], S. Shirabe[91], M. Shiyakova[40,w], M.J. Shochet[41], D.R. Shope[129], B. Shrestha[124], S. Shrestha[123,ai], I. Shreyber[39], M.J. Shroff[170], P. Sicho[135], A.M. Sickles[167], E. Sideras Haddad[34g,164], A.C. Sidley[118], A. Sidoti[24b], F. Siegert[52], Dj. Sijacki[16], F. Sili[93], J.M. Silva[54], I. Silva Ferreira[85b], M.V. Silva Oliveira[30], S.B. Silverstein[49a], S. Simion[68], R. Simoniello[37], E.L. Simpson[104], H. Simpson[151], L.R. Simpson[109], S. Simsek[84], S. Sindhu[57], P. Sinervo[159], S. Singh[30], S. Sinha[50], S. Sinha[104], M. Sioli[24b,24a], I. Siral[37], E. Sitnikova[50], J. Sjölin[49a,49b], A. Skaf[57], E. Skorda[21], P. Skubic[124], M. Slawinska[89], V. Smakhtin[174], B.H. Smart[138], S.Yu. Smirnov[39], Y. Smirnov[39], L.N. Smirnova[39,a], O. Smirnova[101], A.C. Smith[43], D.R. Smith[163], E.A. Smith[41], J.L. Smith[104], R. Smith[148], H. Smitmanns[103], M. Smizanska[94], K. Smolek[136], A.A. Snesarev[39], H.L. Snoek[118], S. Snyder[30], R. Sobie[170,y], A. Soffer[156], C.A. Solans Sanchez[37], E.Yu. Soldatov[39], U. Soldevila[168], A.A. Solodkov[39], S. Solomon[27], A. Soloshenko[40], K. Solovieva[56], O.V. Solovyanov[42], P. Sommer[52], A. Sonay[13], W.Y. Song[160b], A. Sopczak[136], A.L. Sopio[54], F. Sopkova[29b], J.D. Sorenson[116], I.R. Sotarriva Alvarez[142], V. Sothilingam[65a], O.J. Soto Sandoval[141c,141b], S. Sottocornola[70], R. Soualah[165], Z. Soumaimi[36e], D. South[50], N. Soybelman[174], S. Spagnolo[72a,72b], M. Spalla[113], D. Sperlich[56], G. Spigo[37], B. Spisso[74a,74b], D.P. Spiteri[61], M. Spousta[137], E.J. Staats[35], R. Stamen[65a], A. Stampekis[21], E. Stanecka[89], W. Stanek-Maslouska[50], M.V. Stange[52], B. Stanislaus[18a], M.M. Stanitzki[50], B. Stapf[50], E.A. Starchenko[39],

JHEP08(2025)034

G.H. Stark[140], J. Stark[92], P. Staroba[135], P. Starovoitov[65a], S. Stärz[107], R. Staszewski[89], G. Stavropoulos[48], A. Stefl[37], P. Steinberg[30], B. Stelzer[147,160a], H.J. Stelzer[133], O. Stelzer-Chilton[160a], H. Stenzel[60], T.J. Stevenson[151], G.A. Stewart[37], J.R. Stewart[125], M.C. Stockton[37], G. Stoicea[28b], M. Stolarski[134a], S. Stonjek[113], A. Straessner[52], J. Strandberg[149], S. Strandberg[49a,49b], M. Stratmann[176], M. Strauss[124], T. Strebler[105], P. Strizenec[29b], R. Ströhmer[171], D.M. Strom[127], R. Stroynowski[46], A. Strubig[49a,49b], S.A. Stucci[30], B. Stugu[17], J. Stupak[124], N.A. Styles[50], D. Su[148], S. Su[64a], W. Su[64d], X. Su[64a], D. Suchy[29a], K. Sugizaki[158], V.V. Sulin[39], M.J. Sullivan[95], D.M.S. Sultan[130], L. Sultanaliyeva[39], S. Sultansoy[3b], T. Sumida[90], S. Sun[175], O. Sunneborn Gudnadottir[166], N. Sur[105], M.R. Sutton[151], H. Suzuki[161], M. Svatos[135], M. Swiatlowski[160a], T. Swirski[171], I. Sykora[29a], M. Sykora[137], T. Sykora[137], D. Ta[103], K. Tackmann[50,v], A. Taffard[163], R. Tafirout[160a], J.S. Tafoya Vargas[68], Y. Takubo[86], M. Talby[105], A.A. Talyshev[39], K.C. Tam[66b], N.M. Tamir[156], A. Tanaka[158], J. Tanaka[158], R. Tanaka[68], M. Tanasini[150], Z. Tao[169], S. Tapia Araya[141f], S. Tapprogge[103], A. Tarek Abouelfadl Mohamed[110], S. Tarem[155], K. Tariq[14], G. Tarna[28b], G.F. Tartarelli[73a], M.J. Tartarin[92], P. Tas[137], M. Tasevsky[135], E. Tassi[45b,45a], A.C. Tate[167], G. Tateno[158], Y. Tayalati[36e,x], G.N. Taylor[108], W. Taylor[160b], R. Teixeira De Lima[148], P. Teixeira-Dias[98], J.J. Teoh[159], K. Terashi[158], J. Terron[102], S. Terzo[13], M. Testa[55], R.J. Teuscher[159,y], A. Thaler[81], O. Theiner[58], T. Theveneaux-Pelzer[105], O. Thielmann[176], D.W. Thomas[98], J.P. Thomas[21], E.A. Thompson[18a], P.D. Thompson[21], E. Thomson[132], R.E. Thornberry[46], C. Tian[64a], Y. Tian[58], V. Tikhomirov[39,a], Yu.A. Tikhonov[39], S. Timoshenko[39], D. Timoshyn[137], E.X.L. Ting[1], P. Tipton[177], A. Tishelman-Charny[30], S.H. Tlou[34g], K. Todome[142], S. Todorova-Nova[137], S. Todt[52], L. Toffolin[71a,71c], M. Togawa[86], J. Tojo[91], S. Tokár[29a], K. Tokushuku[86], O. Toldaiev[70], M. Tomoto[86,114], L. Tompkins[148,m], K.W. Topolnicki[88b], E. Torrence[127], H. Torres[92], E. Torró Pastor[168], M. Toscani[31], C. Tosciri[41], M. Tost[11], D.R. Tovey[144], I.S. Trandafir[28b], T. Trefzger[171], A. Tricoli[30], I.M. Trigger[160a], S. Trincaz-Duvoid[131], D.A. Trischuk[27], B. Trocmé[62], A. Tropina[40], L. Truong[34c], M. Trzebinski[89], A. Trzupek[89], F. Tsai[150], M. Tsai[109], A. Tsiamis[157], P.V. Tsiareshka[40], S. Tsigaridas[160a], A. Tsirigotis[157,s], V. Tsiskaridze[159], E.G. Tskhadadze[154a], M. Tsopoulou[157], Y. Tsujikawa[90], I.I. Tsukerman[39], V. Tsulaia[18a], S. Tsuno[86], K. Tsuri[122], D. Tsybychev[150], Y. Tu[66b], A. Tudorache[28b], V. Tudorache[28b], A.N. Tuna[63], S. Turchikhin[59b,59a], I. Turk Cakir[3a], R. Turra[73a], T. Turtuvshin[40,z], P.M. Tuts[43], S. Tzamarias[157,e], E. Tzovara[103], F. Ukegawa[161], P.A. Ulloa Poblete[141c,141b], E.N. Umaka[30], G. Unal[37], A. Undrus[30], G. Unel[163], J. Urban[29b], P. Urrejola[141a], G. Usai[8], R. Ushioda[142], M. Usman[111], F. Ustuner[54], Z. Uysal[84], V. Vacek[136], B. Vachon[107], T. Vafeiadis[37], A. Vaitkus[99], C. Valderanis[112], E. Valdes Santurio[49a,49b], M. Valente[160a], S. Valentinetti[24b,24a], A. Valero[168], E. Valiente Moreno[168], A. Vallier[92], J.A. Valls Ferrer[168], D.R. Van Arneman[118], T.R. Van Daalen[143], A. Van Der Graaf[51], P. Van Gemmeren[6], M. Van Rijnbach[37], S. Van Stroud[99], I. Van Vulpen[118], P. Vana[137], M. Vanadia[78a,78b], U.M. Vande Voorde[149], W. Vandelli[37], E.R. Vandewall[125], D. Vannicola[156], L. Vannoli[55], R. Vari[77a], E.W. Varnes[7], C. Varni[18b], T. Varol[153], D. Varouchas[68], L. Varriale[168], K.E. Varvell[152], M.E. Vasile[28b], L. Vaslin[86], G.A. Vasquez[170], A. Vasyukov[40], L.M. Vaughan[125], R. Vavricka[103], T. Vazquez Schroeder[37],

JHEP08(2025)034

J. Veatch[32], V. Vecchio[104], M.J. Veen[106], I. Veliscek[30], L.M. Veloce[159], F. Veloso[134a,134c], S. Veneziano[77a], A. Ventura[72a,72b], S. Ventura Gonzalez[139], A. Verbytskyi[113], M. Verducci[76a,76b], C. Vergis[97], M. Verissimo De Araujo[85b], W. Verkerke[118], J.C. Vermeulen[118], C. Vernieri[148], M. Vessella[106], M.C. Vetterli[147,af], A. Vgenopoulos[103], N. Viaux Maira[141f], T. Vickey[144], O.E. Vickey Boeriu[144], G.H.A. Viehhauser[130], L. Vigani[65b], M. Vigl[113], M. Villa[24b,24a], M. Villaplana Perez[168], E.M. Villhauer[54], E. Vilucchi[55], M.G. Vincter[35], A. Visibile[118], C. Vittori[37], I. Vivarelli[24b,24a], E. Voevodina[113], F. Vogel[112], J.C. Voigt[52], P. Vokac[136], Yu. Volkotrub[88b], E. Von Toerne[25], B. Vormwald[37], V. Vorobel[137], K. Vorobev[39], M. Vos[168], K. Voss[146], M. Vozak[118], L. Vozdecky[124], N. Vranjes[16], M. Vranjes Milosavljevic[16], M. Vreeswijk[118], N.K. Vu[64d,64c], R. Vuillermet[37], O. Vujinovic[103], I. Vukotic[41], I.K. Vyas[35], S. Wada[161], C. Wagner[148], J.M. Wagner[18a], W. Wagner[176], S. Wahdan[176], H. Wahlberg[93], C.H. Waits[124], J. Walder[138], R. Walker[112], W. Walkowiak[146], A. Wall[132], E.J. Wallin[101], T. Wamorkar[6], A.Z. Wang[140], C. Wang[103], C. Wang[11], H. Wang[18a], J. Wang[66c], P. Wang[99], R. Wang[63], R. Wang[6], S.M. Wang[153], S. Wang[64b], S. Wang[14], T. Wang[64a], W.T. Wang[82], W. Wang[14], X. Wang[115a], X. Wang[167], X. Wang[64c], Y. Wang[64d], Y. Wang[115a], Y. Wang[64a], Z. Wang[109], Z. Wang[64d,53,64c], Z. Wang[109], A. Warburton[107], R.J. Ward[21], N. Warrack[61], S. Waterhouse[98], A.T. Watson[21], H. Watson[54], M.F. Watson[21], E. Watton[61,138], G. Watts[143], B.M. Waugh[99], J.M. Webb[56], C. Weber[30], H.A. Weber[19], M.S. Weber[20], S.M. Weber[65a], C. Wei[64a], Y. Wei[56], A.R. Weidberg[130], E.J. Weik[121], J. Weingarten[51], C. Weiser[56], C.J. Wells[50], T. Wenaus[30], B. Wendland[51], T. Wengler[37], N.S. Wenke[113], N. Wermes[25], M. Wessels[65a], A.M. Wharton[94], A.S. White[63], A. White[8], M.J. White[1], D. Whiteson[163], L. Wickremasinghe[128], W. Wiedenmann[175], M. Wielers[138], C. Wiglesworth[44], D.J. Wilbern[124], H.G. Wilkens[37], J.J.H. Wilkinson[33], D.M. Williams[43], H.H. Williams[132], S. Williams[33], S. Willocq[106], B.J. Wilson[104], P.J. Windischhofer[41], F.I. Winkel[31], F. Winklmeier[127], B.T. Winter[56], J.K. Winter[104], M. Wittgen[148], M. Wobisch[100], T. Wojtkowski[62], Z. Wolffs[118], J. Wollrath[37], M.W. Wolter[89], H. Wolters[134a,134c], M.C. Wong[140], E.L. Woodward[43], S.D. Worm[50], B.K. Wosiek[89], K.W. Woźniak[89], S. Wozniewski[57], K. Wraight[61], C. Wu[21], M. Wu[115b], M. Wu[117], S.L. Wu[175], X. Wu[58], Y. Wu[64a], Z. Wu[4], J. Wuerzinger[113,ad], T.R. Wyatt[104], B.M. Wynne[54], S. Xella[44], L. Xia[115a], M. Xia[15], M. Xie[64a], S. Xin[14,115c], A. Xiong[127], J. Xiong[18a], D. Xu[14], H. Xu[64a], L. Xu[64a], R. Xu[132], T. Xu[109], Y. Xu[143], Z. Xu[54], Z. Xu[115a], B. Yabsley[152], S. Yacoob[34a], Y. Yamaguchi[86], E. Yamashita[158], H. Yamauchi[161], T. Yamazaki[18a], Y. Yamazaki[87], S. Yan[61], Z. Yan[106], H.J. Yang[64c,64d], H.T. Yang[64a], S. Yang[64a], T. Yang[66c], X. Yang[37], X. Yang[14], Y. Yang[46], Y. Yang[64a], Z. Yang[64a], W-M. Yao[18a], H. Ye[115a], H. Ye[57], J. Ye[14], S. Ye[30], X. Ye[64a], Y. Yeh[99], I. Yeletskikh[40], B. Yeo[18b], M.R. Yexley[99], T.P. Yildirim[130], P. Yin[43], K. Yorita[173], S. Younas[28b], C.J.S. Young[37], C. Young[148], C. Yu[14,115c], Y. Yu[64a], J. Yuan[14,115c], M. Yuan[109], R. Yuan[64d,64c], L. Yue[99], M. Zaazoua[64a], B. Zabinski[89], E. Zaid[54], Z.K. Zak[89], T. Zakareishvili[168], S. Zambito[58], J.A. Zamora Saa[141d,141b], J. Zang[158], D. Zanzi[56], O. Zaplatilek[136], C. Zeitnitz[176], H. Zeng[14], J.C. Zeng[167], D.T. Zenger Jr[27], O. Zenin[39], T. Ženiš[29a], S. Zenz[97], S. Zerradi[36a], D. Zerwas[68], M. Zhai[14,115c], D.F. Zhang[144], J. Zhang[64b],

J. Zhang[6], K. Zhang[14,115c], L. Zhang[64a], L. Zhang[115a], P. Zhang[14,115c], R. Zhang[175], S. Zhang[109], S. Zhang[92], T. Zhang[158], X. Zhang[64c], Y. Zhang[143], Y. Zhang[99], Y. Zhang[115a], Z. Zhang[18a], Z. Zhang[64b], Z. Zhang[68], H. Zhao[143], T. Zhao[64b], Y. Zhao[140], Z. Zhao[64a], Z. Zhao[64a], A. Zhemchugov[40], J. Zheng[115a], K. Zheng[167], X. Zheng[64a], Z. Zheng[148], D. Zhong[167], B. Zhou[109], H. Zhou[7], N. Zhou[64c], Y. Zhou[15], Y. Zhou[115a], Y. Zhou[7], C.G. Zhu[64b], J. Zhu[109], X. Zhu[64d], Y. Zhu[64c], Y. Zhu[64a], X. Zhuang[14], K. Zhukov[70], N.I. Zimine[40], J. Zinsser[65b], M. Ziolkowski[146], L. Živković[16], A. Zoccoli[24b,24a], K. Zoch[63], T.G. Zorbas[144], O. Zormpa[48], W. Zou[43], L. Zwalinski[37]

[1] *Department of Physics, University of Adelaide, Adelaide; Australia*
[2] *Department of Physics, University of Alberta, Edmonton AB; Canada*
[3] [(a)] *Department of Physics, Ankara University, Ankara;* [(b)] *Division of Physics, TOBB University of Economics and Technology, Ankara; Türkiye*
[4] *LAPP, Université Savoie Mont Blanc, CNRS/IN2P3, Annecy; France*
[5] *APC, Université Paris Cité, CNRS/IN2P3, Paris; France*
[6] *High Energy Physics Division, Argonne National Laboratory, Argonne IL; United States of America*
[7] *Department of Physics, University of Arizona, Tucson AZ; United States of America*
[8] *Department of Physics, University of Texas at Arlington, Arlington TX; United States of America*
[9] *Physics Department, National and Kapodistrian University of Athens, Athens; Greece*
[10] *Physics Department, National Technical University of Athens, Zografou; Greece*
[11] *Department of Physics, University of Texas at Austin, Austin TX; United States of America*
[12] *Institute of Physics, Azerbaijan Academy of Sciences, Baku; Azerbaijan*
[13] *Institut de Física d'Altes Energies (IFAE), Barcelona Institute of Science and Technology, Barcelona; Spain*
[14] *Institute of High Energy Physics, Chinese Academy of Sciences, Beijing; China*
[15] *Physics Department, Tsinghua University, Beijing; China*
[16] *Institute of Physics, University of Belgrade, Belgrade; Serbia*
[17] *Department for Physics and Technology, University of Bergen, Bergen; Norway*
[18] [(a)] *Physics Division, Lawrence Berkeley National Laboratory, Berkeley CA;* [(b)] *University of California, Berkeley CA; United States of America*
[19] *Institut für Physik, Humboldt Universität zu Berlin, Berlin; Germany*
[20] *Albert Einstein Center for Fundamental Physics and Laboratory for High Energy Physics, University of Bern, Bern; Switzerland*
[21] *School of Physics and Astronomy, University of Birmingham, Birmingham; United Kingdom*
[22] [(a)] *Department of Physics, Bogazici University, Istanbul;* [(b)] *Department of Physics Engineering, Gaziantep University, Gaziantep;* [(c)] *Department of Physics, Istanbul University, Istanbul; Türkiye*
[23] [(a)] *Facultad de Ciencias y Centro de Investigaciónes, Universidad Antonio Nariño, Bogotá;* [(b)] *Departamento de Física, Universidad Nacional de Colombia, Bogotá; Colombia*
[24] [(a)] *Dipartimento di Fisica e Astronomia A. Righi, Università di Bologna, Bologna;* [(b)] *INFN Sezione di Bologna; Italy*
[25] *Physikalisches Institut, Universität Bonn, Bonn; Germany*
[26] *Department of Physics, Boston University, Boston MA; United States of America*
[27] *Department of Physics, Brandeis University, Waltham MA; United States of America*
[28] [(a)] *Transilvania University of Brasov, Brasov;* [(b)] *Horia Hulubei National Institute of Physics and Nuclear Engineering, Bucharest;* [(c)] *Department of Physics, Alexandru Ioan Cuza University of Iasi, Iasi;* [(d)] *National Institute for Research and Development of Isotopic and Molecular Technologies, Physics Department, Cluj-Napoca;* [(e)] *National University of Science and Technology Politechnica, Bucharest;* [(f)] *West University in Timisoara, Timisoara;* [(g)] *Faculty of Physics, University of Bucharest, Bucharest; Romania*
[29] [(a)] *Faculty of Mathematics, Physics and Informatics, Comenius University, Bratislava;* [(b)] *Department of Subnuclear Physics, Institute of Experimental Physics of the Slovak Academy of Sciences, Kosice; Slovak Republic*
[30] *Physics Department, Brookhaven National Laboratory, Upton NY; United States of America*

JHEP08(2025)034

[31] *Universidad de Buenos Aires, Facultad de Ciencias Exactas y Naturales, Departamento de Física, y CONICET, Instituto de Física de Buenos Aires (IFIBA), Buenos Aires; Argentina*
[32] *California State University, CA; United States of America*
[33] *Cavendish Laboratory, University of Cambridge, Cambridge; United Kingdom*
[34] [(a)] *Department of Physics, University of Cape Town, Cape Town;* [(b)] *iThemba Labs, Western Cape;* [(c)] *Department of Mechanical Engineering Science, University of Johannesburg, Johannesburg;* [(d)] *National Institute of Physics, University of the Philippines Diliman (Philippines);* [(e)] *University of South Africa, Department of Physics, Pretoria;* [(f)] *University of Zululand, KwaDlangezwa;* [(g)] *School of Physics, University of the Witwatersrand, Johannesburg; South Africa*
[35] *Department of Physics, Carleton University, Ottawa ON; Canada*
[36] [(a)] *Faculté des Sciences Ain Chock, Université Hassan II de Casablanca;* [(b)] *Faculté des Sciences, Université Ibn-Tofail, Kénitra;* [(c)] *Faculté des Sciences Semlalia, Université Cadi Ayyad, LPHEA-Marrakech;* [(d)] *LPMR, Faculté des Sciences, Université Mohamed Premier, Oujda;* [(e)] *Faculté des sciences, Université Mohammed V, Rabat;* [(f)] *Institute of Applied Physics, Mohammed VI Polytechnic University, Ben Guerir; Morocco*
[37] *CERN, Geneva; Switzerland*
[38] *Affiliated with an institute formerly covered by a cooperation agreement with CERN*
[39] *Affiliated with an institute covered by a cooperation agreement with CERN*
[40] *Affiliated with an international laboratory covered by a cooperation agreement with CERN*
[41] *Enrico Fermi Institute, University of Chicago, Chicago IL; United States of America*
[42] *LPC, Université Clermont Auvergne, CNRS/IN2P3, Clermont-Ferrand; France*
[43] *Nevis Laboratory, Columbia University, Irvington NY; United States of America*
[44] *Niels Bohr Institute, University of Copenhagen, Copenhagen; Denmark*
[45] [(a)] *Dipartimento di Fisica, Università della Calabria, Rende;* [(b)] *INFN Gruppo Collegato di Cosenza, Laboratori Nazionali di Frascati; Italy*
[46] *Physics Department, Southern Methodist University, Dallas TX; United States of America*
[47] *Physics Department, University of Texas at Dallas, Richardson TX; United States of America*
[48] *National Centre for Scientific Research "Demokritos", Agia Paraskevi; Greece*
[49] [(a)] *Department of Physics, Stockholm University;* [(b)] *Oskar Klein Centre, Stockholm; Sweden*
[50] *Deutsches Elektronen-Synchrotron DESY, Hamburg and Zeuthen; Germany*
[51] *Fakultät Physik, Technische Universität Dortmund, Dortmund; Germany*
[52] *Institut für Kern- und Teilchenphysik, Technische Universität Dresden, Dresden; Germany*
[53] *Department of Physics, Duke University, Durham NC; United States of America*
[54] *SUPA — School of Physics and Astronomy, University of Edinburgh, Edinburgh; United Kingdom*
[55] *INFN e Laboratori Nazionali di Frascati, Frascati; Italy*
[56] *Physikalisches Institut, Albert-Ludwigs-Universität Freiburg, Freiburg; Germany*
[57] *II. Physikalisches Institut, Georg-August-Universität Göttingen, Göttingen; Germany*
[58] *Département de Physique Nucléaire et Corpusculaire, Université de Genève, Genève; Switzerland*
[59] [(a)] *Dipartimento di Fisica, Università di Genova, Genova;* [(b)] *INFN Sezione di Genova; Italy*
[60] *II. Physikalisches Institut, Justus-Liebig-Universität Giessen, Giessen; Germany*
[61] *SUPA — School of Physics and Astronomy, University of Glasgow, Glasgow; United Kingdom*
[62] *LPSC, Université Grenoble Alpes, CNRS/IN2P3, Grenoble INP, Grenoble; France*
[63] *Laboratory for Particle Physics and Cosmology, Harvard University, Cambridge MA; United States of America*
[64] [(a)] *Department of Modern Physics and State Key Laboratory of Particle Detection and Electronics, University of Science and Technology of China, Hefei;* [(b)] *Institute of Frontier and Interdisciplinary Science and Key Laboratory of Particle Physics and Particle Irradiation (MOE), Shandong University, Qingdao;* [(c)] *State Key Laboratory of Dark Matter Physics, School of Physics and Astronomy, Shanghai Jiao Tong University, Key Laboratory for Particle Astrophysics and Cosmology (MOE), SKLPPC, Shanghai;* [(d)] *State Key Laboratory of Dark Matter Physics, Tsung-Dao Lee Institute, Shanghai Jiao Tong University, Shanghai;* [(e)] *School of Physics, Zhengzhou University; China*
[65] [(a)] *Kirchhoff-Institut für Physik, Ruprecht-Karls-Universität Heidelberg, Heidelberg;* [(b)] *Physikalisches Institut, Ruprecht-Karls-Universität Heidelberg, Heidelberg; Germany*
[66] [(a)] *Department of Physics, Chinese University of Hong Kong, Shatin, N.T., Hong Kong;* [(b)] *Department of*

Physics, University of Hong Kong, Hong Kong;[(c)] Department of Physics and Institute for Advanced Study, Hong Kong University of Science and Technology, Clear Water Bay, Kowloon, Hong Kong; China
[67] Department of Physics, National Tsing Hua University, Hsinchu; Taiwan
[68] IJCLab, Université Paris-Saclay, CNRS/IN2P3, 91405, Orsay; France
[69] Centro Nacional de Microelectrónica (IMB-CNM-CSIC), Barcelona; Spain
[70] Department of Physics, Indiana University, Bloomington IN; United States of America
[71] [(a)] INFN Gruppo Collegato di Udine, Sezione di Trieste, Udine;[(b)] ICTP, Trieste;[(c)] Dipartimento Politecnico di Ingegneria e Architettura, Università di Udine, Udine; Italy
[72] [(a)] INFN Sezione di Lecce;[(b)] Dipartimento di Matematica e Fisica, Università del Salento, Lecce; Italy
[73] [(a)] INFN Sezione di Milano;[(b)] Dipartimento di Fisica, Università di Milano, Milano; Italy
[74] [(a)] INFN Sezione di Napoli;[(b)] Dipartimento di Fisica, Università di Napoli, Napoli; Italy
[75] [(a)] INFN Sezione di Pavia;[(b)] Dipartimento di Fisica, Università di Pavia, Pavia; Italy
[76] [(a)] INFN Sezione di Pisa;[(b)] Dipartimento di Fisica E. Fermi, Università di Pisa, Pisa; Italy
[77] [(a)] INFN Sezione di Roma;[(b)] Dipartimento di Fisica, Sapienza Università di Roma, Roma; Italy
[78] [(a)] INFN Sezione di Roma Tor Vergata;[(b)] Dipartimento di Fisica, Università di Roma Tor Vergata, Roma; Italy
[79] [(a)] INFN Sezione di Roma Tre;[(b)] Dipartimento di Matematica e Fisica, Università Roma Tre, Roma; Italy
[80] [(a)] INFN-TIFPA;[(b)] Università degli Studi di Trento, Trento; Italy
[81] Universität Innsbruck, Department of Astro and Particle Physics, Innsbruck; Austria
[82] University of Iowa, Iowa City IA; United States of America
[83] Department of Physics and Astronomy, Iowa State University, Ames IA; United States of America
[84] Istinye University, Sariyer, Istanbul; Türkiye
[85] [(a)] Departamento de Engenharia Elétrica, Universidade Federal de Juiz de Fora (UFJF), Juiz de Fora;[(b)] Universidade Federal do Rio De Janeiro COPPE/EE/IF, Rio de Janeiro;[(c)] Instituto de Física, Universidade de São Paulo, São Paulo;[(d)] Rio de Janeiro State University, Rio de Janeiro;[(e)] Federal University of Bahia, Bahia; Brazil
[86] KEK, High Energy Accelerator Research Organization, Tsukuba; Japan
[87] Graduate School of Science, Kobe University, Kobe; Japan
[88] [(a)] AGH University of Krakow, Faculty of Physics and Applied Computer Science, Krakow;[(b)] Marian Smoluchowski Institute of Physics, Jagiellonian University, Krakow; Poland
[89] Institute of Nuclear Physics Polish Academy of Sciences, Krakow; Poland
[90] Faculty of Science, Kyoto University, Kyoto; Japan
[91] Research Center for Advanced Particle Physics and Department of Physics, Kyushu University, Fukuoka; Japan
[92] L2IT, Université de Toulouse, CNRS/IN2P3, UPS, Toulouse; France
[93] Instituto de Física La Plata, Universidad Nacional de La Plata and CONICET, La Plata; Argentina
[94] Physics Department, Lancaster University, Lancaster; United Kingdom
[95] Oliver Lodge Laboratory, University of Liverpool, Liverpool; United Kingdom
[96] Department of Experimental Particle Physics, Jožef Stefan Institute and Department of Physics, University of Ljubljana, Ljubljana; Slovenia
[97] Department of Physics and Astronomy, Queen Mary University of London, London; United Kingdom
[98] Department of Physics, Royal Holloway University of London, Egham; United Kingdom
[99] Department of Physics and Astronomy, University College London, London; United Kingdom
[100] Louisiana Tech University, Ruston LA; United States of America
[101] Fysiska institutionen, Lunds universitet, Lund; Sweden
[102] Departamento de Física Teorica C-15 and CIAFF, Universidad Autónoma de Madrid, Madrid; Spain
[103] Institut für Physik, Universität Mainz, Mainz; Germany
[104] School of Physics and Astronomy, University of Manchester, Manchester; United Kingdom
[105] CPPM, Aix-Marseille Université, CNRS/IN2P3, Marseille; France
[106] Department of Physics, University of Massachusetts, Amherst MA; United States of America
[107] Department of Physics, McGill University, Montreal QC; Canada
[108] School of Physics, University of Melbourne, Victoria; Australia
[109] Department of Physics, University of Michigan, Ann Arbor MI; United States of America

JHEP08(2025)034

[110] *Department of Physics and Astronomy, Michigan State University, East Lansing MI; United States of America*
[111] *Group of Particle Physics, University of Montreal, Montreal QC; Canada*
[112] *Fakultät für Physik, Ludwig-Maximilians-Universität München, München; Germany*
[113] *Max-Planck-Institut für Physik (Werner-Heisenberg-Institut), München; Germany*
[114] *Graduate School of Science and Kobayashi-Maskawa Institute, Nagoya University, Nagoya; Japan*
[115] [(a)] *Department of Physics, Nanjing University, Nanjing;*[(b)] *School of Science, Shenzhen Campus of Sun Yat-sen University;*[(c)] *University of Chinese Academy of Science (UCAS), Beijing; China*
[116] *Department of Physics and Astronomy, University of New Mexico, Albuquerque NM; United States of America*
[117] *Institute for Mathematics, Astrophysics and Particle Physics, Radboud University/Nikhef, Nijmegen; Netherlands*
[118] *Nikhef National Institute for Subatomic Physics and University of Amsterdam, Amsterdam; Netherlands*
[119] *Department of Physics, Northern Illinois University, DeKalb IL; United States of America*
[120] [(a)] *New York University Abu Dhabi, Abu Dhabi;*[(b)] *United Arab Emirates University, Al Ain; United Arab Emirates*
[121] *Department of Physics, New York University, New York NY; United States of America*
[122] *Ochanomizu University, Otsuka, Bunkyo-ku, Tokyo; Japan*
[123] *Ohio State University, Columbus OH; United States of America*
[124] *Homer L. Dodge Department of Physics and Astronomy, University of Oklahoma, Norman OK; United States of America*
[125] *Department of Physics, Oklahoma State University, Stillwater OK; United States of America*
[126] *Palacký University, Joint Laboratory of Optics, Olomouc; Czech Republic*
[127] *Institute for Fundamental Science, University of Oregon, Eugene, OR; United States of America*
[128] *Graduate School of Science, University of Osaka, Osaka; Japan*
[129] *Department of Physics, University of Oslo, Oslo; Norway*
[130] *Department of Physics, Oxford University, Oxford; United Kingdom*
[131] *LPNHE, Sorbonne Université, Université Paris Cité, CNRS/IN2P3, Paris; France*
[132] *Department of Physics, University of Pennsylvania, Philadelphia PA; United States of America*
[133] *Department of Physics and Astronomy, University of Pittsburgh, Pittsburgh PA; United States of America*
[134] [(a)] *Laboratório de Instrumentação e Física Experimental de Partículas — LIP, Lisboa;*[(b)] *Departamento de Física, Faculdade de Ciências, Universidade de Lisboa, Lisboa;*[(c)] *Departamento de Física, Universidade de Coimbra, Coimbra;*[(d)] *Centro de Física Nuclear da Universidade de Lisboa, Lisboa;*[(e)] *Departamento de Física, Escola de Ciências, Universidade do Minho, Braga;*[(f)] *Departamento de Física Teórica y del Cosmos, Universidad de Granada, Granada (Spain);*[(g)] *Departamento de Física, Instituto Superior Técnico, Universidade de Lisboa, Lisboa; Portugal*
[135] *Institute of Physics of the Czech Academy of Sciences, Prague; Czech Republic*
[136] *Czech Technical University in Prague, Prague; Czech Republic*
[137] *Charles University, Faculty of Mathematics and Physics, Prague; Czech Republic*
[138] *Particle Physics Department, Rutherford Appleton Laboratory, Didcot; United Kingdom*
[139] *IRFU, CEA, Université Paris-Saclay, Gif-sur-Yvette; France*
[140] *Santa Cruz Institute for Particle Physics, University of California Santa Cruz, Santa Cruz CA; United States of America*
[141] [(a)] *Departamento de Física, Pontificia Universidad Católica de Chile, Santiago;*[(b)] *Millennium Institute for Subatomic physics at high energy frontier (SAPHIR), Santiago;*[(c)] *Instituto de Investigación Multidisciplinario en Ciencia y Tecnología, y Departamento de Física, Universidad de La Serena;*[(d)] *Universidad Andres Bello, Department of Physics, Santiago;*[(e)] *Instituto de Alta Investigación, Universidad de Tarapacá, Arica;*[(f)] *Departamento de Física, Universidad Técnica Federico Santa María, Valparaíso; Chile*
[142] *Department of Physics, Institute of Science, Tokyo; Japan*
[143] *Department of Physics, University of Washington, Seattle WA; United States of America*
[144] *Department of Physics and Astronomy, University of Sheffield, Sheffield; United Kingdom*
[145] *Department of Physics, Shinshu University, Nagano; Japan*

JHEP08(2025)034

[146] *Department Physik, Universität Siegen, Siegen; Germany*
[147] *Department of Physics, Simon Fraser University, Burnaby BC; Canada*
[148] *SLAC National Accelerator Laboratory, Stanford CA; United States of America*
[149] *Department of Physics, Royal Institute of Technology, Stockholm; Sweden*
[150] *Departments of Physics and Astronomy, Stony Brook University, Stony Brook NY; United States of America*
[151] *Department of Physics and Astronomy, University of Sussex, Brighton; United Kingdom*
[152] *School of Physics, University of Sydney, Sydney; Australia*
[153] *Institute of Physics, Academia Sinica, Taipei; Taiwan*
[154] [(a)] *E. Andronikashvili Institute of Physics, Iv. Javakhishvili Tbilisi State University, Tbilisi;*[(b)] *High Energy Physics Institute, Tbilisi State University, Tbilisi;*[(c)] *University of Georgia, Tbilisi; Georgia*
[155] *Department of Physics, Technion, Israel Institute of Technology, Haifa; Israel*
[156] *Raymond and Beverly Sackler School of Physics and Astronomy, Tel Aviv University, Tel Aviv; Israel*
[157] *Department of Physics, Aristotle University of Thessaloniki, Thessaloniki; Greece*
[158] *International Center for Elementary Particle Physics and Department of Physics, University of Tokyo, Tokyo; Japan*
[159] *Department of Physics, University of Toronto, Toronto ON; Canada*
[160] [(a)] *TRIUMF, Vancouver BC;*[(b)] *Department of Physics and Astronomy, York University, Toronto ON; Canada*
[161] *Division of Physics and Tomonaga Center for the History of the Universe, Faculty of Pure and Applied Sciences, University of Tsukuba, Tsukuba; Japan*
[162] *Department of Physics and Astronomy, Tufts University, Medford MA; United States of America*
[163] *Department of Physics and Astronomy, University of California Irvine, Irvine CA; United States of America*
[164] *University of West Attica, Athens; Greece*
[165] *University of Sharjah, Sharjah; United Arab Emirates*
[166] *Department of Physics and Astronomy, University of Uppsala, Uppsala; Sweden*
[167] *Department of Physics, University of Illinois, Urbana IL; United States of America*
[168] *Instituto de Física Corpuscular (IFIC), Centro Mixto Universidad de Valencia — CSIC, Valencia; Spain*
[169] *Department of Physics, University of British Columbia, Vancouver BC; Canada*
[170] *Department of Physics and Astronomy, University of Victoria, Victoria BC; Canada*
[171] *Fakultät für Physik und Astronomie, Julius-Maximilians-Universität Würzburg, Würzburg; Germany*
[172] *Department of Physics, University of Warwick, Coventry; United Kingdom*
[173] *Waseda University, Tokyo; Japan*
[174] *Department of Particle Physics and Astrophysics, Weizmann Institute of Science, Rehovot; Israel*
[175] *Department of Physics, University of Wisconsin, Madison WI; United States of America*
[176] *Fakultät für Mathematik und Naturwissenschaften, Fachgruppe Physik, Bergische Universität Wuppertal, Wuppertal; Germany*
[177] *Department of Physics, Yale University, New Haven CT; United States of America*
[178] *Yerevan Physics Institute, Yerevan; Armenia*

[a] *Also Affiliated with an institute covered by a cooperation agreement with CERN*
[b] *Also at An-Najah National University, Nablus; Palestine*
[c] *Also at Borough of Manhattan Community College, City University of New York, New York NY; United States of America*
[d] *Also at Center for High Energy Physics, Peking University; China*
[e] *Also at Center for Interdisciplinary Research and Innovation (CIRI-AUTH), Thessaloniki; Greece*
[f] *Also at CERN, Geneva; Switzerland*
[g] *Also at CMD-AC UNEC Research Center, Azerbaijan State University of Economics (UNEC); Azerbaijan*
[h] *Also at Département de Physique Nucléaire et Corpusculaire, Université de Genève, Genève; Switzerland*
[i] *Also at Departament de Fisica de la Universitat Autonoma de Barcelona, Barcelona; Spain*
[j] *Also at Department of Financial and Management Engineering, University of the Aegean, Chios; Greece*
[k] *Also at Department of Physics, California State University, Sacramento; United States of America*
[l] *Also at Department of Physics, King's College London, London; United Kingdom*

JHEP08(2025)034

[m] Also at Department of Physics, Stanford University, Stanford CA; United States of America
[n] Also at Department of Physics, Stellenbosch University; South Africa
[o] Also at Department of Physics, University of Fribourg, Fribourg; Switzerland
[p] Also at Department of Physics, University of Thessaly; Greece
[q] Also at Department of Physics, Westmont College, Santa Barbara; United States of America
[r] Also at Faculty of Physics, Sofia University, 'St. Kliment Ohridski', Sofia; Bulgaria
[s] Also at Hellenic Open University, Patras; Greece
[t] Also at Imam Mohammad Ibn Saud Islamic University; Saudi Arabia
[u] Also at Institucio Catalana de Recerca i Estudis Avancats, ICREA, Barcelona; Spain
[v] Also at Institut für Experimentalphysik, Universität Hamburg, Hamburg; Germany
[w] Also at Institute for Nuclear Research and Nuclear Energy (INRNE) of the Bulgarian Academy of Sciences, Sofia; Bulgaria
[x] Also at Institute of Applied Physics, Mohammed VI Polytechnic University, Ben Guerir; Morocco
[y] Also at Institute of Particle Physics (IPP); Canada
[z] Also at Institute of Physics and Technology, Mongolian Academy of Sciences, Ulaanbaatar; Mongolia
[aa] Also at Institute of Physics, Azerbaijan Academy of Sciences, Baku; Azerbaijan
[ab] Also at Institute of Theoretical Physics, Ilia State University, Tbilisi; Georgia
[ac] Also at National Institute of Physics, University of the Philippines Diliman (Philippines); Philippines
[ad] Also at Technical University of Munich, Munich; Germany
[ae] Also at The Collaborative Innovation Center of Quantum Matter (CICQM), Beijing; China
[af] Also at TRIUMF, Vancouver BC; Canada
[ag] Also at Università di Napoli Parthenope, Napoli; Italy
[ah] Also at University of Colorado Boulder, Department of Physics, Colorado; United States of America
[ai] Also at Washington College, Chestertown, MD; United States of America
[aj] Also at Yeditepe University, Physics Department, Istanbul; Türkiye
[*] Deceased

JHEP08(2025)034